

2022

Gold nanoparticles as probes in epidermal growth factor receptor clustering and second messenger mediated activation

<https://hdl.handle.net/2144/45501>

Downloaded from DSpace Repository, DSpace Institution's institutional repository

BOSTON UNIVERSITY
GRADUATE SCHOOL OF ARTS AND SCIENCES

Dissertation

**GOLD NANOPARTICLES AS PROBES IN EPIDERMAL
GROWTH FACTOR RECEPTOR CLUSTERING AND
SECOND MESSENGER MEDIATED ACTIVATION**

by

SANDY ZHANG

B.S., Binghamton University, 2015

Submitted in partial fulfillment of the
requirements for the degree of
Doctor of Philosophy

2022

© 2022 by
SANDY ZHANG
All rights reserved

Approved by

First Reader

Björn M. Reinhard, PhD
Professor of Chemistry

Second Reader

Lawrence D. Ziegler, PhD
Professor of Chemistry

Acknowledgments

First and foremost, I would like to thank my advisor Björn M. Reinhard for all of his support and guidance over the years. When I was first getting started in graduate school, he would often be in the lab to do experiments with me and was incredibly hands-on. He always encouraged scientific inquiry, which was an inspiration to me during this journey. We've shared many talks about science as well as many laughs during my time at Boston University. It has been such a joy working in Björn's lab and learning from him. His passion for science and dedication to the research endeavors of his students have deeply inspired me.

I would also like to thank my dissertation advisory committee (Professor David Coker, Professor Xi Ling, Professor Lawrence D. Ziegler, and Professor Masha Kamenetska) for helping me navigate graduate school and for their feedback. I would also like to acknowledge the help I received from the facilities and staff at Boston University's Photonics Center and the Chemistry department. Additionally, I want to thank Dr. Todd Blute for all of this help with the flow cytometer, especially when I ran into issues with the instrument. I would also like to thank Dr. Andy Fan for training me and helping me with western blots. Additionally, I would like to thank my lab members who helped me a lot when I first started graduate school, Sarah, Linxi, Ali, and Amin. They were very welcoming and helped train me on different lab techniques and instrumentats. Finishing up my PhD during COVID had its own challenges, but being able to share laughs with my colleagues in the lab (Taejun, Han, Aidan, Leslie, Xingda, and everyone else) made things a lot better and for that I am thankful. I would also like to thank Behnaz and Leslie for being great colleagues as well as being my friends outside of the lab.

I would also like to thank my family and friends for all of their love and support.

My parents have been very supportive throughout this process and always gave me words of encouragement. They also taught me not to be too hard on myself and to take breaks when I needed them. My brother, Jimmy, was always there for me and offered advice for anything I might be going through. I would also like to thank my friends France, ShuMin, and Irene. We may be in different cities and time zones, but they always made time to catch up with me and cheer me on. For that, I will be forever grateful. Lastly, I want to thank my partner Nick for being there for every up and down during the entire PhD. He has been very understanding and always encouraged me to keep going even when it was hard for me. I am extremely grateful for his continued support in all of the moments in my life. We've also had many fun adventures together and with friends in Boston, which made graduate school a very enjoyable time in my life.

GOLD NANOPARTICLES AS PROBES IN EPIDERMAL GROWTH FACTOR RECEPTOR CLUSTERING AND SECOND MESSENGER MEDIATED ACTIVATION

SANDY ZHANG

Boston University, Graduate School of Arts and Sciences, 2022

Major Professor: Björn M. Reinhard, PhD. Professor of Chemistry

ABSTRACT

The epidermal growth factor receptor (EGFR) is a prototypical receptor tyrosine kinase that plays an important role in cell growth, while its dysregulation is associated with a broad range of cancers. Understanding the mechanisms that underlie EGFR activation are crucial for the development of novel therapeutic targets. In this dissertation, the spatial distribution of EGFR and the role of reactive oxygen species (ROS) in modulating EGFR activation are elucidated.

Spatial clustering of EGFR has been indicated to play a regulatory role in signal initiation, and the distribution of receptors on the cell surface may represent a potential biomarker. To realize its potential for diagnostic purposes, high-throughput assays capable of mapping spatial receptor heterogeneity on the length scale of tens of nanometers are needed. To that end, gold (Au) nanoparticle (NP) labels are used as bright optical probes for detecting large-scale EGFR clustering in cancer cells. The clustering spatial maps obtained from hyperspectral plasmon coupling microscopy (PCM) are compared to those obtained through fluorescence direct stochastic optical

reconstruction microscopy (dSTORM). The results revealed that hyperspectral PCM imaging of NP labels identified the same trends in large-scale EGFR clustering as dSTORM, but the NP imaging approach provided the information in a fraction of the time.

Au NPs can also be decorated with ligands through nanoconjugation to probe ligand-receptor interactions. Multivalent ligand presentation on NPs is considered a general approach for controlling and amplifying local EGFR activation in receptor clusters. ROS have been indicated to play a role in the regulation of EGFR activation as a second messenger, but the effect of nanoconjugation (NP-EGF) on EGF-mediated ROS formation and ROS-induced EGFR activation is not well established. Au NPs functionalized with two different EGF ligand densities were used to quantify NP-EGF-induced ROS generation and EGFR phosphorylation in breast cancer cell models. In EGFR overexpressing cell lines, nanoconjugated EGF with higher ligand density achieved a multivalent enhancement of ROS that was EGFR and nicotinamide adenine dinucleotide phosphate oxidase (NOX) dependent. This multivalent enhancement is not exclusively related to avidity but also to a stronger stimulation per NP. Importantly, the increase in EGF-induced ROS formation associated with EGF nanoconjugation resulted in a gain in EGFR phosphorylation, confirming that ROS generation contributes to the multivalent enhancement of EGFR activation in response to NP-EGF.

Contents

1	Introduction	1
1.1	Ligand-Induced Dimerization Model of EGFR	2
1.2	Ligand-Induced Oligomerization and Clustering of EGFR	4
1.3	Ligand-Induced Reactive Oxygen Species Generation	7
1.4	Imaging Methods for Characterizing Receptor Clustering	9
1.4.1	Conventional Optical and Fluorescence Microscopy	10
1.4.2	Superresolution Fluorescence Microscopy	11
1.4.3	Plasmon Coupling Microscopy	14
1.5	Design and Nanoconjugation of Metal Nanoparticles	18
1.6	The Scope and Organization of this Dissertation	21
2	Characterizing Large-Scale Receptor Clustering on the Single Cell Level: A Comparative Plasmon Coupling and Fluorescence Microscopy Study	23
2.1	Superresolution dSTORM Imaging of EGFR Clustering	24
2.2	Hyperspectral Plasmon Coupling Microscopy for Characterizing EGFR Heterogeneity	27
2.3	Optical Analysis of EGFR Heterogeneity through Plasmon Coupling between NP Labels	29
2.4	Wide-Field Ratiometric Analysis of NP Labels for Quantifying Receptor Clustering	32

2.5	Probing Changes in EGFR Clustering Induced by Dissolution of Cortical Actin Network	36
2.6	Throughput Comparison of dSTORM Imaging and Hyperspectral Plasmon Coupling Microscopy for Analysis of Single Cells	38
2.7	Conclusion	39
2.8	Materials and Methods	40
3	Multivalent Ligand-Nanoparticle Conjugates Amplify ROS Second Messenger Generation and Enhance Epidermal Growth Factor Receptor Phosphorylation	46
3.1	NP-EGF design and characterization	47
3.2	EGF-mediated ROS generation is EGFR and NOX dependent	49
3.3	Multivalent Enhancement of EGF-mediated cytoplasmic ROS Generation	53
3.4	NP-EGF-induced ROS generation and EGFR phosphorylation	60
3.5	Conclusion	63
3.6	Materials and Methods	64
4	Future Directions	71
A	Data Organization and Storage	74
	References	76
	Curriculum Vitae	93

List of Tables

2.1	R_{av} (hyperspectral PCM) and Cluster diameter (dSTORM) Values .	35
-----	---	----

List of Figures

1.1	Schematic diagram of EGFR structure.	3
1.2	A model for EGFR oligomerization.	5
1.3	General mechanisms for thiol-based redox modulation of EGFR activation.	8
1.4	Overview of SMLM Imaging Principle.	12
1.5	Jablonski diagram of dSTORM photoswitching.	13
1.6	Universal scaling law for plasmon coupling of 40 nm Au dimers.	16
1.7	Schematic overview of the setup for hyperspectral plasmon coupling microscopy.	17
1.8	The spectral response of NP labels depends on the NP density and receptor clustering on the cell surface.	18
1.9	Design scheme of functionalized Au NPs.	20
2.1	dSTORM imaging of EGFR clustering.	25
2.2	Detection of EGFR spatial heterogeneity using Au NP labels.	28
2.3	Optical analysis of digital color images of NP labels.	29
2.4	Hopkins Statistics for spatial randomness of NP labels (digital color images).	30
2.5	Hopkins Statistics for spatial randomness of NP labels (SEM images).	31
2.6	Schematic overview of hyperspectral PCM imaging approach.	33
2.7	Resonance peak wavelength and ratiometric analysis of NP labels.	34

2.8	Correlation plot of R_{av} (hyperspectral PCM) and average EGFR cluster size (dSTORM)	36
2.9	Hyperspectral PCM and dSTORM analysis of Lat A-treated cells. . .	37
2.10	Comparison of hyperspectral PCM and dSTORM applied for optical mapping of NP labels and fluorescence labeling of EGFR.	39
3.1	Schematic of NP-EGF design.	48
3.2	EGF-mediated ROS generation is EGFR and NOX dependent.	51
3.3	Basal intracellular ROS levels for breast cancer cell models.	52
3.4	Mitochondrial superoxide ROS generation at 1.6 nM EGF.	52
3.5	Cytoplasmic ROS generation of NP-PEG and NP-EGF.	53
3.6	ROS_{max} values for NP-PEG and NP-EGF.	54
3.7	GSH/GSSG ratio for NP-EGF ₈₇	55
3.8	Cell viability (MTT assay) of cells incubated with NP-PEG and NP-EGF.	56
3.9	Source of NP-EGF-mediated ROS generation.	57
3.10	Multivalent enhancement of NP-EGF mediated ROS generation as measured by cellular uptake.	59
3.11	Multivalent enhancement of NP-EGF-mediated EGFR phosphorylation.	61
3.12	NP-EGF-mediated EGFR activation is modulated by cellular ROS levels and NOX activity.	62
4.1	Detection of H ₂ O ₂ gradients using HyPer probe.	72

Acronyms

Ab antibody. 28

AQP aquaporin. 8

Au gold. vi

CCD charge-coupled device. 41

Cys cysteine. 7

DMEM Dulbecco's modified Eagle medium. 40

DMEM/F12 Dulbecco's Modified Eagle Medium/F-12. 64

DPI diphenyleneiodium. 50

DPPC 1,2-dipalmitoyl-sn-glycero-3-phosphocholine. 28

dSTORM direct stochastic optical reconstruction microscopy. vi, vii, 11

EGF epidermal growth factor. 2

EGFR epidermal growth factor receptor. vi

ELISA enzyme-linked immunosorbent assay. 48

F-actin actin filament. 6

FWHM full width at half maximum. 32

GSH glutathione. 55

H₂O₂ hydrogen peroxide. xii, 7, 71–73

Lat A Latrunculin A. 36

LSPR localized surface plasmon resonance. 14

MP-AES microwave plasma atomic emission spectroscopy. 58

MTT 3-(4,5-dimethylthiazol-2-yl)-2,5-diphenylterazolium bromide. 56

NA numerical aperture. 41

NAC N-acetylcysteine. 50

NADPH nicotinamide adenine dinucleotide phosphate. 7

NHS N-hydroxysuccinimidyl. 65

NOX nicotinamide adenine dinucleotide phosphate oxidase. 7

NP nanoparticle. vi

NS not significant. 25, 37

O₂ molecular oxygen. 7

O₂⁻ superoxide. 7, 8

OD optical density. 69

PALM photoactivated localization microscopy. 11

PBS phosphate-buffered saline. 41

PCM plasmon coupling microscopy. vi, 15

PEG polyethylene glycol. 19

pEGFR phosphorylated EGFR. 60

PI(4,5)P2 phosphatidylinositol 4,5-biphosphate. 6

PSF point spread function. 11, 32

PTB phosphotyrosine-binding. 2

PTPs protein tyrosine phosphatases. 7

RTK receptor tyrosine kinase. 1

S₀ ground state. 12, 13

S₁ singlet state. 12, 13

S.E.M standard error of the mean. 34

SD standard deviation. 25, 37

SEM scanning electron microscope. 31, 45

SH2 Src homology. 2

SMLM single-molecule localization microscopy. 11

STORM stochastic optical reconstruction microscopy. 11

T₁ triplet state. 12, 13

TNBC triple negative breast cancer. 24

Y tyrosine. 2

Y1068 tyrosine 1068. 60

Chapter 1

Introduction

The epidermal growth factor receptor (EGFR or HER1/ERbB1) is a cell surface receptor tyrosine kinase (RTK) that plays an essential role in cell growth¹, differentiation², and proliferation¹. EGFR is considered the prototypical RTK since it was the first to be discovered³ and has been studied extensively since its discovery. It is also the first RTK in which ligand mediated oligomerization (EGFR clustering) was observed to be crucial for activation and the first in which a relationship between receptor dysregulation and oncogenesis^{4,5} was determined. EGFR serves as a prognostic biomarker since its overexpression, dysregulation, and mutation is associated with a range of cancers.⁶⁻¹⁰ Cancer therapies that target EGFR^{11,12} are often met with initial outstanding response, however, over time, treatments often lead to acquired drug resistance in patients.¹³ Thus, it becomes imperative to understand the mechanisms the underlie structure-function of EGFR in order to inform the development of next generation anti-EGFR therapeutics. Notably, the molecular mechanisms underlying EGFR cluster formation are not well understood. It has been documented that EGFR forms more clusters that are larger in size on the cell surface of cancer cells compared with normal healthy cells.¹⁴ Moreover, the signaling outcome in receptors clusters is distinct from receptors that are not clustered.¹⁵ The signaling output of EGFR is also modulated by reactive oxygen species (ROS) second messenger molecules. ROS may facilitate redox regulation of EGFR to enhance ligand-dependent or -independent

receptor activation in EGFR clusters.

In this introduction chapter, EGFR activation mechanisms based on the ligand-induced dimerization and oligomerization (EGFR clustering) model will be described. The following section introduces EGF ligand-induced EGFR activation and concomitant ROS generation. Then, fluorescence and NP based imaging techniques for characterizing receptor heterogeneity will be discussed. Lastly, the design of multivalent ligand-NP conjugates is introduced.

1.1 Ligand-Induced Dimerization Model of EGFR

EGFR consists of an N-terminal extracellular ligand binding domain (comprising of four subdomains), a single transmembrane helix, and a cytoplasmic region. The cytoplasmic region contains a tyrosine kinase domain and a C-terminal tail with five tyrosine (Y) phosphorylation sites (Y992, Y1045, Y1068, Y1086, and Y1173). The C-terminal tail serves as a docking site for the recruitment of signaling molecules that contain Src homology (SH2) or phosphotyrosine-binding (PTB) domains, which leads to downstream signaling.¹⁶ EGFR is one of a family of four RTKs in humans, the others being ErbB2/HER2, ErbB3/HER3, and ErbB4/HER4. Receptors in the EGFR family are activated by the epidermal growth factor (EGF) and six other different cognate ligands. After ligand binding, the receptors in the EGFR family can form homo- and heterodimers. The diversity in receptor interactions plays a fundamental role in the receptor distribution as well as the signaling output.

The crystal structure of EGF ligands bound to the extracellular domain of EGFR revealed symmetric and doubly ligated EGFR dimers.¹⁷ Another study demonstrated that detergent-solubilized EGFR exists as cross-linked dimers in the presence of a bound ligand, but in the absence of any ligand, EGFR was mostly in its monomeric form.¹⁸ Based on these early structural^{17,19} and biophysical²⁰ studies, the "ligand-

induced dimerization” model was proposed to explain the ligand-bound structure of EGFR and its activation^{21,22}.

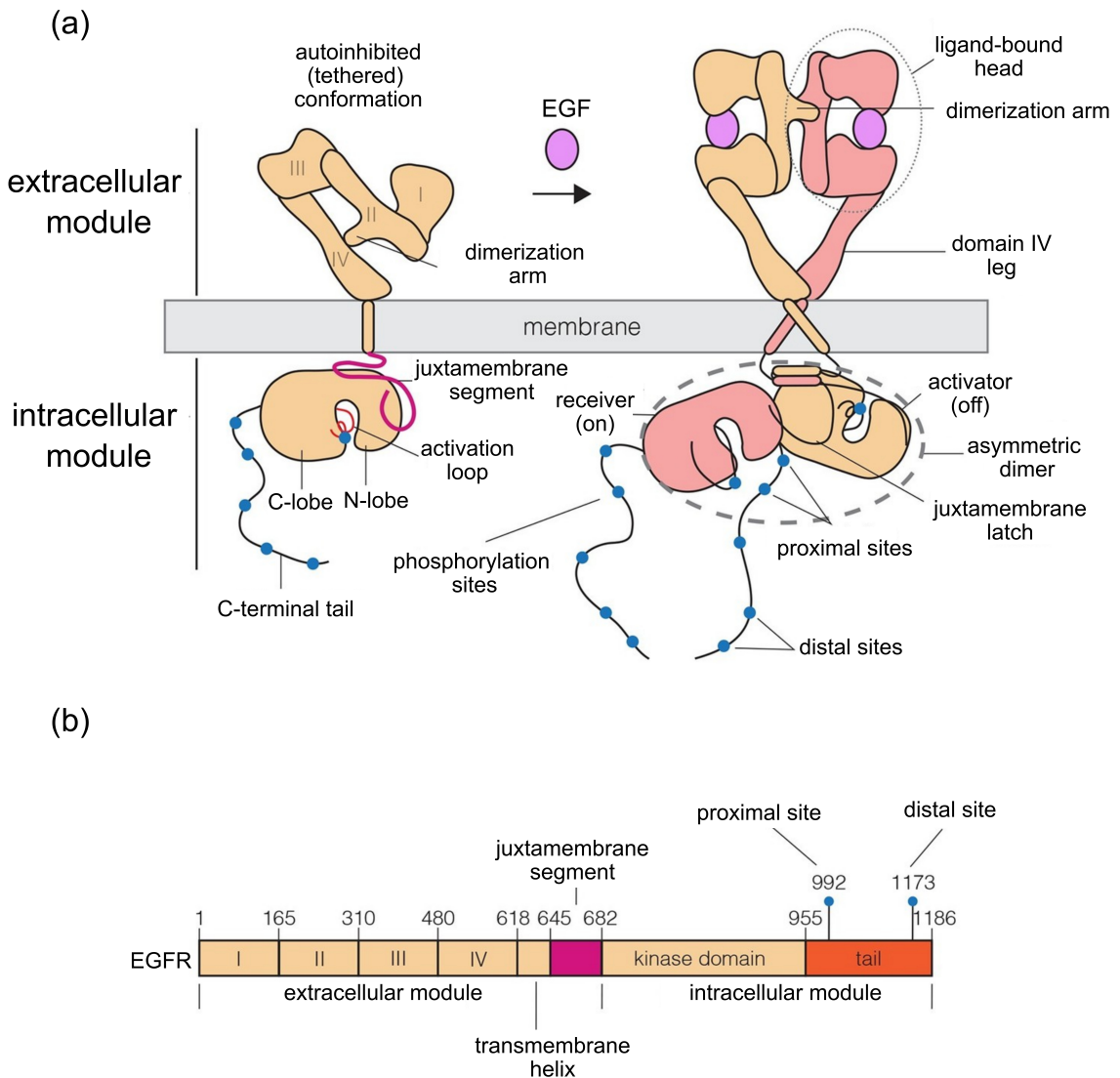


Figure 1.1: Schematic diagram of EGFR structure. (a) The canonical model for the formation of EGFR dimers after EGF ligand binding. (b) Domain boundaries for the extracellular and intracellular module of human EGFR. Adapted with permission from reference²³ under the <https://creativecommons.org/licenses/by/4.0/> for CC BY 4.0 Creative Commons license, © 2016 eLife Sciences Publications Ltd.

In this model, EGFR exists as monomer in its basal (resting) state and ligand binding

to the extracellular domain induces dimerization of the receptor monomer. Ligand binding leads to a rearrangement of the extracellular domain involving a $\sim 130^\circ$ rotation of domains I and II with respect to domains III and IV (Figure 1.1). The receptor monomer goes from a tethered conformation to an extended conformation; the exposed dimerization arm stabilizes the dimer formation. The extracellular domains adopt a ligand bound back-to-back dimer^{17,19} configuration with two EGF ligands bound between domains I and III at the distal sites from the dimer interface. Receptor dimerization also induces allosteric changes in the intracellular kinase domains in which the C-terminal region of the “activator” kinase contacts the N terminal region of the other kinase, termed the “receiver”²⁴ (Figure 1.1). In the asymmetric kinase dimer, interactions between the “activator” and “receiver” kinase are responsible for phosphorylating the C-terminal tail segments and receptor dimerization is a critical component of allosteric activation of EGFR^{19,24}.

1.2 Ligand-Induced Oligomerization and Clustering of EGFR

Although research into EGFR activation has long focused on dimerization-dependent activation²⁵, an increasing number of studies^{26–32} have since demonstrated the importance of ligand-induced higher-order EGFR oligomerization (assemblies larger than dimers) or EGFR clustering in signal regulation^{33–39}. Seminal studies revealed that formation of ligand-induced receptor oligomers^{21,40} or the EGFR dimer-tetramer transition⁴¹ are essential for signaling. Additionally, ligand-induced receptor oligomerization is dependent on receptor tyrosine phosphorylation²⁸ and mutations that prevent oligomerization reduced auto-phosphorylation of EGFR²³. It has also been proposed that oligomerization organizes kinase-active dimers in ways that are optimal for trans-auto phosphorylation between neighboring dimers.^{15,23} In this model, the intracellular kinase domains are sandwiched by other kinase domains which function as “activa-

tors” and “receivers” simultaneously (Figure 1.2). The formation of EGFR oligomers increases the number of effective docking sites for downstream adaptor proteins. Thus, EGFR oligomerization potentiates phosphorylation and readily enables signal propagation in the presence of stimulus. Ligand-induced oligomerization is one mechanism that can promote lateral propagation of EGFR activation across the plasma membrane, especially in cells that overexpress EGFR.⁴² Although ligand-induced dimerization is essential for EGFR activation, oligomerization or receptor clustering is likely to play a pivotal role in ensuring efficient access of adapter molecules to the activated kinases.

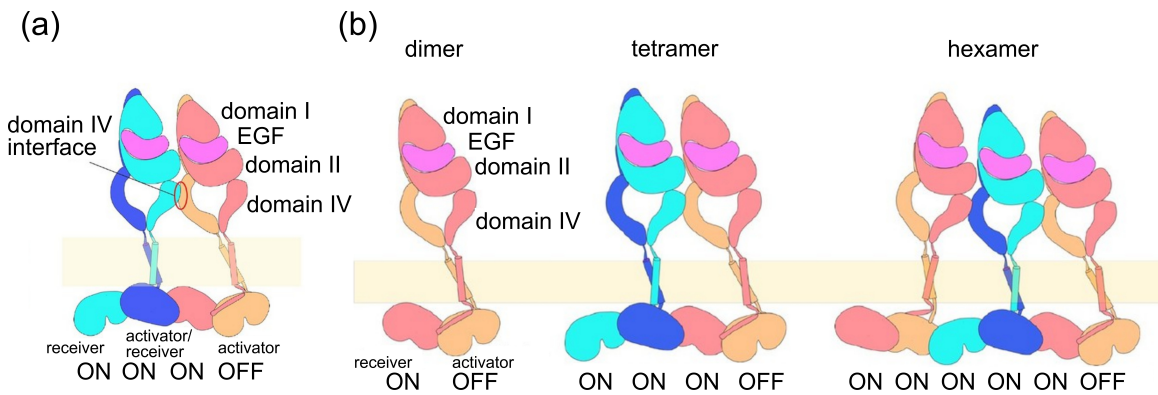


Figure 1.2: A model for EGFR oligomerization. (a) A schematic representation of an EGFR tetramer. (b) Proposed model of higher-order oligomer formation. The kinase domains can function as “activators” and “receivers” simultaneously. Adapted with permission from reference²³ under the <https://creativecommons.org/licenses/by/4.0/> for CC BY 4.0 Creative Commons license, © 2016 eLife Sciences Publications Ltd.

Intriguingly, even in the absence of ligand stimulation, EGFR clusters could be pre-formed^{43–45} on the cell surface and is dependent on both the receptor surface densities and the cell type. Reports indicate that the typical size of EGFR clusters are on the length scale of tens to hundreds of nanometers^{33,46–48}. The membrane composition⁴⁹ as well as protein-protein interactions in the vicinity of EGFR clusters can influence cluster size as well as receptor distribution. EGFR clusters may distribute into dif-

ferent nanoscale domains on the membrane, which can dynamically sequester EGFR and regulate signaling.

The spatial distribution of EGFR is sensitive to its surrounding lipid environment⁵⁰⁻⁵² and the cytoskeletal actin network^{46,50,53}. The actin filament (F-actin) network regulates cellular processes such as cell motility and has been shown to affect the diffusivity of EGFR clusters⁵⁴. Colocalization of EGFR with F-actin stabilizes EGFR signaling complexes in a manner dependent on the synthesis of the anionic phospholipid, phosphatidylinositol 4,5-bisphosphate (PI(4,5)P2), a major regulator of the actin cytoskeleton.⁵³ Additionally, PI(4,5)P2 also interacts with the polybasic juxtamembrane region of EGFR and its depletion results in a decrease in EGFR clustering on the membrane.⁴⁸ Membrane cholesterol also plays an important role in the clustering of ligand-bound EGFR⁵¹ and enhancing EGFR signaling^{49,55}.

On the cell surface, nanoscale domains with varying numbers of receptors can coexist. Ligand-induced EGFR clustering is a common phenomenon in cells expressing these receptors at both physiological and oncogenic expression levels.^{45,47,56,57} Receptor clustering can modulate the signaling output and the correlation between activation with clustering state is essential. Since EGFR is an important cancer biomarker, targeting receptor clusters can represent an attractive therapeutic target for preventing abnormal EGFR activation at an early stage in the signaling process. However, the underlying mechanisms of EGFR clustering are not fully understood. In order to further probe the biological role of spatial receptor heterogeneity and to utilize it as a diagnostic cancer biomarker, it is crucial that methods are available to detect, characterize, and quantify receptor clustering, ideally on the single cell level with high throughput. Imaging methods commonly used to characterize EGFR spatial heterogeneity will be described in more detail in Chapter 1.4.

1.3 Ligand-Induced Reactive Oxygen Species Generation

In the previous sections, ligand-induced EGFR activation through dimerization and oligomerization mechanisms are described. Interestingly, EGFR activation can also be induced by hydrogen peroxide (H_2O_2).⁵⁸ A pioneering study by Gamou and Shimizu⁵⁸ revealed that EGFR may be regulated by oxidants through a unique non-canonical mechanism. Since then, a number of studies demonstrated that ligand-mediated activation of EGFR also leads to the localized production of reactive oxygen species (ROS)^{59–63} through nicotinamide adenine dinucleotide phosphate (NADPH) oxidase (NOX)^{64,65} (Figure 1.3). Although high concentrations of ROS are often associated with cellular oxidative stress and cancer^{66–69}, ROS formed as a result of ligand-receptor interactions can function as physiological second messengers that regulate cell signaling processes^{69–75}. Plasma membrane associated NOX reduce molecular oxygen (O_2) using cytosolic NADPH to generate superoxide (O_2^-), which is then spontaneously or enzymatically dismutated to H_2O_2 . Importantly, NOX-derived H_2O_2 regulates EGFR signaling by oxidizing the active site cysteine (Cys) residue in the intracellular kinase domain of EGFR (Cys 797) to enhance kinase activity (Figure 1.3c).^{65,76} At the same time, H_2O_2 -mediated oxidation of the active site Cys in protein tyrosine phosphatases (PTPs), in particular PTP1B, results in inactivation (Figure 1.3d).^{60,62,77} Since PTPs dephosphorylate activated EGFR, H_2O_2 -mediated inactivation of PTPs prolongs EGFR phosphorylation.^{60,77,78} The inhibition of EGFR dephosphorylation by H_2O_2 is important as activation of EGFR by EGF ligand binding may not be sufficient to increase the steady state level of RTK phosphorylation in cells.^{58,78,79}

The spatial colocalization of NOX and redox-sensitive enzymes⁸⁰, such as RTKs and PTPs, at the plasma membrane⁶⁹ is a critical determinant for the cell physiological effect of the second messenger. EGFR shows a heterogeneous spatial distribution in

the plasma membrane and is known to be enriched in membrane regions with lateral dimensions of tens to hundreds of nanometers^{23,33,46,48,52,81}.

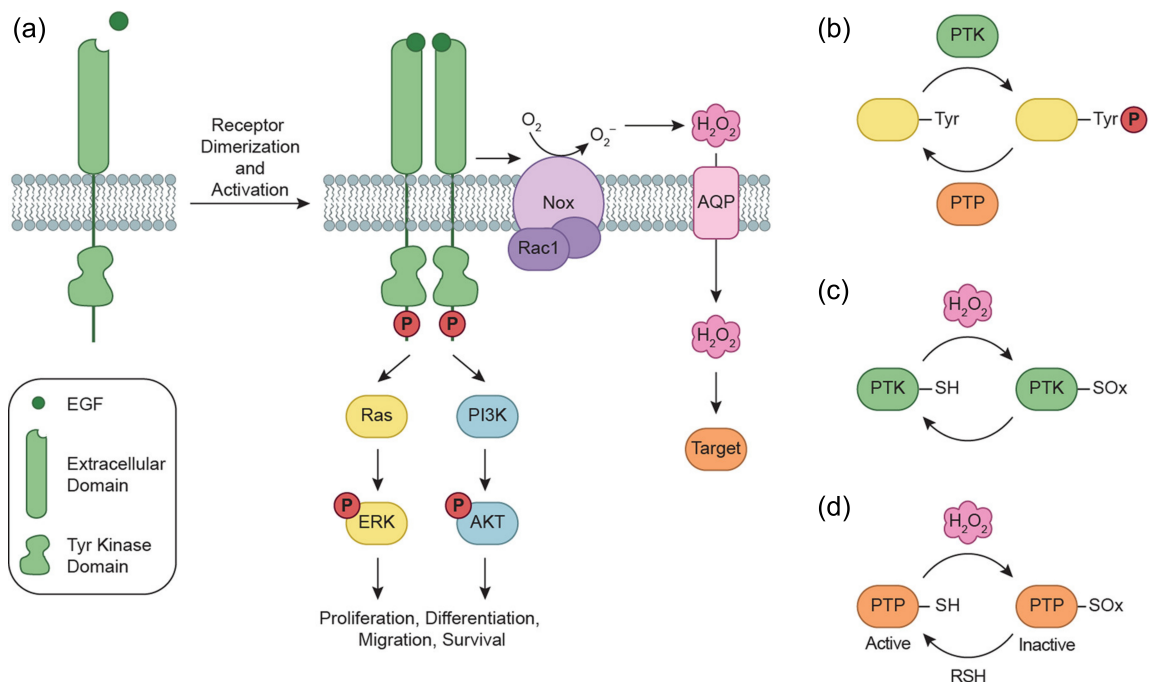


Figure 1.3: General mechanisms for thiol-based redox modulation of EGFR activation. (a) EGF ligand binding to EGFR induces EGFR dimerization, followed by autophosphorylation of Tyr residues in the intracellular kinase domain which triggers the onset of downstream signaling cascades. This also induces NOX activation and the local production of H₂O₂ through spontaneous dismutation of O₂⁻. H₂O₂ can diffuse into the cytosol through specific aquaporin (AQP) channels. H₂O₂ second messenger can then react with redox sensitive targets. (b) Model for redox-dependent signal activation. PTKs catalyze the transfer of γ -phosphoryl groups from ATP to tyrosine hydroxyls of proteins, whereas PTPs remove phosphate groups from phosphorylated tyrosine residues. (c) Cysteine residues in protein kinases can either be reduced or oxidized. Depending on the redox target, this can either have an activating or inactivating effect. (d) Oxidation of the active site Cys residue in PTPs inactivates PTPs. This reaction is reversible in the presence of RSH. SOx in (c) and (d) represents the oxidized form of cysteine. Adapted with permission from reference⁸², © 2012 American Chemical Society.

H₂O₂ has a lifetime of ≈ 1 ms and diffusion length of ≈ 1 μ m within cells.^{74,83} Once released after an initial EGF binding, H₂O₂ second messenger may facilitate redox

regulation of near-by RTKs and PTPs to enhance ligand-dependent or -independent receptor activation in the EGFR cluster of its origin or in neighboring clusters. These regulation mechanisms have potential ramifications for EGFR transactivation and amplification of global EGFR phosphorylation.^{28,32,41,43,84}

Reynolds et al. found for 0.8 micron diameter beads functionalized with different EGF ligand densities that EGF-induced ROS formation plays a role in the lateral activation propagation of EGFR.⁸⁵ Although it is established that multivalent presentation of EGF on smaller NPs can enhance EGFR activation and signaling,^{84,86,87} it remains untested whether multivalent EGF presentation on NPs also affects the intracellular EGFR-mediated ROS generation and how potential changes in the concentration of this second messenger acts back on EGFR activation in response to nanoconjugated EGF. Chapter 3 will discuss in more details how EGF nanoconjugation and multivalent EGF ligand presentation on NPs can be used as a tool to control and amplify ROS and also its effect on EGFR phosphorylation.

1.4 Imaging Methods for Characterizing Receptor Clustering

A long-standing challenge of obtaining quantitative information about the non-uniform receptor distribution on the cell surface is due to the the lack of tools available to address this question on relevant length scales (tens of nanometers). Receptor clusters in discrete regions on the cell surface are difficult to spatially resolve with most conventional imaging modalities. However, in the past decade, emerging imaging technologies are able to address questions about protein behavior on a spatial and temporal scale that cannot be achieved by traditional biochemical assays. Chapter 1.4.1 - 1.4.3 will discuss some of the imaging approaches commonly used to characterize receptor clustering.

1.4.1 Conventional Optical and Fluorescence Microscopy

Conventional optical and fluorescence microscopy techniques are diffraction limited. The diffraction limit, d , is given by the equation:

$$d = \frac{0.61\lambda}{NA} \quad (1.1)$$

where λ is the wavelength of light and NA is the numerical aperture of the objective. The diffraction limit in traditional optical and fluorescence microscopy is between 200–300 nm⁸⁸, which is not sufficient to spatially resolve structural details and molecular interactions below this length scale. The resolution can be improved by using a shorter wavelength of light or a higher NA objective. However, there is a limitation in the wavelength of light that can be used as well as maximal NA for the objective.

EGFR clustering occurs on the length scale of tens of nanometers⁸⁹, a distance too small to be resolved by conventional diffraction-limited optical microscopy techniques^{49,89}. Even for cell lines with physiological EGFR expression levels (40,000–100,000 EGFR/cell)⁹⁰, the local EGFR concentrations on the plasma membrane can be high enough that there is more than one receptor in any given diffraction-limited region of the conventional microscope.⁹¹ Thus, optical techniques that can circumvent the diffraction limit are critical for imaging receptor clusters on relevant length scales. To obtain nanoscale information about the spatial distribution of plasma membrane EGFR, optical methods such as number and brightness analysis^{44,49}, near-field microscopy³³, multi-color optical tracking^{92–94}, and far-field superresolution fluorescence microscopy^{46,48,52,95} have been used. Diffraction limited approaches, such as number and brightness analysis measures the concentration and stoichiometry of complexes. However, number and brightness analysis can only provide information about the number of receptors in a diffraction-limited spot with no direct information about the

spatial clustering of the receptors on shorter length scales. In contrast, fluorescence superresolution microscopy techniques which utilize single-molecule photoswitching of fluorophores, can map the receptor distribution below the diffraction limit as described in Chapter [1.4.2](#).

1.4.2 Superresolution Fluorescence Microscopy

Superresolution fluorescence microscopy techniques can overcome the diffraction barrier of light and allow for imaging cellular and subcellular biological structures. In particular, single-molecule localization microscopy (SMLM) methods have been gaining popularity because these modalities can achieve resolution on the order of ~ 20 -50 nm or better. SMLM techniques typically employ conventional wide-field excitation and achieve superresolution by localizing individual fluorescent molecules. Localization of individual molecules can be achieved with high precision if the point spread function (PSF) of individual emitters do not overlap. SMLM based imaging methods include photoactivated localization microscopy (PALM)^{96,97}, stochastic optical reconstruction microscopy (STORM)⁹⁸, and direct stochastic optical reconstruction microscopy (dSTORM)⁹⁹.

All SMLM techniques depend on the temporal separation of emissions from excited fluorophores¹⁰⁰. Fluorophores are sparsely activated and reversibly switch between an on “bright” state and an off “dark” state. The stochastic “blinking” of non-overlapping PSFs is recorded over time and the position of individual fluorophores is approximated to be at the center of a Gaussian fitting of the PSF. The raw data typically consists of thousands of imaging frames, where each frame contains a sparse subset of fluorescing molecules to allow for localization of individual emitters. Figure [1.4](#) contains an overview for the general principle of SMLM imaging.

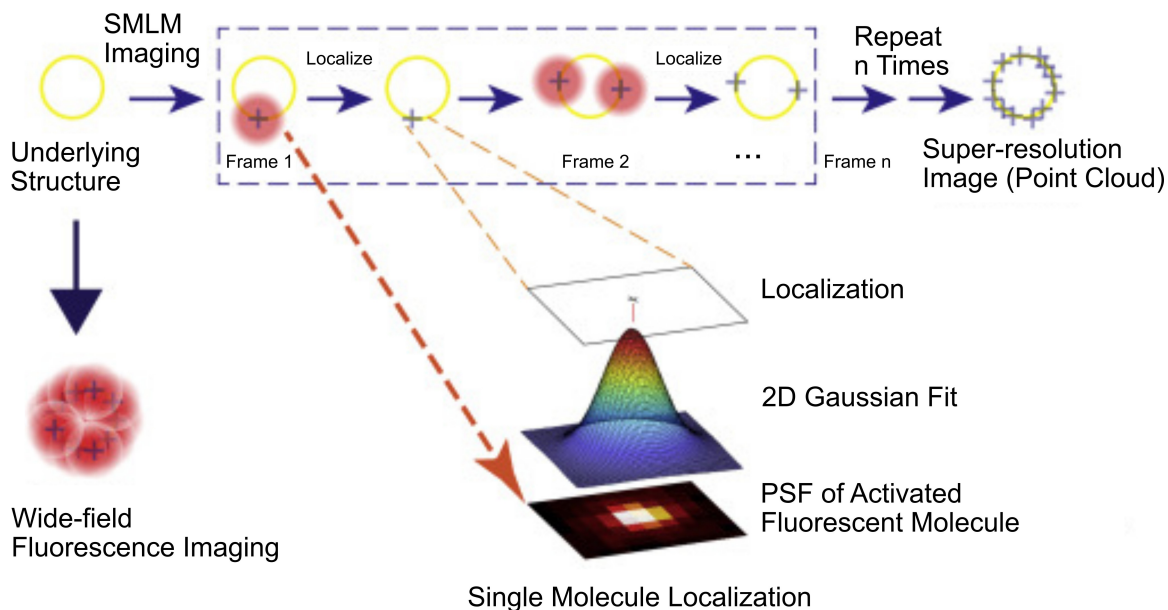


Figure 1.4: Overview of SMLM Imaging Principle. The yellow circle represents the underlying biological structure below the diffraction limit that cannot be spatially resolved using conventional wide-field fluorescence imaging. SMLM imaging produces a superresolution image that is constructed from thousands of imaging frames. The fluorophores are localized using a Gaussian PSF to form the final reconstructed superresolution image. Adapted with permission from reference¹⁰¹, © 2020 Cell Press.

With the emergence of superresolution imaging techniques, EGFR clustering has been investigated on the nanoscale using the SMLM method dSTORM^{48,52,102,103}. Figure 1.5 shows a diagram for the general mechanisms of dSTORM photoswitching. Fluorophores are excited from the ground state (S_0) to the excited singlet state (S_1) from which it can relax back to S_0 while emitting photons (on “bright” state). From S_1 , fluorophores can enter the triplet state (T_1) by applying high-powered laser illumination and can stochastically return back to S_0 .¹⁰⁴ In dSTORM, fluorophores with a low duty cycle are used to label the target of interest. Fluorescent dyes with low duty cycle are in the off “dark” state longer than they are in the on “bright” state, which enable individual emitters to be spatially resolved. To ensure that the fluorophores are in the “dark” state for a sufficient time, they can enter a long-lived dark

state from T_1 through redox reactions in the imaging buffer cocktail which contains thiol reducing agents and oxygen scavengers. This long-lived dark state can last up to many seconds and fluorophores can go back to the ground state through inverse redox reactions. This “blinking” process or switching between on “bright” and off “dark” states is sequentially repeated many times until most of the fluorophores have been localized or until photobleaching occurs.

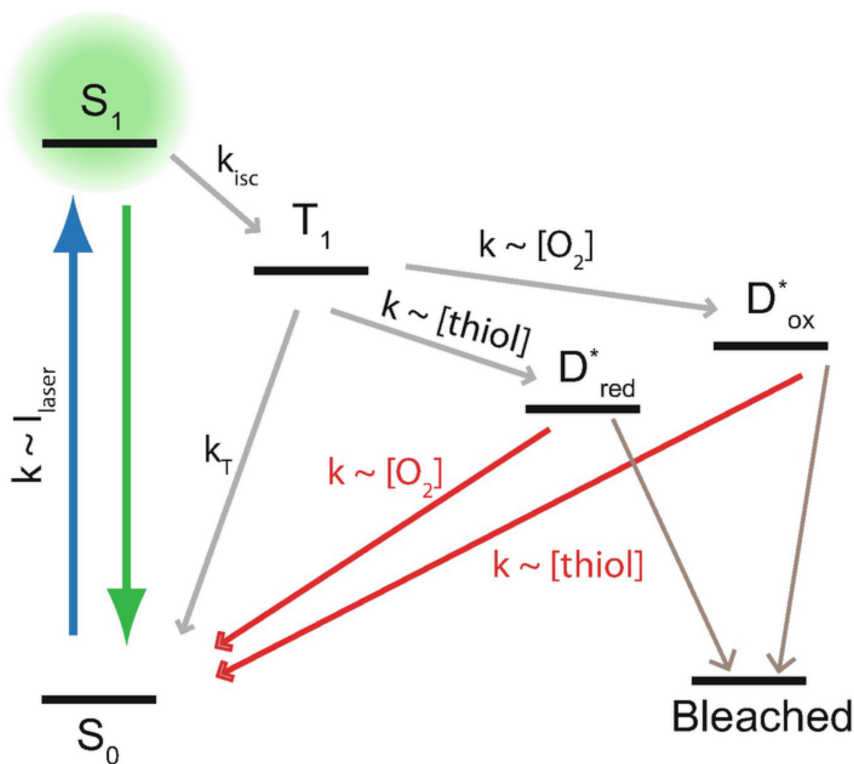


Figure 1.5: Jablonski diagram of dSTORM photoswitching. Fluorescence is only observed when the fluorescent molecule goes between ground state S_0 and singlet excited state S_1 . From S_1 , fluorescent molecules can undergo intersystem crossing to a triplet state T_1 . A long-lived dark state (shown in red) is created by photoreduction of the excited T_1 . From the dark state, fluorophores can return back to S_0 spontaneously or through inverse redox reactions. The presence of oxygen and primary thiols affect the rates at which the transitions occur. Reprinted with permission from reference¹⁰⁵, © 2018 Springer Nature Switzerland AG.

SMLM techniques such as dSTORM typically require acquisition of thousands of

image frames¹⁰⁶⁻¹⁰⁹ to reconstruct a superresolution image, which limits experimental throughput¹⁰⁶ and makes a statistical analysis of receptor clustering in a heterogeneous cell ensemble challenging. Moreover, fluorescence-based approaches in general are subject to restrictions regarding the brightness and photostability of organic dyes. These fundamental limitations have spurred interest in alternative, non-fluorescence based optical approaches for detecting large-scale receptor clustering on the cell surface based on the distance-dependent plasmon coupling between metal NP labels^{84,110-112,112-114} which will be described in the following section (Chapter 1.4.3).

1.4.3 Plasmon Coupling Microscopy

Noble metal NPs such as gold (Au) have superb optical, photophysical and material properties which are exploited in a diverse range of applications.¹¹⁵⁻¹¹⁸ Metal NPs possess unique properties due to the well-known localized surface plasmon resonance (LSPR), which refers to the collective oscillations of electrons on the metallic NPs excited by the incident photons at the resonant frequency¹¹⁹. In contrast to conventional dyes used in fluorescence microscopy, the LSPR of metal NPs increases the light absorption and scattering of metal NPs by orders of magnitude higher.¹²⁰ Additionally, metal NPs have large optical cross-sections and do not blink or bleach compared with organic dyes. Furthermore, Au NPs can be synthesized with excellent size control and there are a variety of bioconjugation strategies available to introduce different targeting moieties on to the NP. The versatility of metal NPs make them a promising candidate for biological applications.

The electromagnetic interactions between individual metal NPs give rise to additional functionalities. When two spherical metal NPs are in close proximity (separations less than one NP diameter), this near-field coupling interaction is detected as a red-shift

in the scattering spectra of the NPs.^{121,122} The strength of plasmon coupling between two metal NPs falls as a function of the interparticle gap scaled by the NP size and follows an exponential decay that is universally independent of NP size, shape, metal type, or the dielectric constant of the surrounding medium.¹²³ For a dimer of metal NPs, the relationship between the fractional shift of the peak position and interparticle separation, s , follows a universal scaling law^{124,125}:

$$\frac{\Delta\lambda}{\lambda_0} \approx Ae^{(-\frac{s/D}{B})} \quad (1.2)$$

where $\Delta\lambda$ is the shift relative to the resonance wavelength, λ_0 , of an individual spherical NP with diameter, D . The coefficients, A and B , are related to the size, shape, and composition of the NP dimers. For a dimer of 40 nm spherical Au NPs, the universal scaling law was experimentally determined as shown in Figure 1.6.¹²⁵ A strong E-field enhancement is also observed as the interparticle separation decreases.

The distance-dependence of plasmon coupling has been utilized in a number of applications, including plasmon coupling microscopy (PCM) with metal NP labels targeted to cell surface receptors^{46,111,113,126}. Plasmon coupling between metal NP labels can be detected in the far-field through elastic or inelastic scattering spectroscopy. The latter utilizes an increase in the Raman signal intensity of dyes bound to the NP when they form electromagnetic hot spots,^{127–129} while the former detects shifts of the plasmon resonance^{111,130–132}. Although PCM is subject to standard diffraction-limited resolution of an optical microscope, subdiffraction limit information can be obtained by acquiring spatial maps of distance-dependent plasmon coupling of metal NP labels using hyperspectral PCM as shown in Figure 1.7.

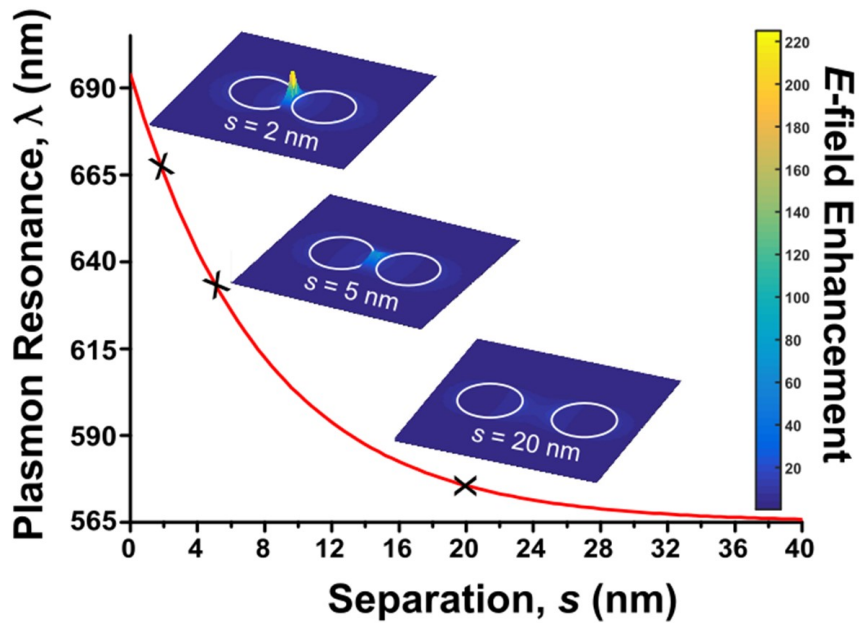


Figure 1.6: Universal scaling law for plasmon coupling of 40 nm Au dimers. Insets show near-field maps for of NP dimers with $s/D = 0.05, 0.125,$ and 0.5 ($s = 2, 5,$ and 20 nm for 40 nm NPs). A strong E-field enhancement is observed as the interparticle separation, s , decreases. Reprinted with permission from reference ¹²⁵, © 2017 World Scientific Publishing Co Pte Ltd.

The schematic overview in Figure 1.7 demonstrates hyperspectral PCM imaging of Au NPs between 540 and 650 nm. The wavelength of light used for excitation can be tuned by incorporating a tunable liquid crystal filter. In a typical setup, the entire field of view of a darkfield microscope is illuminated at a specific wavelength and a monochromatic image is recorded for each chosen wavelength. After correcting the individual monochromatic images by subtracting the intensity profile of the excitation source, the images can be combined into a hyperspectral composite image. In this composite image, each pixel contains information about the relative intensities on the different wavelength channels. ¹¹³

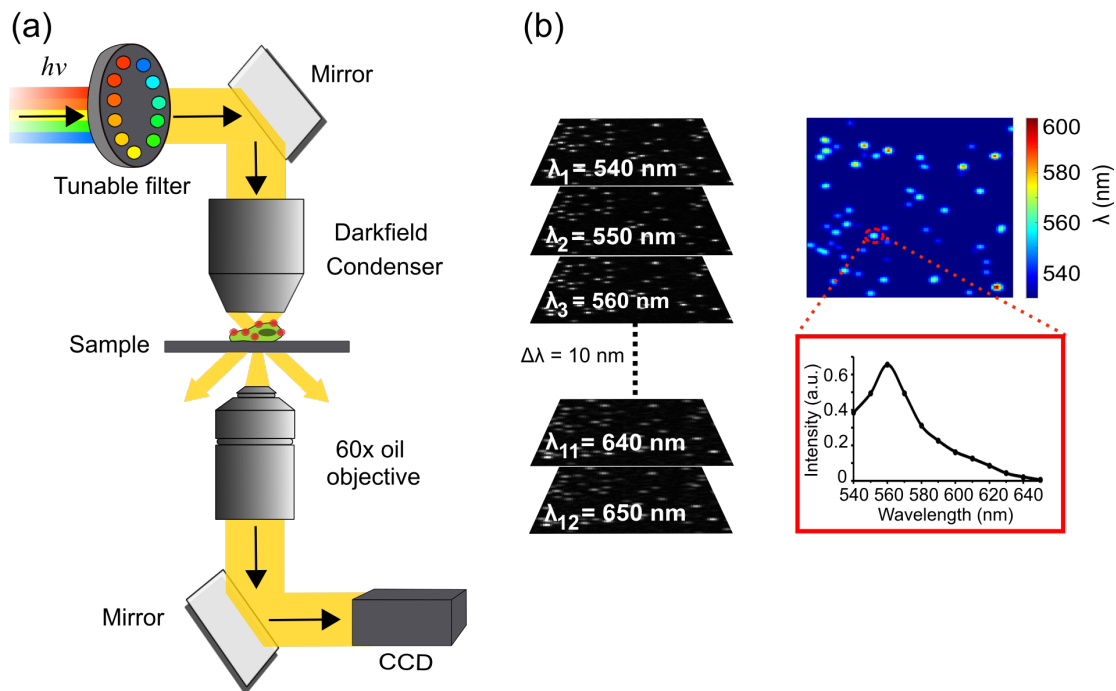


Figure 1.7: Schematic overview of the setup for hyperspectral plasmon coupling microscopy. Acquisition of a monochromatic image from $\lambda = 540\text{-}650$ nm, every 10 nm, to generate a hyperspectral composite image. Each pixel in the composite image provides complete spectral information of the NP labels Reprinted with permission from reference⁴⁶, © 2019 American Chemical Society

PCM can be augmented by ratiometric imaging at predefined wavelengths. Since images of the same field of view can be obtained at specific wavelengths, ratiometric imaging can be utilized to detect NP association levels. For a given frame n , the intensity ratio $R(n)$ can be calculated (Eq. 1.3). The spectral information in R allows for a ratiometric detection of NP labels targeted to cell surface receptors (Figure 1.8).^{46,111} For ratiometric analysis, if the wavelength channels are chosen such that $\lambda_2 > \lambda_1$, the formation of strongly coupled NP labels results in an increase in R . The ratio R of the NPs' intensities on the two wavelength channels can provide

quantitative information about receptor clustering.

$$R(n) = \frac{I_{\lambda_2}(n)}{I_{\lambda_1}(n)} \quad (1.3)$$

Since subdiffraction limit information can be obtained through hyperspectral PCM on the length scale of tens to hundreds of nanometers, this technique is suitable for characterizing large-scale EGFR heterogeneity on the cell surface. The binding of metal NP labels targeted to EGFR allows for spatial EGFR mapping of receptor clusters on the cell surface through monitoring the resonance peak shifts.

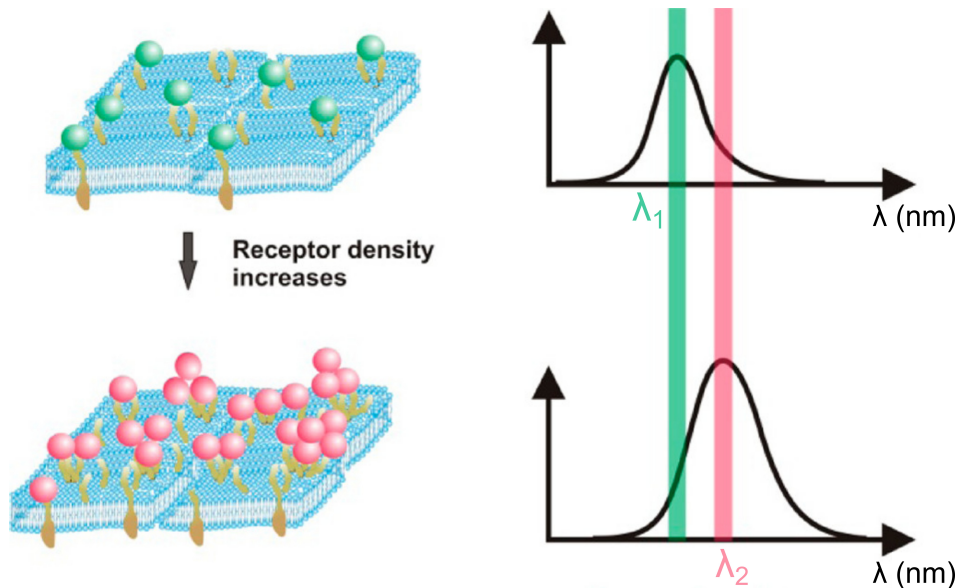


Figure 1.8: The spectral response of NP labels targeted to cell surface receptors depends on the density of NP labels and the receptor clustering on the cell surface. As the average interparticle separation between the NPs decrease, the plasmon resonance red-shifts. Adapted with permission from reference¹³³, © 2012 American Chemical Society.

1.5 Design and Nanoconjugation of Metal Nanoparticles

Au NPs are considered to be relatively non-toxic, however, there are a number of *in vitro* studies that demonstrated Au NP-related cytotoxicity.^{134,135} Modification of

the surface chemistry on the NP through surface coating strategies is one way to increase the overall biocompatibility of NPs and NP stability in aqueous solutions. To achieve this, Au NPs can be coated with various polymers, surfactants, proteins, as well as lipids. Given the high degree of design flexibility for functionalized Au NPs, these nanomaterials can be applied to numerous biological applications. The design and nanoconjugation of metal NPs implemented for the work presented in this dissertation are discussed below.

A scheme for EGFR-targeting Au NP labels used for the studies presented in Chapter 2 is shown in Figure 1.9a. Lipids are biocompatible and a natural component of cell membranes, which makes lipid coating a great candidate for NP surface coating. To generate lipid-coated Au NP labels, lipids are integrated via their hydrophobic tail into an octadecanethiol monolayer assembled around a Au NP core. A biotinylated lipid is incorporated in the lipid coating to allow for biotin-avidin binding to biotinylated EGFR on the cell surface.

Another strategy for targeting cell surface EGFR is through EGF nanoconjugation (NP-EGF). For the work presented in Chapter 3, citrate-stabilized Au NPs are grafted with two different thiol polyethylene glycol (PEG) molecules. PEGylation is a common coating strategy that can increase biocompatibility and shield the NP surface from aggregation.¹³⁶ A scheme for the NP-EGF design is shown in Figure 1.9b. The azide-containing PEG is used to tether alkyne-functionalized EGF to the Au NPs through Cu(I) catalyzed click reaction. The shorter carboxy PEG is used to stabilize the NPs and to increase the accessibility of the azido group on the NP surface. In addition to allowing for specific targeting to EGFR, multivalent ligand presentation through EGF nanoconjugation has been shown to influence EGF-EGFR mediated processes.^{84,86,87} In general, the design of multivalent ligand-decorated NPs enables NP attachment to a specific target through numerous binding interactions, which im-

proves targeting efficiency compared to monovalent NPs or free ligand.¹³⁷ Moreover, signal activation^{42,84,85,138} can also be tuned and amplified through multivalent ligand presentation on NPs by increasing binding avidity^{139–141} as well as influencing ligand-receptor interactions^{142–148}. In the case of NP-EGF, multiple ligand-receptor contacts within the footprint of the NP can generate a strong local receptor activation that results in signal propagation across the cell membrane.⁴² Thus, EGF-functionalized NPs can act as quantifiable units of EGFR activation to probe the effect of multivalency on EGF-dependent processes, which will be described in more detail in Chapter 3.

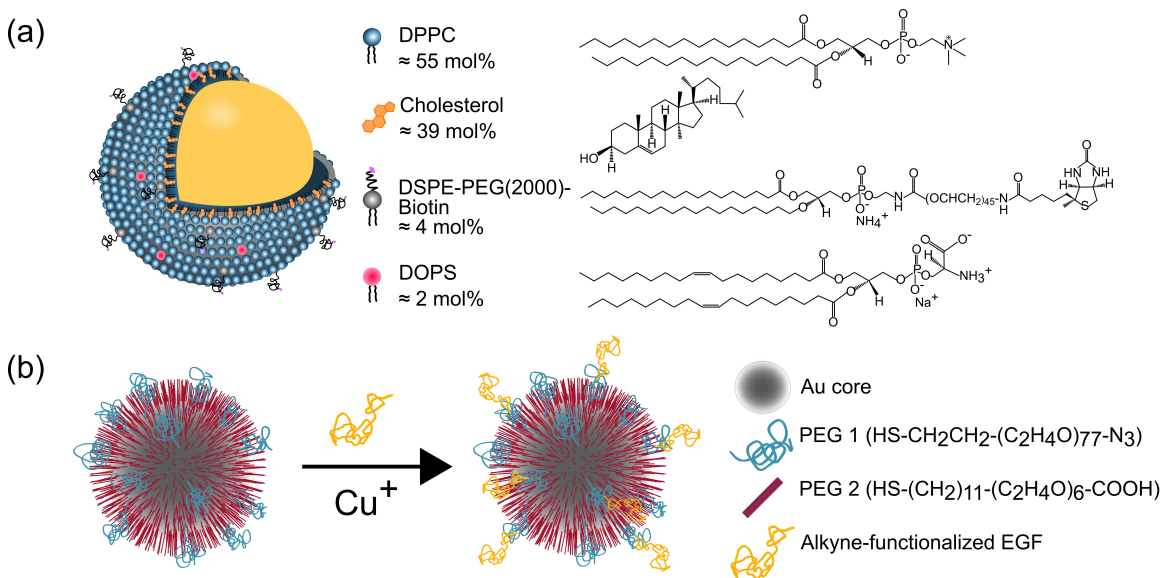


Figure 1.9: Design scheme of functionalized Au NPs. (a) Lipid-coated Au NPs composed of a lipid layer anchored to the Au NP core through 1-octadecanethiol. (b) Schematic of NP-EGF design. 81 ± 1 nm spherical Au NPs are functionalized with PEG 1 (HS-CH₂CH₂-(C₂H₄O)₇₇-N₃) and PEG 2 (HS-(CH₂)₁₁-(C₂H₄O)₆-COOH) in a nominal ratio of 10:1. Alkyne-functionalized EGF was tethered to azido group of PEG 1 through Cu(I) catalyzed 1,3-dipolar cycloaddition reaction.

1.6 The Scope and Organization of this Dissertation

The work described in this dissertation focuses on biological applications of functionalized Au NP probes. Plasmonic Au NPs possess unique optical properties and are used as a bioimaging probe to characterize spatial heterogeneity of EGFR on cancer cells. Additionally, multivalent ligand presentation on Au NPs allows them to be an excellent tool in investigating the role of multivalency in EGF-EGFR dependent processes.

Chapter 2 focuses on the characterization of large-scale EGFR clustering on the length scale of tens to hundreds of nanometers. Superresolution dSTORM imaging of fluorescently labeled EGFR and hyperspectral PCM using Au NP labels targeted to EGFR are both used to characterize EGFR spatial heterogeneity. Subsequently, both imaging methods are applied to test the role of the cortical actin network in patterning large-scale EGFR clustering. The quantitative information obtained from hyperspectral PCM imaging are compared to that of superresolution dSTORM imaging of EGFR clustering. A comparison of the experimental throughput of both imaging methods is emphasized.

In Chapter 3, the role of nanoconjugated EGF on EGF-mediated ROS formation and ROS-induced EGFR activation in breast cancer cell models are discussed. First, the design and characterization of nanoconjugated EGF are introduced. The source of EGF-mediated and NP-EGF-mediated ROS generation are also determined. Multivalent enhancement of NP-EGF mediated cytoplasmic ROS and EGFR phosphorylation are also examined. The future directions of the studies discussed herein are detailed in Chapter 4.

This dissertation includes material from one publication by the author. Chapter 2 includes material from reference⁴⁶, © 2019 American Chemical Society. Chapter 3 is

based on unpublished work that is under review for publication. Material from both papers are included in the introductory chapter of this dissertation.

Chapter 2

Characterizing Large-Scale Receptor Clustering on the Single Cell Level: A Comparative Plasmon Coupling and Fluorescence Microscopy Study

Spatial clustering of cell membrane receptors such as EGFR play a regulatory role in signal initiation as described in Chapter 1. The distribution of receptors on the cell surface may represent a potential biomarker and to realize its potential for diagnostic purposes, scalable assays capable of mapping spatial receptor heterogeneity with high throughput are needed. Given the cell-to-cell variability of cancer cells, a technique that allows analysis at the single cell level is critical. In this chapter, Au NP labels with an average diameter of 72.17 ± 2.16 nm are used for mapping large-scale EGFR clustering (tens to hundreds of nanometers) in hyperspectral PCM and compared to the cluster maps obtained through fluorescence superresolution dSTORM imaging. Though diffraction limited, hyperspectral imaging of NP labels can differentiate differences in EGFR cluster sizes based on differences in the average separations between electromagnetically coupled metal NPs. Due to the distance dependence of plasmon coupling, changes in the average interparticle separation results in significant spectral shifts. In this chapter, both imaging techniques are used to compare trends of large-scale EGFR clustering in the absence of EGF ligand stimulation (basal), EGF

ligand stimulation, and perturbation of the cortical actin network.

2.1 Superresolution dSTORM Imaging of EGFR Clustering

To investigate the spatial heterogeneity of EGFR “clusters”, where a cluster is defined as a membrane region enriched in EGFR, we used dSTORM imaging. All experiments in the work described in this chapter were performed with two different cell lines: the human cervical cancer cell line HeLa with a physiological EGFR expression level (5×10^4 receptors/cell)¹⁴⁹ and the triple negative breast cancer (TNBC) cell line MDA-MB-468, as an example of an EGFR over-expressing cell line (1×10^6 receptors/cell)¹⁵⁰. Figure 2.1a shows (i) a representative reconstructed dSTORM image of fluorescently labeled EGFR of an entire cell, (ii) a magnified $4 \mu\text{m} \times 4 \mu\text{m}$ section of the reconstructed image, (iii) the corresponding pseudo-colored cluster map (red areas indicate locations of high EGFR density), as well as the associated (iv) thresholded binary cluster map, and (v) Ripley’s H -function as a function of separation for MDA-MB-468 (−/+) EGF and HeLa (−/+) EGF (from top to bottom). The local clustering of EGFR is illustrated in the cluster maps shown in Figure 2.1a(iii), which contain the value of Ripley’s L -function evaluated at a spatial scale of $r = 80$ nm. The pseudo-colored cluster maps were thresholded by an $L(r)$ cutoff value to define clusters, and the resulting binary cluster maps are shown in Figure 2.1a(iv). The Ripley’s H -functions in Figure 2.1a(v) for MDA-MB-468 (−/+) EGF are quite broad and remain positive on length scales up to 1000 nm, whereas in HeLa (−/+) EGF, the positive spatial correlation disappeared on length scales beyond 600 nm. Importantly, the H -functions peak at separations between 80 and 120 nm for MDA-MB-468 and HeLa (−/+) EGF, which indicates strong spatial EGFR clustering on the length scale of tens of nanometers.

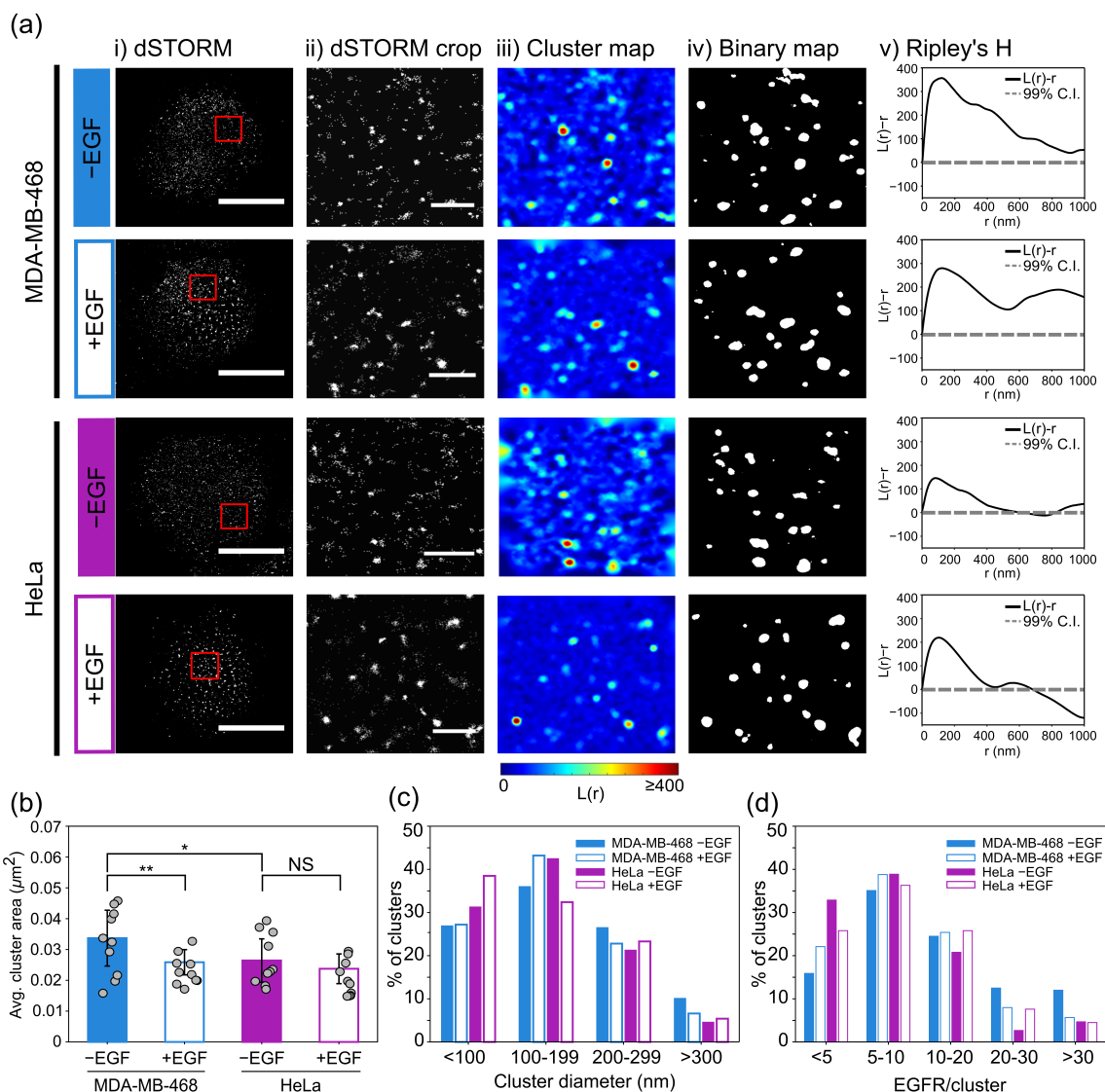


Figure 2.1: dSTORM imaging of EGFR clustering. (a)(i) Representative reconstructed dSTORM images of MDA-MB-468 (-/+ EGF (top) and HeLa (-/+ EGF (bottom). Scale bar: 10 μm . (ii) Regions (4 μm \times 4 μm) outlined in red are enlarged and shown with the corresponding (iii) cluster map according to a pseudocolor scale bar, (iv) thresholded binary maps, and (v) Ripley's H -distributions. Scale bar: 1 μm . (b) Plot of average cluster area for all experimental conditions. Each data point represents the average cluster area for two 4 μm \times 4 μm regions per cell for a total of 10 cells each. Lines represent average \pm standard deviation (SD). * $P < 0.05$, ** $P < 0.01$, and not significant (NS) by the unpaired two-sample t -test. (c) Histogram of EGFR cluster diameter distribution. (d) Histogram of EGFR per cluster. Reprinted with permission from reference⁴⁶, © 2019 American Chemical Society.

Figure 2.1b summarizes the average cluster area (obtained from the binary cluster map) for two randomly selected $4 \mu\text{m} \times 4 \mu\text{m}$ areas in the central region of 10 cells. The average cluster area for MDA-MB-468 decreases significantly from 0.034 ± 0.009 to $0.026 \pm 0.006 \mu\text{m}^2$ after EGF addition. For HeLa, a slight decrease from 0.026 ± 0.008 to $0.024 \pm 0.006 \mu\text{m}^2$ is observed after EGF addition, but the difference in the average cluster area ($-/+$) EGF is not statistically significant. The cluster diameter histograms in Figure 2.1c provide an overview of the distribution of effective cluster diameters of 0-99, 100-199, 200-299, and >300 nm for the investigated conditions. For both MDA-MB-468 and HeLa ($-$ EGF), clusters with a diameter between 100 and 199 nm have the highest probability, but the contribution from larger clusters is higher for MDA-MB-468 $-$ EGF than for all other conditions. For MDA-MB-468 $+$ EGF, the contribution from these larger cluster diameters decreases and the contribution from 100 to 199 nm is further increased. After EGF addition to HeLa, the contribution from clusters with a diameter <100 nm is increased, primarily at the expense of decrease in clusters with diameters between 100 and 199 nm. The average EGFR cluster sizes for MDA-MB-468 and HeLa ($-/+$) EGF were determined as 172 ± 99 nm/ 155 ± 91 nm and 150 ± 90 nm/ 145 ± 90 nm, respectively. The number of localizations in each cluster obtained from the binary map can be used to estimate the number of EGFR per cluster if one accounts for the number of Alexa-647 dyes conjugated to an individual anti-EGFR antibody. The resulting numbers of EGFR/cluster for the different experimental conditions are shown in Figure 2.1d. In the absence of stimulation, MDA-MB-468 contains an average of 15 EGFR/cluster compared with only 10 EGFR/cluster for HeLa. The over-expressing MDA-MB-468 has a higher EGFR expression level than HeLa, which corresponds to an increase in the percentage of intermediate to larger sized clusters containing more than 10 EGFR. Additionally, activation of EGFR with free EGF results in a higher number

of clusters with < 10 EGFR for both cell lines. Overall, a higher number of clusters with less EGFR is consistent with the increase in small to intermediate-sized clusters with diameters less than 199 nm and a decrease in the average cluster area.

2.2 Hyperspectral Plasmon Coupling Microscopy for Characterizing EGFR Heterogeneity

We hypothesize that spectral imaging of NPs targeted at EGFR can detect large-scale EGFR clustering and discern between different levels of clustering (Figure 2.2a). The distance-dependent plasmon coupling between Au NP labels¹⁵¹⁻¹⁵⁴ with diameter, D , forms the basis for the spectral detection of large-scale receptor clustering. NPs can bind to two EGFR proteins without structural interference if the interparticle separation is $d > D$. If binding to the EGFR localizes two NPs within the range $D < d < 2D$, the NPs are sufficiently close for electromagnetic coupling to occur and the resulting hybridization of the plasmons^{155,156} induces a spectral red shift as a quantifiable observable of clustering (Figure 2.2b). As the probability of receptors with separations $d < 2D$ increases with EGFR clustering, a spectral red shift of the resonance wavelength of the NP labels relative to that of an individual NP is an indicator of a local increase in EGFR density. Additional factors, such as the ratio of NP diameter to EGFR cluster size and the number of NPs bound per cluster, determine the magnitude of the experimentally observed spectral shift. In a previous study, Abulrob et al. used near-field scanning optical microscopy to characterize the heterogeneous distribution of EGFR in the plasma membrane of HeLa cells and reported an average cluster size of approximately 150 nm.³³ Informed by this number and our dSTORM results, which revealed average cluster sizes between 145 ± 90 and 172 ± 99 nm for the experimental conditions tested, we used lipid-coated Au NPs with a diameter of 72.17 ± 2.16 nm as labels in this work because they are small enough

to allow binding of multiple NPs in EGFR-enriched membrane domains but, at the same time, have large scattering crosssections to ensure a strong contrast relative to the cellular environment.¹⁵⁷ The NPs were coated with a thin membrane assembled primarily from 1,2-dipalmitoyl-sn-glycero-3-phosphocholine (DPPC), cholesterol, and a small fraction of biotinylated lipid. The lipids were tethered to the NPs via octadecanethiol as described previously.^{118,158,159} The incorporation of biotin into the membrane of the NPs facilitated a biotin-avidin based labeling of EGFR as outlined in Figure 2.2a.

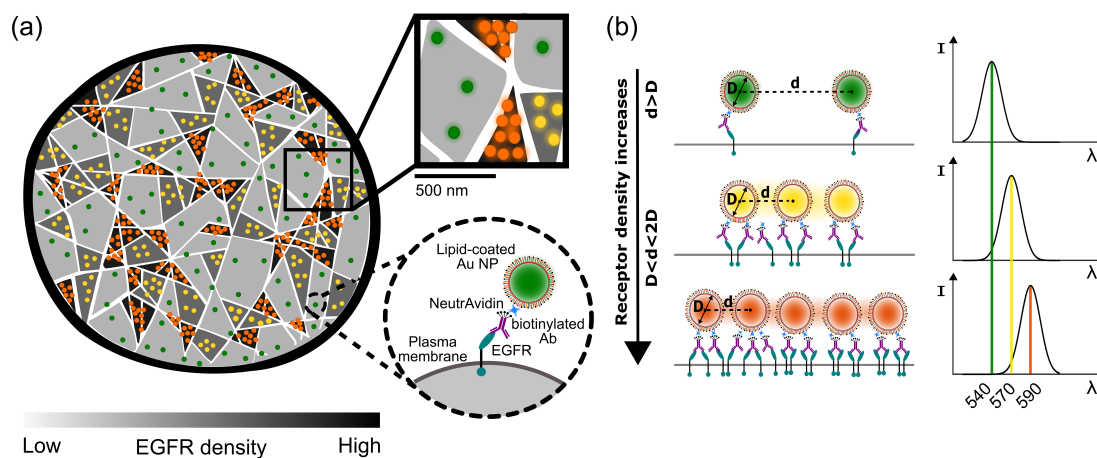


Figure 2.2: Detection of EGFR heterogeneity using Au NP labels. (a) Schematic illustration of using Au NP labels to detect large-scale EGFR clustering. As receptor density increases, so does the NP density. The inset on the upper right illustrates a model of the cortical actin network (white) as a structure-defining component that patterns large-scale EGFR clustering. Dashed circle on the lower right shows the immunolabeling strategy based on biotin–avidin binding between biotinylated anti-EGFR antibody (Ab) and biotinylated lipid-coated Au NPs. (b) Decrease in the average interparticle separation (d) of NP labels with diameter (D) leads to a spectral red shift, which is an observable of receptor clustering. Reprinted with permission from reference⁴⁶, © 2019 American Chemical Society.

2.3 Optical Analysis of EGFR Heterogeneity through Plasmon Coupling between NP Labels

The dSTORM results facilitate testing the sensitivity of hyperspectral PCM for differentiating between different EGFR cluster sizes. In Figure 2.3a, digital color images of NP labels (immobilized on glass) before and after incubation with cells have the characteristic green color of monodisperse Au NPs.

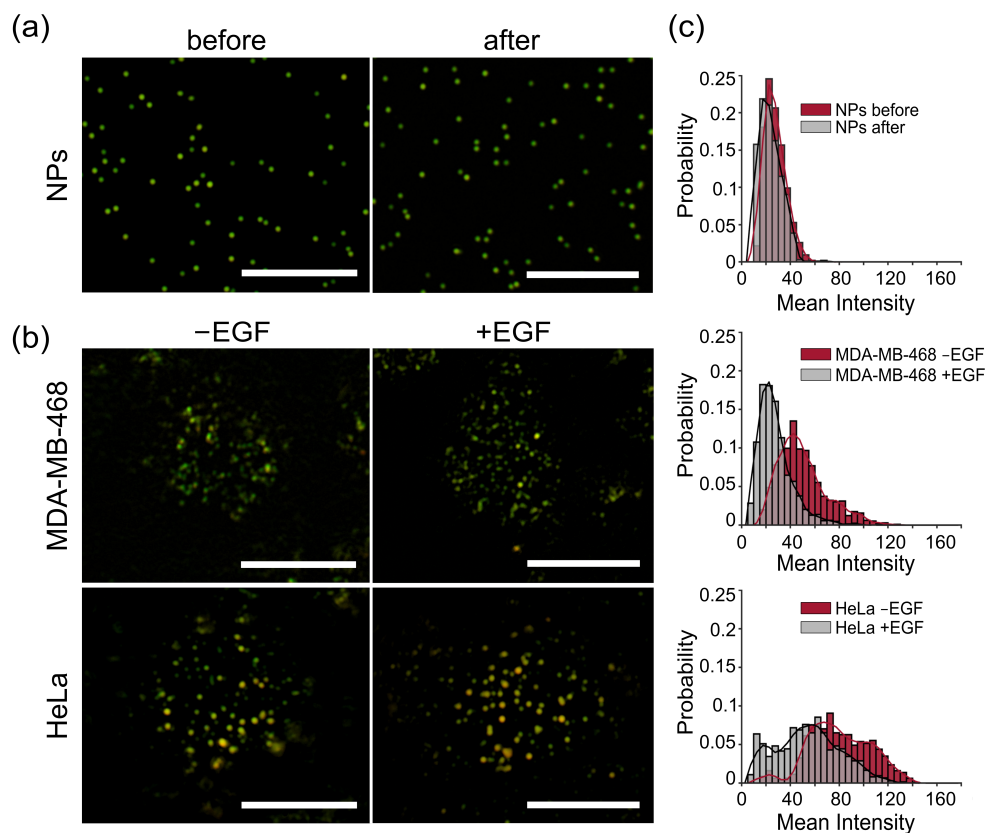


Figure 2.3: Optical analysis of digital color images of NP labels. (a) Digital color images of NP labels immobilized on glass before and after incubation with cells. Scale bar: 10 μm . (b) Digital color images of NP-labeled MDA-MB-468 without and with 10 nM EGF stimulation (top) and HeLa without and with 10 nM EGF stimulation (bottom). Scale bar: 10 μm . (c) Histogram of mean intensity distribution of NP labels for NP controls (top), MDA-MB-468 (-/+ EGF) (middle), and HeLa (-/+ EGF) (bottom). Reprinted with permission from reference ⁴⁶, © 2019 American Chemical Society.

Figure 2.3b shows digital color images of NP labels bound to MDA-MB-468 and HeLa cells before and after addition of 10 nM EGF. This concentration is 10 times higher than the dissociation constant of EGF to EGFR and ensures stoichiometric binding of ligand to the targeted receptor.^{149,160} Tests of the spatial randomness of the distribution of the optically discernible NPs performed with the Hopkins statistic, H ¹⁶¹, for 50 cells per experimental condition (Figure 2.4) reveal nearly random NP distributions ($H \approx 0.5$) on length scales above the diffraction limit at $\lambda = 540$ nm for all experimental conditions.

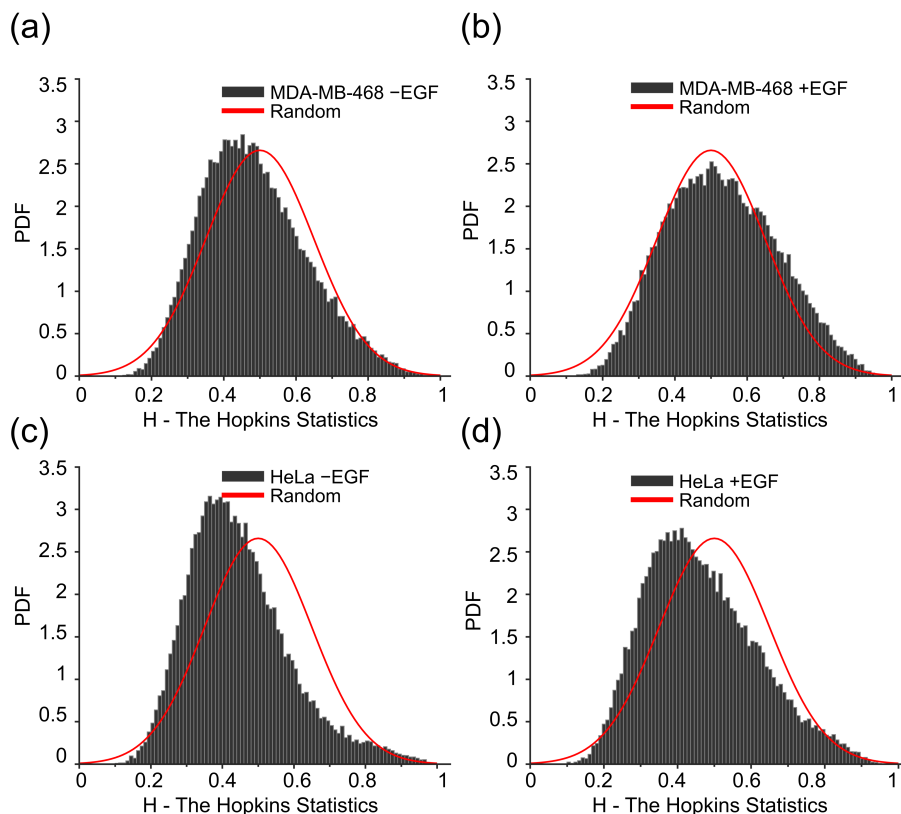


Figure 2.4: Hopkins Statistics of NP labels bound to MDA-MB-468 (-/+ EGF and HeLa (-/+ EGF) in diffraction-limited digital color images. Average Hopkins Statistics for spatial randomness for (a-b) MDA-MB-468 (-/+ EGF and (c-d) HeLa (-/+ EGF). The red curve is a random distribution centered at 0.5. Reprinted with permission from reference⁴⁶, © 2019 American Chemical Society.

However, the apparent difference in color of the NPs targeted to EGFR on MDA-MB-468 and, in particular, to HeLa when compared with the NP controls suggests clustering on length scales below the diffraction limit. To independently confirm NP clustering on subdiffraction limit length scales, we analyzed the NP-labeled cells after fixation through scanning electron microscope (SEM) at a much higher spatial resolution (Figure 2.5). Inspection of the SEM micrographs revealed discrete NP clusters with H values shifted closer to 1, confirming a significant level of clustering of NP labels bound to MDA-MB-468 and HeLa on subdiffraction limit length scales.

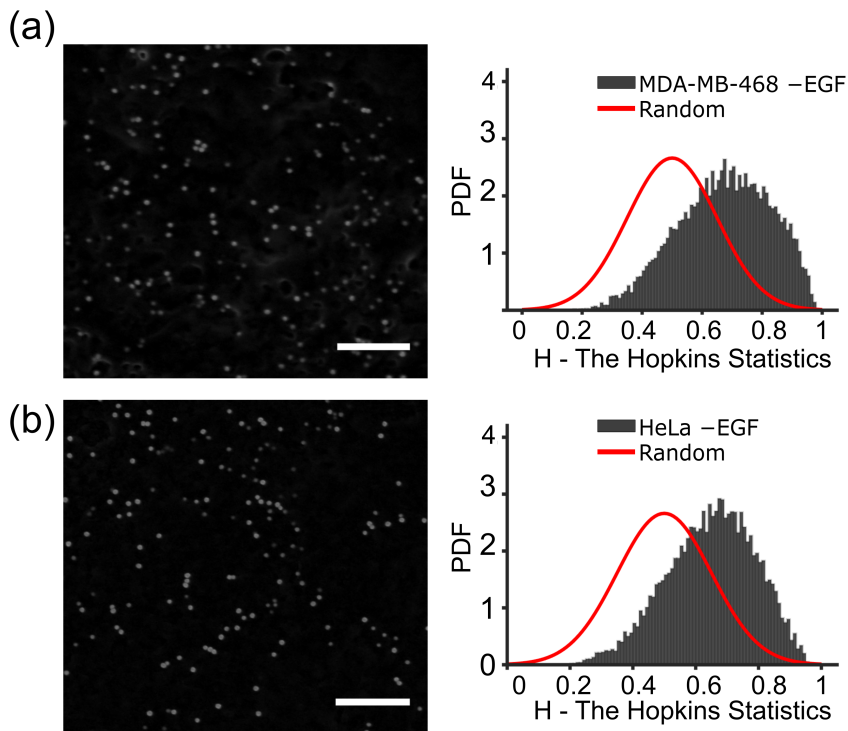


Figure 2.5: Hopkins Statistics for spatial randomness of NP labels. Representative SEM images of EGFR distribution on the plasma membrane and average Hopkins Statistics for spatial randomness on $4 \times 4 \mu\text{m}^2$ areas for (a) MDA-MB-468 (–EGF) and (b) HeLa (–EGF). Scale bar: $1 \mu\text{m}$. The red curve is a random distribution centered at 0.5. Reprinted with permission from reference⁴⁶, © 2019 American Chemical Society.

Intriguingly, the color of the NPs bound to HeLa are overall red-shifted relative to those bound to MDA-MB-468 and the NP controls in Figure 2.3a,b. This color change indicates a stronger electromagnetic coupling between NP labels for HeLa than for MDA-MB-468. This trend is also consistent with a higher average intensity of NP scatterers¹³⁰ on HeLa than on MDA-MB-468 or NP controls (Figure 2.3c). EGFR activation through EGF decreases the mean scattering intensity for both MDA-MB-468 and HeLa, suggesting less NP clustering after ligand stimulation.

2.4 Wide-Field Ratiometric Analysis of NP Labels for Quantifying Receptor Clustering

To quantify the spectral differences between NP labels bound to HeLa and MDA-MB-468 and to characterize more subtle differences between cells before and after EGFR activation ($-/+$) EGF, we measured in the next step the spectra of the NP labels using the hyperspectral PCM^{84,130} approach described in Figure 2.6a. In this technique, a monochromatic image was recorded every 10 nm between 540 and 650 nm to generate a hyperspectral composite image. Importantly, each pixel in the composite image contains an entire spectrum and information about the relative intensities of NPs from different wavelength channels (Figure 2.6b). The typical spatial resolution (resolving power) of discrete NPs in our set-up was $\Delta x = 651$ nm as determined by the full width at half maximum (FWHM) of the fitted point spread function (PSF) of individual NPs (Figure 2.6c). This imaging method provides spectral and spatial information of all scatterers in the field of view ($141 \mu\text{m} \times 141 \mu\text{m}$ at the chosen magnification) with an average localization precision of 1 nm for individual NP scatterers at the chosen acquisition time of 0.1 s. For spectral analysis of NP labels, we determined the resonance wavelength, λ_{peak} , defined as the wavelength channel with the highest intensity, for each NP pixel in the field of view (Figure 2.6a). The

distributions for NP labels as synthesized and after recovery from a solution incubated with cells peak at 550 nm and are nearly identical, confirming the stability of the NP labels.

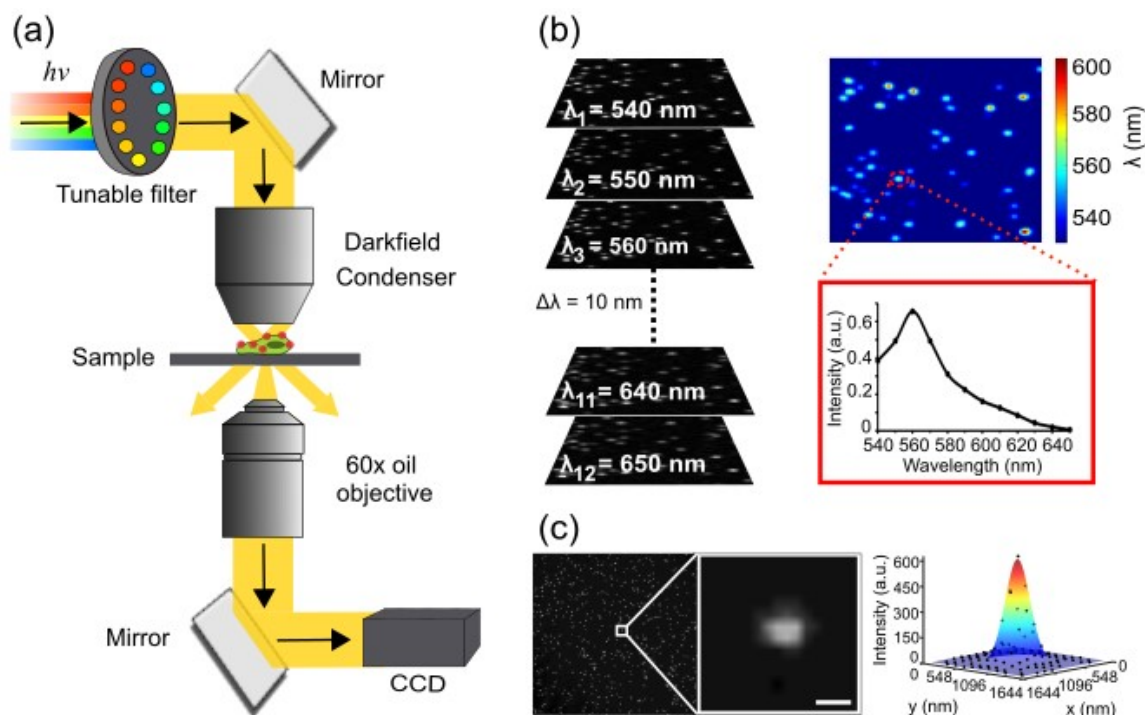


Figure 2.6: Schematic overview of hyperspectral PCM imaging approach. (a) Setup for hyperspectral PCM. (b) Acquisition of a monochromatic image from $\lambda = 540 - 650$ nm, every 10 nm, to generate a hyperspectral composite image. Each pixel in the composite image provides complete spectral information of the NP labels. (c) Representative CCD image of Au NPs immobilized on glass and an enlarged image showing an individual NP and the corresponding 2D Gaussian fit. Scale bar: 1 μm . Reprinted with permission from reference⁴⁶, © 2019 American Chemical Society.

In Figure 2.7b, the λ_{peak} distributions for both MDA-MB-468 and HeLa (-)EGF are broadened to longer wavelengths when compared with NPs immobilized on glass. Compared with NP controls, $\lambda_{peak} = 550$ nm still has the highest probability for MDA-MB-468 -EGF, but its value is decreased while the contributions from longer wavelengths have increased.

The shift to longer peak wavelengths is strongest for HeLa, for which the frequencies of $\lambda_{peak} = 550$ nm and $\lambda_{peak} = 560$ nm are lower and $\lambda_{peak} = 570$ is higher than for MDA-MB-468. This shift in the λ_{peak} distribution toward longer wavelengths is indicative of a NP subpopulation with a red-shifted plasmon resonance. The most prominent changes in λ_{peak} associated with NP binding to the cell surface for both HeLa and MDA-MB-468 in Figure 2.7a,b occur in a relatively narrow spectral window between $\lambda_{peak} = 540 - 580$ nm. We calculated the intensity ratio $R = I_{570}/I_{540}$ of the 540 ± 5 and 570 ± 5 nm intensity channels for all NP pixels as a measure for electromagnetic coupling.

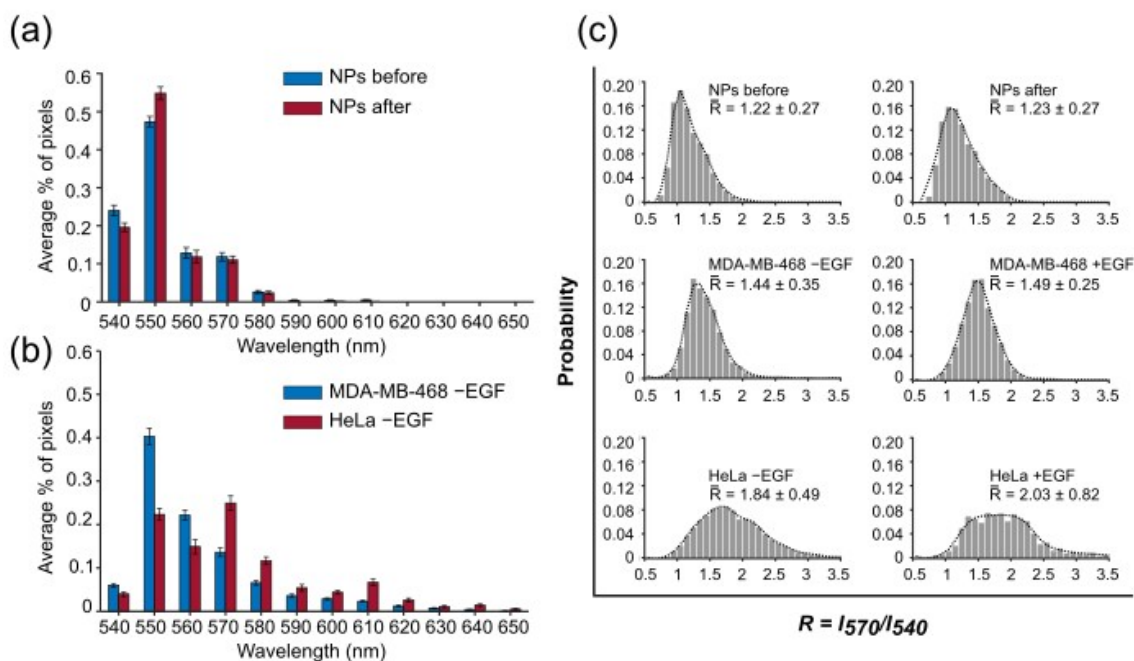


Figure 2.7: Resonance peak wavelength and ratiometric analysis of NP labels. (a) Peak wavelength, λ_{peak} , for NP labels in solution before and after incubation with cells. (b) λ_{peak} histograms for NP labels bound to MDA-MB-468 and HeLa (–EGF). Error bars in (a,b) are \pm standard error of the mean (S.E.M). (c) Histograms of $R = I_{570}/I_{540}$ for NP labels before and after incubation with cells (top row), NPs bound to MDA-MB-468 without and with 10 nM EGF treatment (middle row), and NPs bound to HeLa without and with 10 nM EGF treatment (bottom row). The data presented in (a - c) were collected from 50 cells (3 independent experiments). Reprinted with permission from reference⁴⁶, © 2019 American Chemical Society.

	R_{av}	Cluster diameter (nm)
MDA-MB-468 (-EGF)	1.44 ± 0.35	172 ± 99
MDA-MB-468 (+EGF)	1.49 ± 0.25	155 ± 91
HeLa (-EGF)	1.84 ± 0.49	150 ± 90
HeLa (+EGF)	2.03 ± 0.82	145 ± 90

Table 2.1: R_{av} (hyperspectral PCM) and Cluster diameter (dSTORM) Values

The histogram in Figure 2.7c shows a progressively increasing red shift (increase in R) relative to the NP controls ($R_{av} = 1.22$ and 1.23 , respectively, for NPs before and after recovery) in the sequence MDA-MB-468 -EGF ($R_{av} = 1.44$), MDA-MB-468 +EGF ($R_{av} = 1.49$), HeLa -EGF ($R_{av} = 1.84$), and HeLa +EGF ($R_{av} = 2.03$), where R_{av} is the average R value of the distribution. The differences in R between the cells as well as between the cells and the NP controls are significant with P values < 0.001 (unpaired two-sample t -test). The differences between the individual cell lines (-/+ EGF) are weaker than between the cell lines but still statistically significant with P values < 0.001 (unpaired two-sample t -test). The R_{av} values provide a metric that can be compared with the effective cluster diameters determined by dSTORM. The corresponding values obtained from both imaging methods are summarized in Table 2.1. We determined a correlation coefficient of -0.8454 , confirming a negative correlation between R values and EGFR cluster size (Figure 2.8). Overall, the spectral analysis in Figure 2.7 confirms that NP binding to EGFR results in a spatial clustering of the labels with sufficiently small interparticle separation to induce significant spectral red shifts. Our analysis reveals that a ratiometric analysis of the intensities at 570 and 540 nm is well suited to discern the spectral differences between the investigated conditions. In principle, changes in the ambient refractive index can also induce a spectral shift between cell bound NPs and glass-bound NP controls. However, the refractive indices of glass ($n = 1.52$)¹⁶² and the cell membrane ($n = 1.46 - 1.60$)^{163,164} are similar and a refractive index difference alone is insufficient to account for the difference in R_{av} between HeLa and MDA-MB-468 (-/+ EGF).

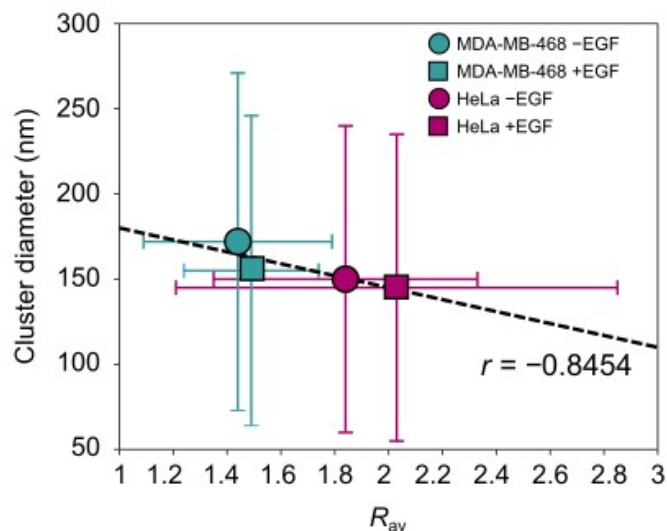


Figure 2.8: Correlation plot of R_{av} (hyperspectral PCM) and average EGFR cluster size (dSTORM) for MDA-MB-468 (-/+ EGF) and HeLa (-/+ EGF). The correlation coefficient is -0.8454 . Reprinted with permission from reference⁴⁶, © 2019 American Chemical Society.

2.5 Probing Changes in EGFR Clustering Induced by Disruption of Cortical Actin Network

EGFR is an actin binding protein and its distribution and clustering tendency can be influenced by the structural organization of the actin cytoskeleton.¹⁶⁵ To test the sensitivities of hyperspectral PCM and dSTORM for detecting potential differences in EGFR clustering after perturbation of the actin network, MDA-MB-468 cells were pretreated with Latrunculin A (Lat A), which sequesters free G-actin monomers and depolymerizes F-actin.¹⁶⁶ Confocal imaging of Lat A-treated cells in Figure 2.9a demonstrated that the activity of the inhibitor while cells maintained their overall shape. Figure 2.9 summarizes the $R = I_{570}/I_{540}$ distributions for NP labels targeted at EGFR, as determined by hyperspectral PCM of samples without and with Lat A treatment. We observed a significant red shift (increase in R) after Lat A treatment, with R_{av} (no treatment) = 1.44 and R_{av} (+Lat A) = 1.58 ($P < 0.001$, unpaired

two-sample t -test). The detected increase in $R = I_{570}/I_{540}$ after actin perturbation indicates that the average interparticle separation in Lat A treated cells are shorter, which suggests that the size of the EGFR clusters has decreased through Lat A treatment. Furthermore, fluorescence superresolution images acquired by dSTORM also show a trend of a small decrease in average cluster size from 0.034 ± 0.009 to $0.029 \pm 0.009 \mu\text{m}^2$ after actin perturbation, but the change is statistically not significant for the relatively small sample size (10 cells) investigated. Analysis of individual clusters from the dSTORM binary maps revealed an average EGFR cluster size of 158 ± 95 nm after actin perturbation in MDA-MB-468 cells.

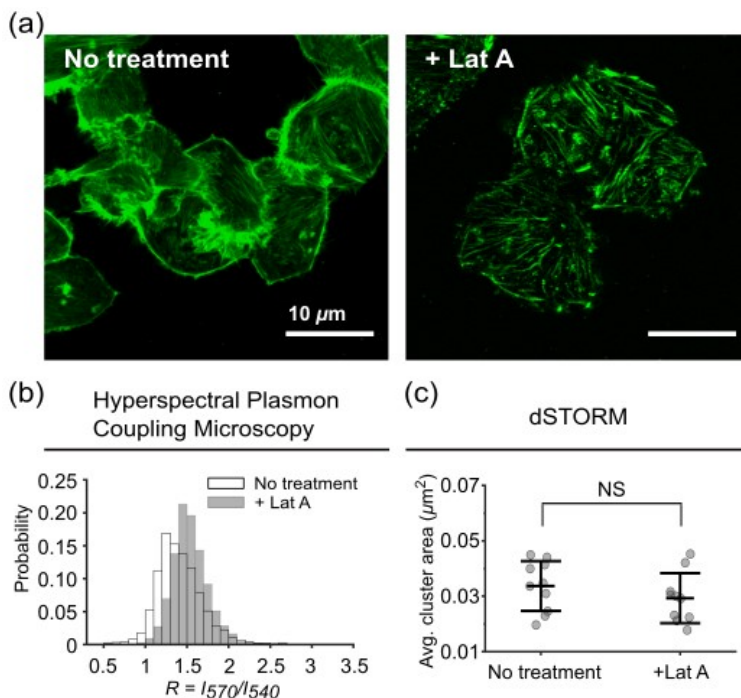


Figure 2.9: Hyperspectral PCM and dSTORM analysis of Lat A-treated cells. (a) Representative confocal images of untreated and 1 μM Lat A-treated MDA-MB-468 cells. Scale bar: 10 μm . (b) Histograms of $R = I_{570}/I_{540}$ for untreated and Lat A-treated MDA-MB-468 cells obtained from hyperspectral PCM. (c) Average cluster area for untreated and Lat A-treated MDA-MB-468 cells obtained from dSTORM. Each data point represents the average cluster area for two $4 \mu\text{m} \times 4 \mu\text{m}$ regions per cell. Lines represent average \pm SD. NS by unpaired two-sample t -test. Reprinted with permission from reference⁴⁶, © 2019 American Chemical Society.

2.6 Throughput Comparison of dSTORM Imaging and Hyperspectral Plasmon Coupling Microscopy for Analysis of Single Cells

Although spectral imaging of plasmon coupling between NP labels does not allow for a direct quantification of EGFR cluster size, as in the case of dSTORM, our data confirm that the hyperspectral PCM approach can reliably detect differences and changes in EGFR cluster size. Considering the size of the NPs used in this work, it is clear that PCM is not as universally applicable as other superresolution microscopies that use smaller labels. However, for the application in this work, characterization of the large-scale clustering of EGFR, the chosen NP size made the plasmon coupling assay very sensitive to changes in EGFR clustering. In fact, the conclusions from the spectral shift analysis are in very good agreement with the dSTORM results. Both techniques differ, however, greatly in experimental throughput (Figure 2.10). In hyperspectral PCM, all the required information to quantify the spectra of the NPs bound to EGFR were collected within 1.2 s. At 1.2 s for dSTORM, only 16 localizations have been localized leading to an incomplete and not useful cluster map. To obtain sufficient localizations to reconstruct a dSTORM image, at least 10,000 frames needed to be recorded over a total acquisition time of 600 s. Importantly, in the time it takes to record 10,000 frames in dSTORM for 1 field of view, data can be acquired for roughly 500 field of views using hyperspectral PCM, which underlines the great advantage in scalability for this approach. For important sensing and screening applications, the ability to detect relative changes in receptor clustering for a large number of individual cells in a relatively short time may outweigh the advantages provided by precise localization of individual receptor molecules in a cluster.

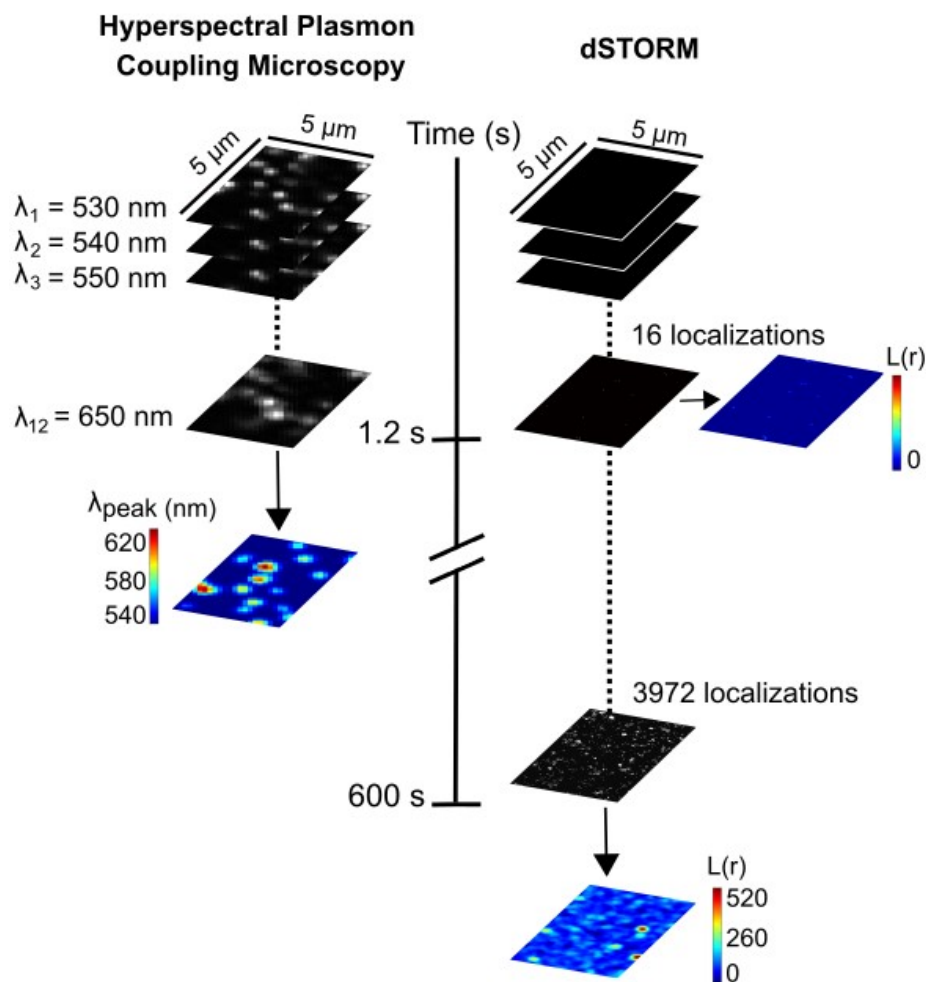


Figure 2.10: Comparison of hyperspectral PCM and dSTORM applied for optical mapping of NP labels and fluorescence labeling of EGFR on independent $5 \mu\text{m} \times 5 \mu\text{m}$ area of HeLa cell, respectively. At the same acquisition time of 0.1 s per frame, the cluster map of peak resonance wavelength for hyperspectral imaging is complete in 1.2 s, while for dSTORM, only 16 localizations have been localized leading to an incomplete cluster map. A complete cluster map for dSTORM requires thousands of frames for sufficient localizations (approximately 600 s). Reprinted with permission from reference⁴⁶, © 2019 American Chemical Society.

2.7 Conclusion

In conclusion, hyperspectral PCM and fluorescence superresolution dSTORM microscopy were both applied to investigate EGFR clustering in MDA-MB-468 and

HeLa cells. The comparative studies suggest that a systematic spectral analysis of the distance-dependent plasmon coupling between NP facilitates a sensitive detection of differences in the size of EGFR clusters in both cell lines as well as changes induced by the addition of EGF or dissolution of cortical actin network as indicated by the dSTORM data. The successful distinctions of changes in clustering patterns under different experimental conditions using bright and easy to image NP labels emphasizes the potential of this approach for achieving rapid characterization of receptor clustering in a large cell population with single cell resolution in a conventional widefield microscope. Spatial clustering of EGFR warrants increased interaction frequencies between EGFR (and coreceptors) and favors their association into dimers^{22,167} and higher oligomers^{41,57,168}. Given the role of EGFR oligomerization in enhancing receptor phosphorylation, receptor clustering could be a regulation mechanism to control and modulate ligand binding-induced receptor signaling.³⁴⁻³⁶ The putative regulatory role of receptor clustering creates a need for tools that can characterize receptor clustering with adequate throughput. This work confirms hyperspectral PCM of NP labels as a scalable analytical tool for surveying the spatial clustering of receptors in the plasma membrane. Through automation of the image acquisition procedure, the approach could provide a useful assay for receptor clustering (and its heterogeneity) to complement existing techniques for the quantification of expression levels of a cell surface receptor in a cell population, such as flow cytometry. The NP-based imaging tool paves a path toward including large-scale receptor clustering on the single cell level as a biomarker in the characterization of heterogeneous cell populations.

2.8 Materials and Methods

Cell Culture and Treatments. MDA-MB-468 cells were cultured in advanced Dulbecco's modified Eagle medium (DMEM) with 10% fetal bovine serum, L-glutamine,

penicillin, and streptomycin at 37 °C with a humidified atmosphere containing 5% CO₂. HeLa cells were cultured under the same conditions. Prior to experiments, MDA-MB-468 and HeLa cells were maintained in serum-free DMEM for 16 h. Cells to be imaged under dSTORM and hyperspectral PCM were cultured in glass bottom petri dishes to approximately 80% confluency for experiments. EGF-stimulated cell samples were serum-starved for 16 h and incubated with 10 nM EGF (Thermo Fisher Scientific) for 10 min at 37 °C before washing with 1× phosphate-buffered saline (PBS) and fixation with 4% paraformaldehyde. Cell samples in which actin was depolymerized were serum-starved for 16 h and incubated with 1 μM of Latrunculin A (Sigma-Aldrich) for 10 min at 37 °C before washing with PBS and fixation with 4% paraformaldehyde.

dSTORM Sample Preparation. Cells were immunostained after fixation with an Alexa-Fluor 647-conjugated antibody against EGFR (0.5 μg/mL, Thermo Fisher Scientific) in the dark for 20 mins and then washed three times with PBS for 5 min each. For dSTORM imaging, the oxygen-scavenging buffer (50 mM Tris and 10 mM NaCl solution to pH 8) contained 0.5 mg/mL glucose oxidase, 40 μg/mL catalase, 10% glucose (w/v), and 10 mM mercaptoethylamine. The buffer solution was added to the glass bottom petri dish prior to imaging.

dSTORM Imaging. For imaging, a 642 nm laser and an electron-multiplying charge-coupled device (CCD) were used (Andor iXonEM+ 897 back-illuminated EM-CCD). dSTORM imaging was performed on a Zeiss ELYRA PS.1 microscope using an α Plan-Apochromat 100× oil objective with numerical aperture (NA) 1.46. Samples were imaged in TIRF illumination mode with the TIRF angle adjusted to ensure that the focal plane was on the apical surface of the cells.¹⁶⁹ A total of 10,000 raw images were acquired per cell with an exposure time of 50 ms for the reconstruction of superresolution images. One single reconstructed dSTORM image was acquired in

less than 10 mins. The average localization precision and spatial resolution was 27 nm and 62 nm, respectively. Single-molecule localizations were fitted to a 2D Gaussian using the Zeiss Zen Black software that was equipped with the imaging system to obtain histograms of localization precision. The spatial resolution was estimated by Fourier ring correlation analysis¹⁷⁰ using SharpVisu¹⁷¹ software on MATLAB.

dSTORM Data Analysis. dSTORM images were reconstructed from raw image TIFF stacks with the ImageJ plug-in QuickPALM¹⁷². For each frame, localizations corresponding to single emission events were identified with a minimum SNR of 2. The x-y drift was corrected post-acquisition using a cross-correlation method via SharpViSu¹⁷¹ software on MATLAB. The drift-corrected x-y coordinates were imported into ClusterVisu¹⁷¹ MATLAB software for further quantitative cluster analysis as described by Owen et al^{173,174}. Avoiding cell edges, two non-overlapping regions of $4 \times 4 \mu\text{m}^2$ were selected per cell for quantitative cluster analysis in reconstructed images. To analyze the spatial distribution of molecules, Ripley’s K -function was calculated using ClusterViSu as shown in Eq. 2.1

$$K(r) = A \sum_{i=1}^n \sum_{j=1}^n \left(\frac{\delta_{ij}}{n^2} \right) \text{ where } \delta_{ij} = 1 \begin{cases} \text{if } \delta_{ij} < r \\ \text{otherwise } 0 \end{cases} \quad (2.1)$$

where $K(r)$ is the K -function, A is the area of the region being analyzed, δ_{ij} is the distance between points i and j , n is the total number of localizations within that area, and r is the spatial scale. In this analysis, concentric circles of radius r is drawn around each localization and counts how many other localizations are encircled and compared to a random distribution. The K -function can be normalized to scale with radius, which yields the H -and L -function as shown in Eq. 2.2:

$$H(r) = \sqrt{K(r)/\pi} - r = L(r) - r \quad (2.2)$$

For a spatially random distribution of localizations, $L(r) - r = 0$ for all r . For clustered localizations, this value is positive. The cluster map was generated by interpolating a surface plot with $L(r)$ for $r = 80$ nm of every localization as the z-axis and shown using a pseudo-color scale. Then the cluster map was thresholded by an $L(r)$ cut-off value of 120 - 130 to best define clusters to generate a binary map which contained quantitative information about the clusters. To estimate the number of EGFR/cluster, the number of localizations in a cluster was divided by 7.8, which is the ratio of Alexa 647 dye conjugated to a single anti-EGFR antibody.

Liposome and Particle Preparation. Lipid-coated NPs were prepared as described previously.^{118,158} The liposome mixture contained 55 mol % DPPC, 2 mol % 1,2-dioleoyl-sn-glycero-3-phospho-L-serine (DOPS), 4 mol % of DSPE-PEG(2000)-Biotin, and 39 mol % cholesterol in chloroform. This lipid mixture was tethered to the Au NP via octadecanethiol by incubating for 17 h on a shaker. The lipid-coated NPs were subsequently dialyzed overnight in Milli-Q water with nuclepore track-etched membranes (Whatman, pore size 0.015 μm). After dialysis, the NPs were centrifuged once (3.4k rpm, 10 min) to obtain the NP pellet. For cell experiments, this pellet was resuspended in 0.1 \times PBS to make a 150 pM NP solution.

Immunolabeling. To functionalize the anti-EGFR antibody (Sigma-Aldrich, clone 102618), 4 μL of biotin N-hydroxysuccinimide ester (100 mg/mL in DMSO) was mixed with 200 μL of 100 $\mu\text{g}/\text{mL}$ anti-EGFR antibody solution (1 \times PBS, pH 7.2) and kept on ice for 6 h. Excess biotin NHS ester was removed using a size exclusion Zeba column (7K MWCO). The functionalized antibody can be stored at -20° until further use. For labeling, cells were briefly rinsed with prewarmed 1 \times HBSS buffer and

then fixed by immersion in 4% paraformaldehyde for 10 mins at room temperature, followed by three washes with $1\times$ PBS for 5 mins each. Subsequently, the cells were incubated in $1\times$ PBS buffer containing 1% BSA for 30 mins at room temperature to block nonspecific binding. Cells were then washed three times with ice-cold $1\times$ PBS for 5 min each and then incubated with biotin-functionalized anti-EGFR antibody (diluted 1:10 in $1\times$ PBS) overnight at 4°C. The cells were then washed three times with $1\times$ PBS for 5 min each and incubated with 0.1 mg/mL of NeutrAvidin for 30 min at room temperature. After that, the cells were washed three times with ice-cold $1\times$ PBS for 5 mins each and $0.1\times$ PBS was used for the last wash. In the subsequent immunolabeling step, the petri dish was covered with 300 μ L of 150 pM of lipid-coated NPs in $0.1\times$ PBS for 30 mins at 4 °C and then washed three times with $0.1\times$ PBS for 5 mins each. The glass bottom petri dishes can then be transferred to a darkfield microscope for hyperspectral PCM imaging.

Hyperspectral Plasmon Coupling Microscopy. All optical imaging experiments were performed with an Olympus IX71 inverted microscope. For whitelight dark-field imaging, the samples were illuminated with a 100 W tungsten lamp through a high NA oil condenser (NA = 1.2 - 1.4) and the scattered light was collected through a $60\times$ oil objective (NA = 0.65). Digital color images were collected under whitelight illumination with a Nikon D5100 DSLR digital camera connected to the microscope through an eyepiece adapter. For hyperspectral imaging, a VariSpec-liquid crystal tunable filter was added in front of the darkfield condenser and used to tune the excitation wavelength. Hyperspectral images were captured with an electron multiplying CCD (Andor, Ixon+). A monochromatic image was obtained from 540 - 650 nm, every 10 nm, for a total of 12 images. The exposure time for each image was 0.1 s and the acquisition time for a full set of 12 images was 1.2 s. The spatial resolution was determined by fitting the PSF of randomly selected NP emitters with

a 2D Gaussian and determining the FWHM of the fit. For the localization precision, the Andor software was operated in photon counting mode to acquire images of NPs immobilized on glass. Random NPs were selected and fitted with a 2D Gaussian to obtain the number of detected photons. The localization precision was calculated as described by Ober et al.¹⁷⁵

Hyperspectral Image Processing. All image processing was performed using custom-written MATLAB codes. Monochromatic images were corrected for the background and excitation profile. For analysis, the central region of the cells (peripheral regions were excluded) and included only pixels whose total intensity was at least one standard deviation above the average cell background over the entire wavelength range. For λ_{peak} histograms, the intensity of the wavelength channel with the highest NP intensity was set to 1 and all others 0 for each pixel. For $R = I_{570}/I_{540}$ histograms, the ratio of NP intensities on the 570 nm and 540 nm channel were divided for every pixel. The mean intensity of NPs were determined using the particle picker plugin on ImageJ.

SEM Sample Preparation and Imaging. The culturing and immunolabeling procedures were identical to the sample preparation for hyperspectral plasmon coupling microscopy except the cells were plated on a $1 \times 1 \text{ cm}^2$ silicon substrate. After fixation and NP labeling, the silicon substrates containing NP labeled cells were washed three times with ice-cold $0.1 \times$ PBS and then briefly immersed in Milli-Q water to remove any remaining salt on the surface. The substrate was then gently blow-dried in a nitrogen stream and left overnight in a vacuum desiccator. The samples were imaged using Zeiss Supra40VP at 5.0 kV and a working distance of 8 mm.

Chapter 3

Multivalent Ligand-Nanoparticle Conjugates Amplify ROS Second Messenger Generation and Enhance Epidermal Growth Factor Receptor Phosphorylation

EGFR is heterogeneously distributed on the cellular surface and enriched in clusters with diameters of tens to hundreds of nanometers (Chapter 2). Multivalent presentation of EGF ligand on NPs provides an approach for controlling and amplifying the local activation of EGFR in these clusters. Signal activation^{42,84,85,138} can be tuned and amplified through multivalent ligand presentation on NPs by increasing binding affinity and influencing ligand-receptor interactions. A previous study by Reynolds et al. found for 0.8 micron diameter beads functionalized with different EGF ligand densities that EGF-induced ROS formation plays a role in the lateral propagation of EGFR activation.⁸⁵ Although it is established that multivalent presentation of EGF on smaller NPs can enhance EGFR activation and signaling,^{84,86,87} it remains untested whether multivalent EGF presentation on NPs also affects the intracellular EGFR-mediated ROS generation and how potential changes in the concentration of this second messenger acts back on EGFR activation in response to nanoconjugated EGF. The goal of this chapter is to characterize the multivalent enhancement

of EGF-induced ROS formation and to test its effect on EGFR phosphorylation. To that end, Au NPs with a diameter of 81 ± 1 nm were functionalized with two different EGF ligand densities (12 ± 7 EGF/NP (NP-EGF₁₂) and 87 ± 6 EGF/NP (NP-EGF₈₇)) and NP-EGF-induced ROS generation and EGFR phosphorylation were quantified in three breast epithelial cell lines: non-tumorigenic MCF10A cells, and EGFR-overexpressing MDA-MB-231 and MDA-MB-468 cells. In the EGFR over-expressing cell lines, NP-EGF₈₇ achieved a measurable multivalent enhancement of ROS, with peak ROS levels obtained for NP input concentrations c $ROS_{max} \leq 25$ pM (2175 pM EGF), that was EGFR and nicotinamide adenine dinucleotide phosphate oxidase (NOX) dependent. NP-EGF₁₂ failed to generate comparable ROS levels as NP-EGF₈₇ in the investigated NP input concentration range (0-100 pM). In cells with nearly identical numbers of bound NP-EGF₈₇ and NP-EGF₁₂, the ROS levels for NP-EGF₈₇ were systematically higher, indicating that the multivalent enhancement is not exclusively related to avidity but also to a stronger stimulation per NP. Importantly, the increase in EGF-induced ROS formation associated with EGF nanoconjugation at c ROS_{max} resulted in a measurable gain in EGFR phosphorylation, confirming that ROS generation contributes to the multivalent enhancement of EGFR activation in response to NP-EGF₈₇.

3.1 NP-EGF design and characterization

The design scheme of the NP-EGF used in this chapter is depicted in Figure 3.1a. The NP surface was passivated with two different thiol polyethylene glycol (PEG) molecules, (HS-CH₂CH₂-(C₂H₄O)₇₇-N₃, PEG 1) and (HS-(CH₂)₁₁-(C₂H₄O)₆-COOH, PEG 2). The NPs were grafted with azide-containing PEG 1 molecules to enable the covalent attachment of alkyne-functionalized EGF through the Cu(I) catalyzed 1,3-dipolar cycloaddition reaction¹⁷⁶. The negatively charged and shorter PEG 2

molecules were incorporated to stabilize the NPs. NP-EGF with two distinct EGF ligand densities of 12 ± 7 EGF/NP (NP-EGF₁₂) and 87 ± 6 EGF/NP (NP-EGF₈₇), as quantified through a human EGF enzyme-linked immunosorbent assay (ELISA) (Figure 3.1b), were prepared by adjusting the concentration of alkyne-functionalized EGF and catalyst mixture as well as the incubation time for the cycloaddition reaction. The EGF surface loadings of NP-EGF₁₂ and NP-EGF₈₇ correspond to average EGF surface densities of $6.0 \times 10^2 \mu\text{m}^{-2}$ and $4.3 \times 10^3 \mu\text{m}^{-2}$, respectively. SEM images of the prepared NP-EGF show a monodisperse distribution of spherical NPs (Figure 3.1c).

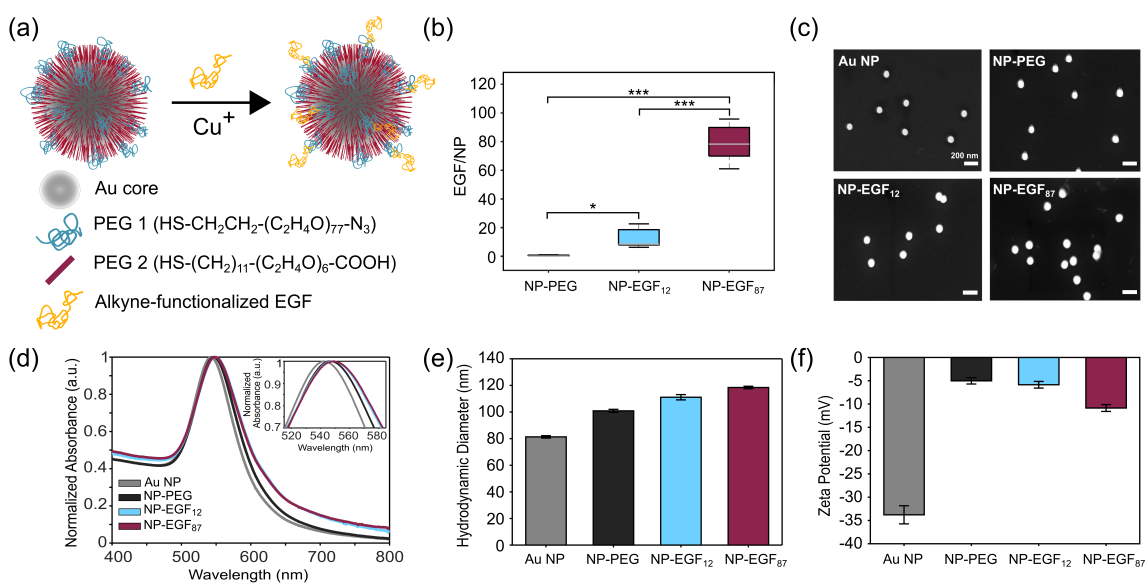


Figure 3.1: Schematic of NP-EGF design. (a) 81 ± 1 nm diameter spherical Au NPs are functionalized with PEG 1 (HS-CH₂CH₂-(C₂H₄O)₇₇-N₃) and PEG 2 (HS-(CH₂)₁₁-(C₂H₄O)₆-COOH) in a nominal ratio of 10:1. Alkyne-functionalized EGF was tethered to the azido group of PEG 1 through Cu(I) catalyzed 1,3-dipolar cycloaddition reaction. (b) Number of EGF bound per NP as quantified using Human EGF ELISA. (c) Representative SEM images of citrate-stabilized Au NP, NP-PEG, NP-EGF₁₂, and NP-EGF₈₇. Scale bar: 200 nm. (d) UV-Vis spectra, (e) hydrodynamic diameters, and (f) zeta potentials for citrate-stabilized Au NPs, NP-PEG, NP-EGF₁₂, and NP-EGF₈₇. The data shown in b, e, f are from at least 3 independent experiments. All values are means, and error bars are \pm s.e.m. Significance was measured using student's *t*-test, * $P < 0.05$, ** $P < 0.01$, *** $P < 0.001$.

The peaks in the UV-Vis spectra of NP-EGF are red-shifted by up to 2 nm for NP-EGF₁₂ and NP-EGF₈₇ relative to pegylated NPs (Figure 3.1d), and the size distributions as determined by DLS show less than 20 nm increase in the hydrodynamic diameter after EGF attachment (Figure 3.1e). The zeta potential of the NPs increases after pegylation and then slightly decreases by up to 5.58 mV after binding of the negative EGF¹⁷⁷ to the pegylated NPs (Figure 3.1f). Overall, the observed spectral shifts and changes in the hydrodynamic diameter and zeta potential are consistent with a successful EGF functionalization of the NPs; the small magnitude of the observed changes in the average hydrodynamic diameter and UV-Vis spectra confirm that the NPs show no systematic agglomeration in the process of the functionalization.

3.2 EGF-mediated ROS generation is EGFR and NOX dependent

Three breast epithelial cell lines (MCF10A, MDA-MB-231, MDA-MB-468) with varying EGFR expression levels were chosen for the studies in this chapter (Figure 3.2a). The advanced TNBC cell lines, MDA-MB-231 and MDA-MB-468 overexpress EGFR and show much higher EGFR surface concentrations than the non-tumorigenic MCF10A. EGFR overexpression in breast cancer cell lines has been reported to correlate with elevated H₂O₂ levels.¹⁷⁸ Indeed, the detection of the intracellular cytoplasmic ROS using CellROX Deep Red demonstrates that MDA-MB-231 and MDA-MB-468 have significantly higher baseline ROS levels compared to MCF10A (Figure 3.3).

Next, the effect of free EGF on the cellular ROS levels was assessed to establish a benchmark for subsequent NP-EGF experiments. In Figure 3.2b, the cytoplasmic ROS levels generated as a function of exogenous EGF concentration (0.16, 1.6, 16, 80 nM) was measured after 10 min of stimulation because the peak in EGF-induced

ROS generation is known to occur within 15 min^{59,65}. EGF concentrations \geq 1.6 nM resulted in a significant increase of the cytoplasmic ROS levels for all 3 cell lines compared with the non-treated cell control. For MCF10A and MDA-MB-231, the cytoplasmic ROS increases in a concentration-dependent manner throughout the tested concentration range, but for MDA-MB-468, the increase in ROS levels off at an EGF concentration of 1.6 nM. Pretreatment of cells with the ROS scavenger, N-acetylcysteine (NAC) prior to EGF stimulation at 1.6 nM reduced the cytoplasmic ROS concentration for all 3 cell lines (Figure 3.2c). Likewise, the H₂O₂ scavenger, PEG-catalase, also resulted in a decrease in EGF-mediated H₂O₂ generation for all cell lines. Importantly, the EGFR-specific RTK inhibitor, AG-1478, also reduced the EGF-induced cytoplasmic ROS, which confirms that EGF-mediated ROS generation is EGFR dependent. EGFR-dependent ROS generation after EGF treatment is consistent with previous reports.^{59,61,65} NOX activation associated with EGFR activation as a result of EGF-mediated ROS generation has also been described.^{65,80} NOX are, however, not the only potential source of EGF-induced cytoplasmic ROS. The electron transport chain in the mitochondria is another major source of ROS production in many different cell types due to electron leakage into the cytosol^{179,180}. Since *a priori*, it is unclear what the relative contributions from NOX and mitochondria are to the detected ROS levels, different inhibitors were used to identify the origin of the EGF-induced cytoplasmic ROS. Inhibition of NOXs with either diphenyleneiodium (DPI) or apocynin led to a reduction in EGF-mediated ROS, whereas blocking the mitochondrial electron transport chain with rotenone did not inhibit EGF-mediated ROS production for any of the investigated cell lines (Figure 3.2c).

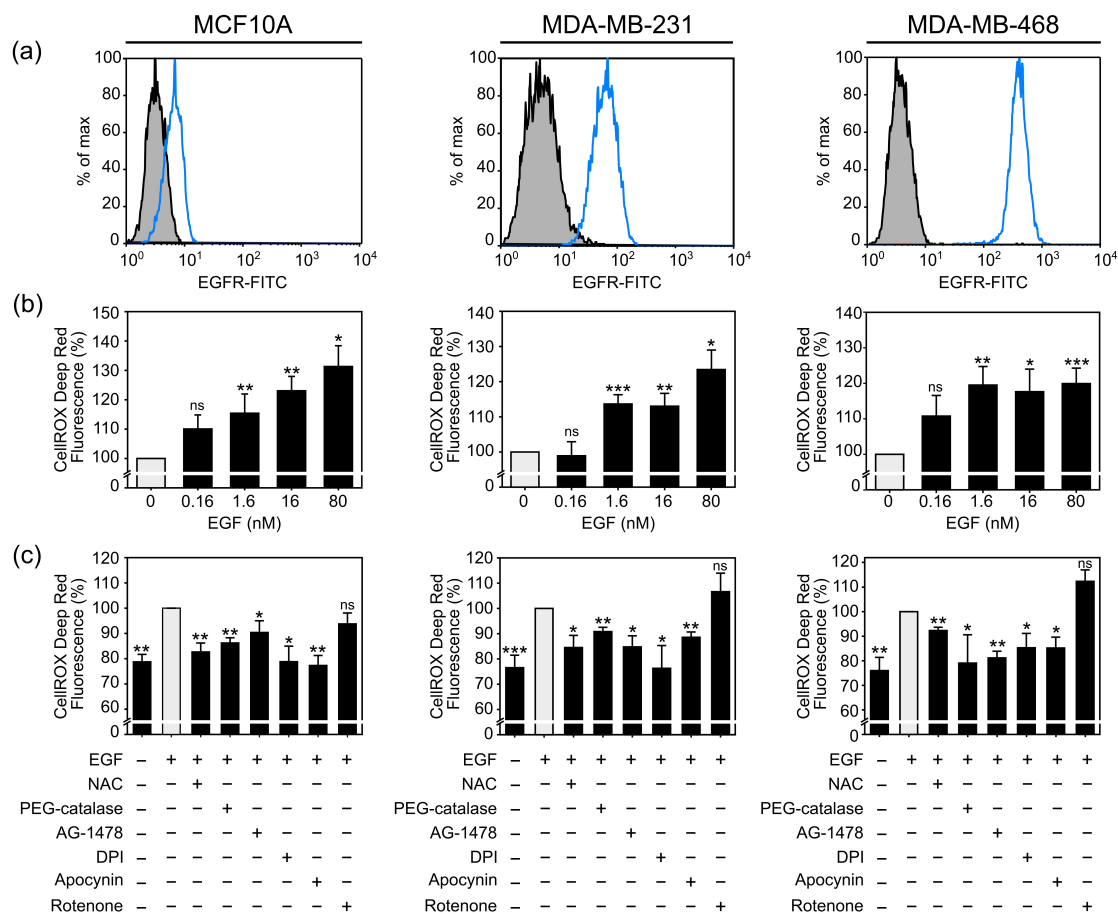


Figure 3.2: EGF-mediated ROS generation is EGFR and NOX dependent. (a) Relative EGFR expression level for MCF10A, MDA-MB-231, and MDA-MB-468 (from left to right) measured by flow cytometry. (Gray histogram is unlabeled cells and blue histogram is cells labeled with Anti-EGFR FITC) (b) Cytoplasmic ROS detected by CellROX Deep Red as a function of EGF concentration after 10 min stimulation. (c) EGF-mediated ROS generation detected with CellROX Deep Red. Cells were pretreated with NAC, PEG-catalase, AG-1478, DPI, apocynin, and rotenone where specified, prior to EGF stimulation (1.6 nM) for 10 min. The data shown are from 3 independent experiments. All values are means, and error bars are \pm s.e.m. Significance was measured using student's *t*-test, * $P < 0.05$, ** $P < 0.01$, *** $P < 0.001$, ns (not significant) when compared against non-treated cell control in (b) and cells treated with EGF only (1.6 nM) in (c).

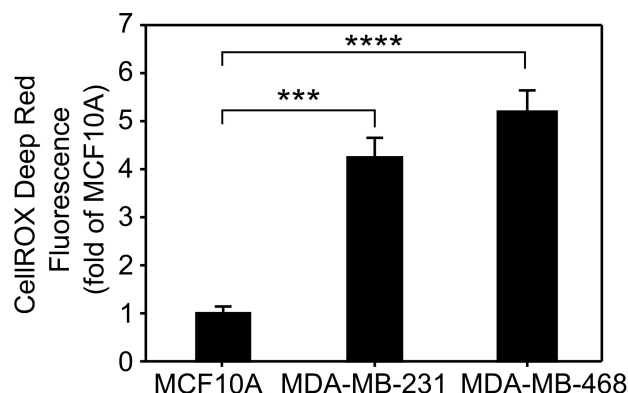


Figure 3.3: Basal intracellular ROS levels for breast cancer cell models for EGFR-overexpressing MDA-MB-231 and MDA-MB-468 relative to non-tumorigenic MCF10A as measured by CellROX Deep Red fluorescence. The data shown are from 3 independent experiments. All values are means and error bars are \pm s.e.m. Significance was compared to MCF10A using the student's *t*-test, *** $P < 0.001$, **** $P < 0.0001$.

Furthermore, at 1.6 nM EGF, detection of mitochondrial superoxide, the main source of mitochondrial ROS, was not significantly higher than for non-treated cell controls for all 3 cell lines (Figure 3.4). Overall, the inhibitors used in Figure 3.2c reveal that EGF-induced ROS formation depends on both EGFR and NOX activity.

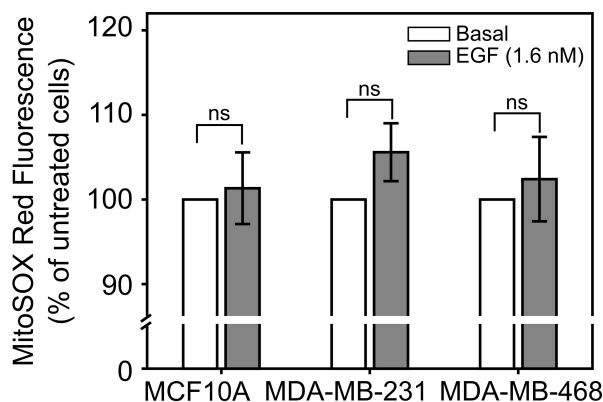


Figure 3.4: Mitochondrial superoxide ROS generation after 10 min incubation with 1.6 nM EGF as measured by MitoSOX Red fluorescence for MCF10A, MDA-MB-231, and MDA-MB-468. The data shown are from 3 independent experiments. All values are means and error bars are \pm s.e.m. Significance was compared to untreated cells (basal) using student's *t*-test, ns (not significant).

3.3 Multivalent Enhancement of EGF-mediated cytoplasmic ROS Generation

Cytoplasmic ROS levels generated by NP-EGF₁₂ and NP-EGF₈₇ were quantified after a 10 min incubation of cells with NPs in the concentration range of 0-100 pM. NP-PEG (no EGF) was included as a control. The global intracellular ROS generation was measured as a % change of CellROX Deep Red fluorescence signal relative to the non-treated cell control (dashed black line) as shown in Figure 3.5.

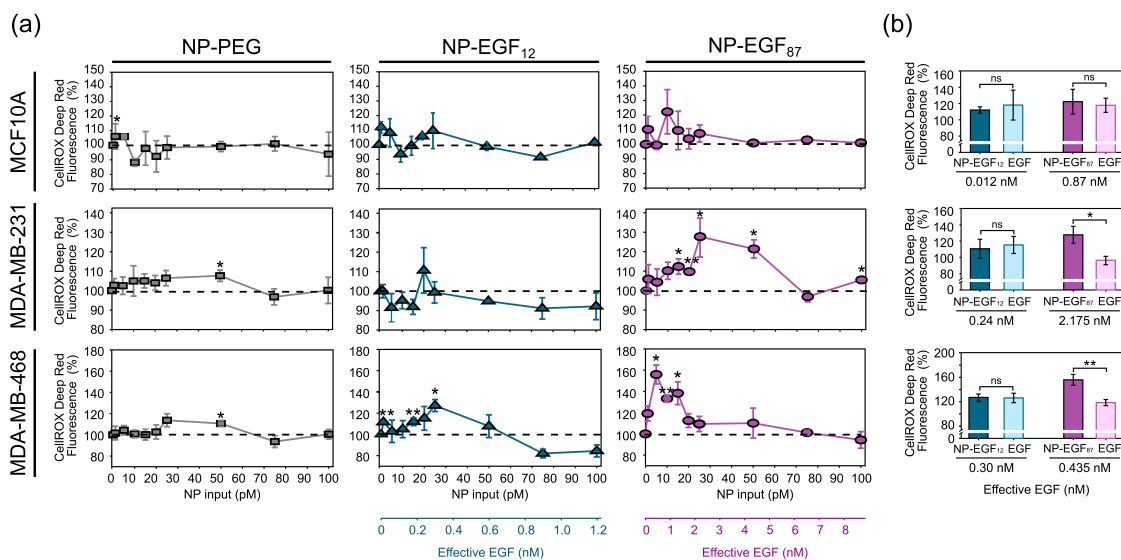


Figure 3.5: Cytoplasmic ROS generation of NP-PEG and NP-EGF. (a) Cytoplasmic ROS generation after 10 min incubation of NP-PEG (gray squares), NP-EGF₁₂ (blue triangles), and NP-EGF₈₇ (purple circles) with MCF10A, MDA-MB-231, and MDA-MB-468 (top to bottom). Black dashed line shown at 100% is used to indicate the non-treated cell control. The second x-axis corresponds to the effective EGF concentration (NP input concentration multiplied by EGF ligand density). (b) Cytoplasmic ROS generation for NP-EGF₁₂, NP-EGF₈₇, and free EGF at effective EGF concentration corresponding to c ROS_{max} for MCF10A, MDA-MB-231 and MDA-MB-468 (from top to bottom). The data shown are from 3 independent experiments. All values are means, and error bars are \pm s.e.m. Significance was measured using student's t -test, * $P < 0.05$, ** $P < 0.01$.

For NP-EGF₁₂ and NP-EGF₈₇, the x-axis is given both as NP input as well as effective

EGF concentration. ROS generation in response to NP-PEG control was negligible for almost all concentrations, except at 5 pM in MCF10A, and 50 pM for both MDA-MB-231 and MDA-MB-468. In these cases, there was a small but significant increase in ROS. For NP-EGF₁₂, statistically significant increases in cytoplasmic ROS were only detected for MDA-MB-468 at 1, 15, and 25 pM. NP-EGF₈₇ had a substantially larger effect on ROS generation. For MCF10A, a peak increase in ROS of 22% ($P = 0.1404$) was obtained for 10 pM of NP-EGF₈₇, and for MDA-MB-231 an increase of 27% ($P = 0.0286$) was detected at 25 pM. For MDA-MB-468, the peak occurred at an even lower input concentration of 5 pM NP-EGF₈₇ (56% increase, $P = 0.0123$). The NP input concentrations that yield the highest ROS level (ROS_{max}) for the different conditions are referred to as c ROS_{max} throughout Chapter 3.

The ROS_{max} values for the 3 investigated types of NPs are summarized in Figure 3.6. In the highly EGFR overexpressing MDA-MB-468 cell line, the maximum ROS generation shows a significant increase with increasing EGF multivalency in the order NP-PEG < NP-EGF₁₂ < NP-EGF₈₇. Intriguingly, the ROS_{max} values for NP-EGF₈₇ occurred at NP input concentrations ≤ 25 pM in all investigated cell lines.

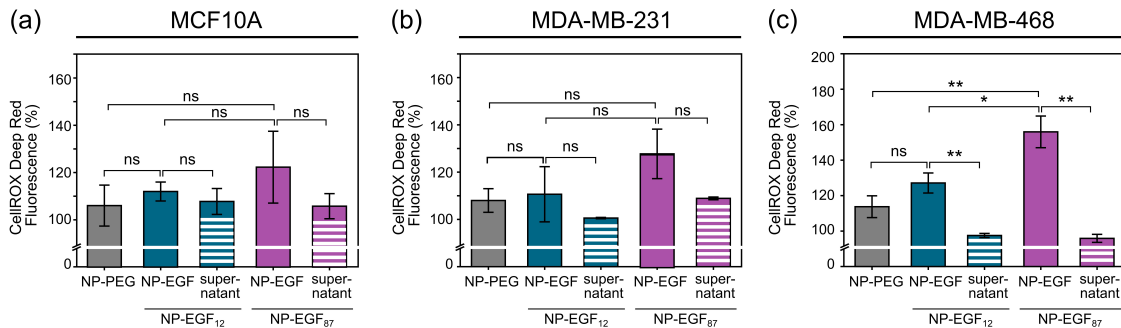


Figure 3.6: ROS_{max} values for NP-PEG, NP-EGF₁₂, NP-EGF₈₇, and supernatant from the last NP-EGF wash as detected by CellROX Deep Red fluorescence for (a) MCF10A, (b) MDA-MB-231, and, (c) MDA-MB-468. The data shown are from 3 independent experiments. All values are means and error bars are \pm s.e.m. Significance was measured using student's t -test, * $P < 0.05$, ** $P < 0.01$, ns (not significant).

After peaking at $c \text{ ROS}_{max}$, the ROS generation decreased again with increasing NP input concentration. This behavior differs from what was observed for the free EGF in Figure 3.2b, where the respondent ROS levels either continuously increase or converge. The decrease observed for the nanoconjugated EGF at increased input concentrations may be related to an adjustment of the cellular redox milieu in response to the NP-EGF-mediated ROS formation. The redox capacity of the cell is regulated by reduced glutathione (GSH) that is oxidized to its disulfide form (GSSG) by ROS. The GSH/GSSG ratio, which is an indicator of oxidative stress, was measured for MCF10A, MDA-MB-231, and MDA-MB-468 cells after a 10 min incubation with NP-EGF₈₇ in the NP input concentration range of 0 - 100 pM (Figure 3.7). For both MDA-MB-231 and MDA-MB-468, there is a decrease in the GSH/GSSG ratio at the NP input concentration corresponding to the respective $c \text{ ROS}_{max}$ values. At NP input concentrations above $c \text{ ROS}_{max}$, the GSH/GSSG ratio is increased again, indicative of the re-establishment of a more reductive cellular environment. For MCF10A, the GSH/GSSG ratios remain constant across the entire NP-EGF₈₇ concentration range.

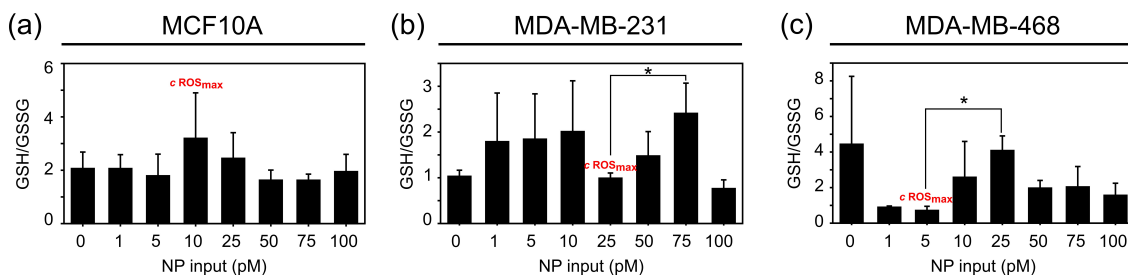


Figure 3.7: GSH/GSSG ratio after 10 min incubation with NP-EGF₈₇ in the input concentration range of 0 - 100 pM for (a) MCF10A, (b) MDA-MB-231, and (c) MDA-MB-468. The NP input concentration corresponding to $c \text{ ROS}_{max}$ is indicated on the figure. The data shown are from 3 independent experiments. All values are means and error bars are \pm s.e.m. Significance was measured compared to GSH/GSSG ratio at $c \text{ ROS}_{max}$ using student's t -test, $*P < 0.05$.

Despite higher ROS levels detected for NP-EGF₈₇ under some conditions, the NP-associated cytotoxicity was overall low unless at high NP-EGF input concentrations. In the case of MDA-MB-468, NP-EGF₈₇ concentrations above 50 pM (effective EGF concentration = 4.35 nM) resulted in significant changes in cell viability as measured by 3-(4,5-dimethylthiazol-2-yl)-2,5-diphenylterazolium bromide (MTT) assay (Figure 3.8). For MCF10A and MDA-MB-231, significant changes in cell viability were only detected at NP-EGF₈₇ concentrations ≥ 75 pM (effective EGF ≥ 6.53 nM). Overall, cytotoxicity was detected only for concentrations higher than c ROS_{max}.

In the next step, the ROS generation associated with NP-EGF₁₂ and NP-EGF₈₇ was directly compared to that of free EGF at c ROS_{max} (Figure 3.5b). For NP-EGF₁₂, there were no significant differences in the ROS levels compared to free EGF at the same effective EGF concentration for all 3 cell lines. However, in the case of NP-EGF₈₇ in the EGFR overexpressing cell lines MDA-MB-231 and MDA-MB-468, the ROS concentrations generated at c ROS_{max} were significantly higher than those of free EGF. This demonstrates that at the same effective EGF concentration, a higher EGF density on NPs results in a multivalent enhancement of ROS generation that cannot be achieved with free EGF.

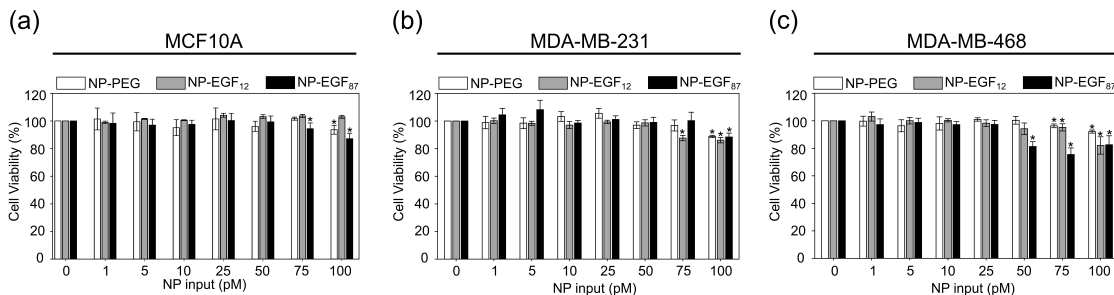


Figure 3.8: Cell viability assessed by the MTT assay after 10 min incubation with NP-PEG or NP-EGF₁₂ or NP-EGF₈₇ for (a) MCF10A, (b) MDA-MB-231, and (c) MDA-MB-468 in the NP input concentration range of 0 - 100 pM. The data shown are from 3 independent experiments. All values are means and error bars are \pm s.e.m. Significance was measured compared to the untreated cell control (0 pM) using the student's t -test, $**P < 0.05$.

To determine the source of NP-EGF mediated ROS generation, cells were pretreated with different inhibitors before addition of NP-EGF at c ROS_{max}. Pretreatment of cells with ROS scavengers (NAC, PEG-catalase), RTK inhibitor AG-1478, or NOX inhibitors (DPI and apocynin) resulted in a decrease in NP-EGF₈₇-mediated ROS generation at c ROS_{max} for all 3 cell lines (Figure 3.9).

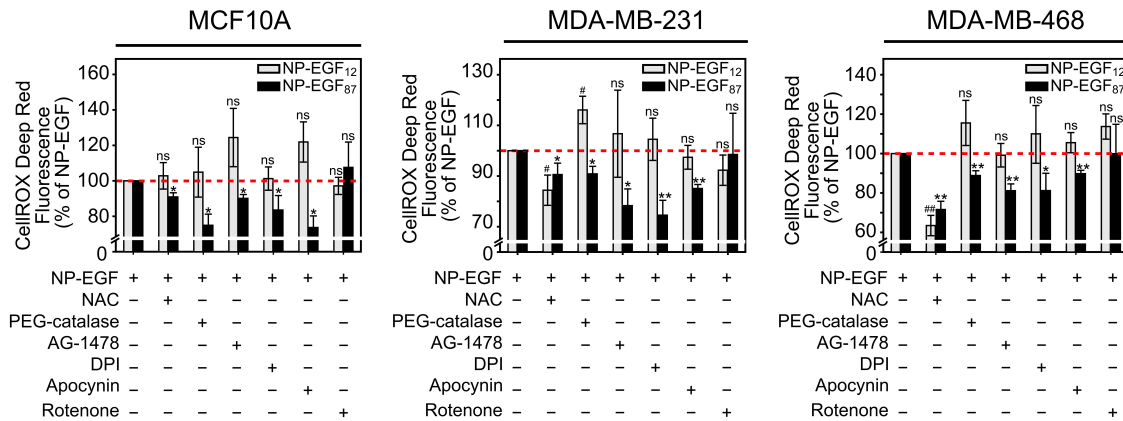


Figure 3.9: Source of NP-EGF-mediated ROS generation. CellROX Deep Red fluorescence as a measure of cytoplasmic ROS generation in cells pretreated with NAC, PEG-catalase, AG-1478, DPI, apocynin, and rotenone before stimulation with NP-EGF₁₂ or NP-EGF₈₇ at c ROS_{max} for MCF10A, MDA-MB-231, and MDA-MB-468 (from left to right). The data shown are from 3 independent experiments. All values are means, and error bars are \pm s.e.m. Significance was measured using student's t -test. # $P < 0.05$, ## $P < 0.01$, ns (not significant) when compared against NP-EGF₁₂ treatment only. * $P < 0.05$, ** $P < 0.01$, *** $P < 0.001$, ns (not significant) when compared against NP-EGF₈₇ treatment only.

In contrast, pretreatment with the mitochondrial inhibitor, rotenone did not lead to a significant decrease in ROS generated by NP-EGF₈₇ at c ROS_{max}. Overall, the inhibitor studies show that NP-EGF₈₇-induced ROS formation depends on both EGFR and NOX activation. Interestingly, even though the ROS increase induced by NP-EGF₈₇ at c ROS_{max} for MCF10A did not reach statistically significant levels in Figure 3.5, Figure 3.9 reveals that NP-EGF₈₇ triggers ROS generation that is EGFR

and NOX dependent in this case as well. In the case of NP-EGF₁₂, PEG-catalase, AG-1478, NOX inhibitors, and rotenone did not result in any reduction of ROS, consistent with a weak ROS generation associated with low EGF ligand densities. Only the GSH precursor NAC achieved a measurable reduction in ROS levels, due to a change in the global cellular redox state. The ROS levels detected after inhibitor pretreatment at c ROS_{max} for NP-EGF₁₂ were in some instances higher than the ROS detected for NP-EGF₁₂ in the absence of any inhibitors, but these increases were not significant at the 95% confidence level except for the PEG-catalase in MDA-MB-231.

The multivalent enhancement of cytoplasmic ROS generation associated with NOX activation observed for NP-EGF₈₇ can have contributions from i.) an increased binding avidity that increases the number of bound and subsequently uptaken nanoconjugated EGF relative to that of free EGF at the same input concentration, and ii.) a more potent activation provided by the multivalent NPs. To better understand the mechanisms underlying multivalent amplification, the Au content per cell for NP-EGF₁₂, NP-EGF₈₇, and NP-PEG control after 10 min of incubation with NPs in the concentration range of 0 - 150 pM was measured using microwave plasma atomic emission spectroscopy (MP-AES). Figure 3.10 shows the amount of Au associated with the cells as function of NP input concentration. For all 3 cell lines, the Au content per cell at any given input concentration increases in the order of NP-PEG < NP-EGF₁₂ < NP-EGF₈₇, confirming EGF-EGFR-mediated multivalent binding for NP-EGF that increases with EGF loading (Figure 3.10a). The differences between the NPs are more pronounced in the EGFR overexpressing cell lines and somewhat less distinct for MCF10A. Knowledge about the amount of gold associated with the cells, facilitates an analysis of the ROS levels as function of the number of NPs associated with the cells (Figure 3.10b). The plots in Figure 3.10b show that the ROS levels for NP-EGF₈₇ in MDA-MB-231 and MDA-MB-468 lie systematically above those of

NP-EGF₁₂ and NP-PEG at comparable cellular NP concentrations. Higher ROS levels for NP-EGF₈₇ than for NP-EGF₁₂ at the same NP concentration provide evidence for an additional amplification mechanism of ROS generation that complements a multivalent increase in binding and uptake.

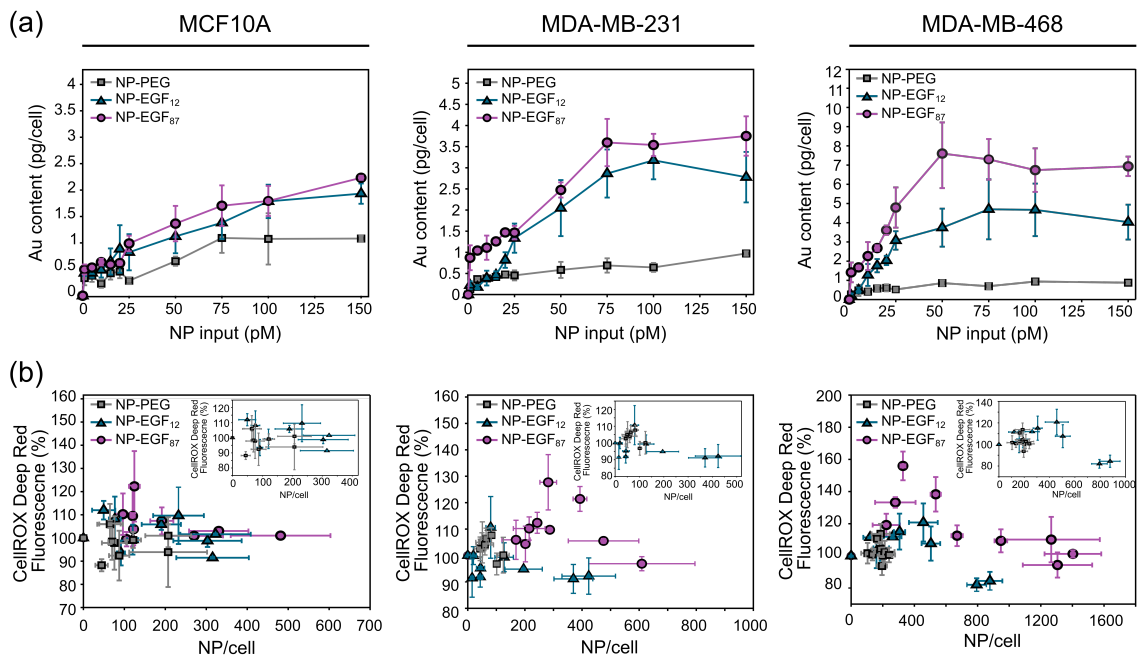


Figure 3.10: Multivalent enhancement of NP-EGF mediated ROS generation as measured by cellular uptake. (a) Au content per cell as a function of NP input concentration for NP-PEG (gray squares), NP-EGF₁₂ (blue triangles), and NP-EGF₈₇ (purple circles) for MCF10A, MDA-MB-231, and MDA-MB-468 (from left to right) (b) Cytoplasmic ROS as measured by CellROX Deep Red as function of NP delivered per cell for NP-PEG (gray squares), NP-EGF₁₂ (blue triangles), and NP-EGF₈₇ (purple circles) for MCF10A, MDA-MB-231, and MDA-MB-468 (from left to right). Inset shows cytoplasmic ROS as a function of NP delivered per cell for NP-PEG and NP-EGF₁₂. The data shown are from 3 independent experiments. All values are means, and error bars are \pm s.e.m.

We attribute the observed higher ROS levels for NP-EGF₈₇ than for NP-EGF₁₂ at identical cell-associated NP concentrations to the spatial clustering of EGFR^{46,84}. High local concentrations of receptors facilitate multiple EGF per NPs to bind to spatially co-localized EGFR receptors. NP-EGF₈₇ are expected to bind and activate

more EGFR within the NP footprint than NP-EGF₁₂, and this stronger activation can account for a higher EGFR-dependent ROS generation for NP-EGF with higher ligand density. Together, Figure 3.5 and Figure 3.10 indicate that a high EGF density on the NPs leads to a multivalent amplification of both the average number of NPs associated with a cell for any given NP input and the EGF-EGFR binding mediated ROS generation per particle.

3.4 NP-EGF-induced ROS generation and EGFR phosphorylation

The global EGFR tyrosine 1068 (Y1068) phosphorylation levels induced by NP-EGF₁₂ and NP-EGF₈₇ in the NP input concentration range of 0 - 100 pM (Figure 3.11a) shows that for all cell lines, the maximum phosphorylation level was dependent on the multivalency of the NPs, with NP-EGF₈₇ generating higher levels of Y1068 phosphorylation than NP-EGF₁₂. The difference in Y1068 phosphorylation between NP-EGF₁₂ and NP-EGF₈₇ was most pronounced for the EGFR overexpressing MDA-MB-468 cell line. Next, Y1068 phosphorylation at c ROS_{max} obtained for NP-PEG, NP-EGF₁₂, and NP-EGF₈₇ were compared to each other and to free EGF at the same effective concentration as for the NP-EGF using western blotting (Figure 3.11b). In Figure 3.11c, the intensity of phosphorylated EGFR (pEGFR) measured at Y1068 was normalized by the intensity of total EGFR protein. For all 3 cell lines, densitometric analysis revealed that the ratio of pEGFR/EGFR was significantly higher after treatment with NP-EGF₈₇ than for the non-treated cell control and free EGF. In contrast, NP-EGF₁₂ did not yield a significant increase over the non-treated cell control. The gain in phosphorylation for NP-EGF₈₇ compared with NP-EGF₁₂ and free EGF confirms a multivalent enhancement of EGFR activation. The multivalent enhancement of EGFR activation through NP-EGF indicated in Figure 3.11 is con-

sistent with the findings of previous study into EGFR activation through NP-EGF.⁸⁴ The prior work analyzed the effect of multivalency on EGFR activation primarily in the context of direct EGF-EGFR binding mediated receptor phosphorylation, without evaluating a potential contribution of EGF-induced ROS.

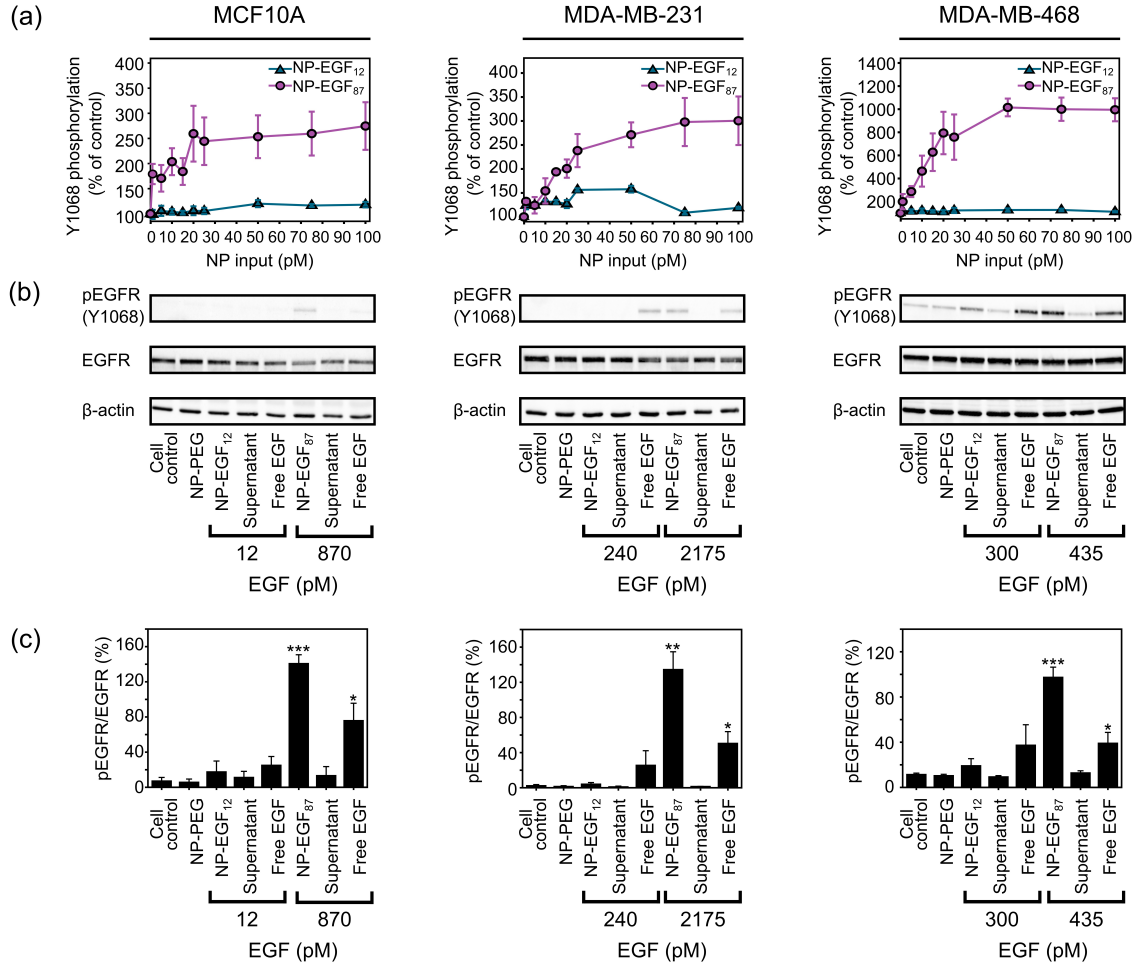


Figure 3.11: Multivalent enhancement of NP-EGF-mediated EGFR phosphorylation. (a) NP-EGF₁₂ and NP-EGF₈₇-induced Y1068 phosphorylation as quantified by flow cytometry in the NP input concentration of 0 - 100 pM. (b) Western blots for Y1068 and EGFR after a 10 min incubation of NP-EGF₁₂, NP-EGF₈₇, free EGF at the same effective EGF concentration (at *c* ROS_{max}) and supernatant of last NP-EGF wash. β -actin was included a loading control. (c) Densitometric quantification of pEGFR relative to total EGFR for the indicated conditions. All values are means, and error bars are \pm s.e.m. Significance was compared to the non-treated cell control using student's *t*-test, **P* < 0.05, ***P* < 0.01, ****P* < 0.001.

To address this potential additional mechanism, the contribution of EGF-induced ROS on the multivalent enhancement of Y1068 phosphorylation by NP-EGF₈₇ at *c* ROS_{max} was quantified using ROS-specific inhibitors, RTK inhibitor AG-1478, NOX inhibitors (DPI and apocynin), as well as the mitochondrial inhibitor rotenone (Figure 3.12).

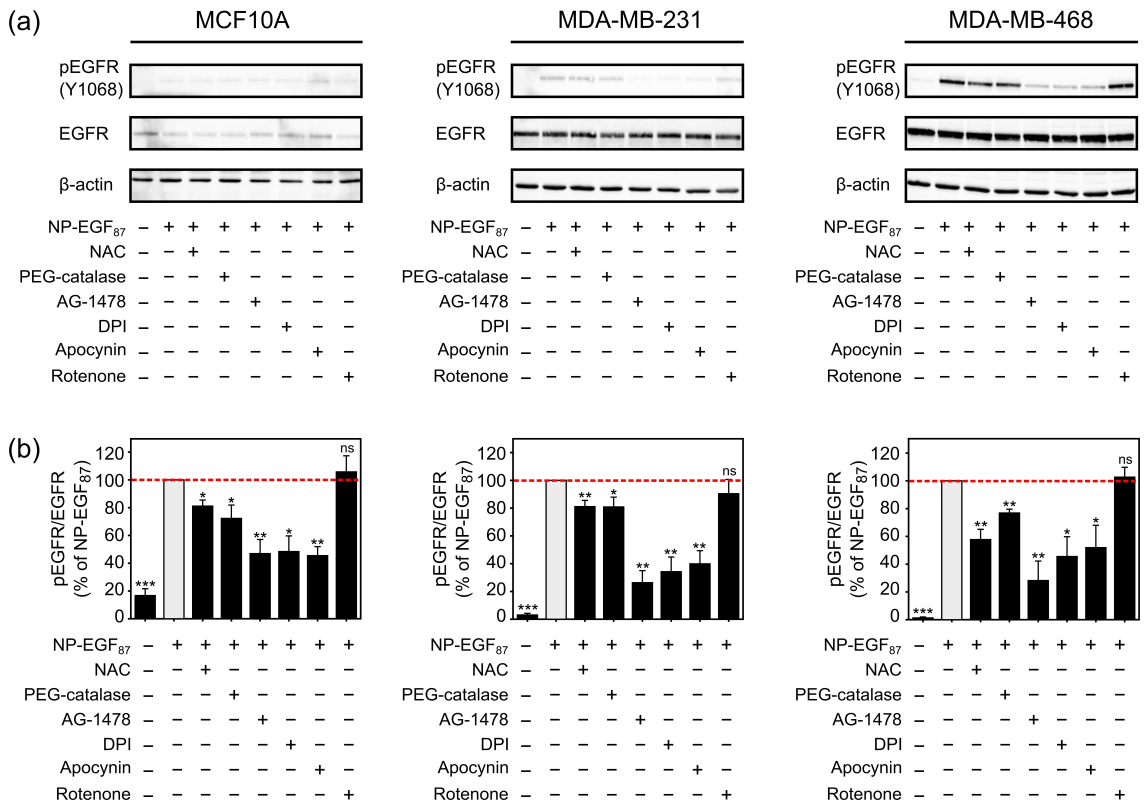


Figure 3.12: NP-EGF-mediated EGFR activation is modulated by cellular ROS levels and NOX activity. (a) Western blots for Y1068 and EGFR. Cells were pretreated with NAC, PEG-catalase, AG-1478, DPI, apocynin, and rotenone where specified, prior to NP-EGF₈₇ stimulation (at *c* ROS_{max}). β-actin was included a loading control. (b) Densitometric quantification of pEGFR relative to total EGFR for the indicated conditions. All values are means, and error bars are ± s.e.m. Significance was compared to NP-EGF₈₇ treatment only (at *c* ROS_{max}) using student's *t*-test, **P* < 0.05, ***P* < 0.01, ****P* < 0.001, ns (not significant).

The densitometric analysis of the pEGFR/EGFR ratio in Figure 3.12b revealed that

in all 3 cell lines, pretreatment with NAC, PEG-catalase, and NOX inhibitors, as well as with AG-1478 resulted in a decrease in Y1068 phosphorylation, whereas the mitochondrial inhibitor had no effect. The inhibition pattern revealed by the densitometric analysis of the western blots in Figure 3.12b provide evidence that EGFR phosphorylation at c ROS_{max} after NP-EGF₈₇ treatment is modulated by cellular ROS levels and NOX activity. This finding directly relates the multivalent enhancement of ROS generation through NP-EGF₈₇ with a gain in EGFR activation and suggests that NP-EGF₈₇-induced ROS generation provides a measurable contribution to the receptor activation obtained at c ROS_{max}. Overall, the data confirm that multivalent NP-EGF binding induces ROS generation which can in turn enhance EGFR-mediated signaling.

3.5 Conclusion

The studies shown in this chapter investigated the effect of multivalency on EGF-induced ROS generation and its contribution to EGFR activation using NP-EGF with an 81 ± 1 nm diameter Au NP core and EGF densities of 12 ± 7 EGF/NP (NP-EGF₁₂) and 87 ± 6 EGF/NP (NP-EGF₈₇) in three breast cancer cell models (MCF10A, MDA-MB-231, MDA-MB-468). NP-EGF with input concentrations of c ROS_{max} ≤ 25 pM (≤ 2175 pM EGF) induced a significant increase in cellular ROS levels in the EGFR-overexpressing cell lines MDA-MB-231 and MDA-MB-468. Importantly, this ROS generation was both EGFR- and NOX-dependent. NP-EGF₈₇ achieved stronger EGF-dependent ROS generation than free EGF or NP-EGF₁₂. The multivalent enhancement of ROS generation observed for NP-EGF₈₇ was driven by an increase in NP-EGF binding as well as a higher density of EGF-EGFR binding interactions within the footprint of the individual NPs. Importantly, the NP-EGF-induced gain in ROS for NP-EGF₈₇ was correlated with a measurable increase in

EGFR phosphorylation, confirming that EGF-induced ROS formation contributes to the multivalent enhancement of EGFR activation through NP-EGF. More generally, our findings support a feedback mechanism in which NOX enhance EGFR activation through the ROS generated in response to EGF binding to EGFR.

3.6 Materials and Methods

Cell culture. MCF10A, MDA-MB-231, and MDA-MB-468 breast epithelial cell lines were obtained from American Type Culture Collection (Manassas, VA, USA). MCF10A cells were maintained in DMEM/F12 (Invitrogen) supplemented with 5% horse serum (Invitrogen), 0.5 mg/mL hydrocortisone (Sigma-Aldrich), 20 ng/mL human EGF (Invitrogen), 10 $\mu\text{g}/\text{mL}$ insulin (Sigma-Aldrich), 100 ng/mL cholera toxin (Sigma-Aldrich), 100 units/mL penicillin and 100 $\mu\text{g}/\text{mL}$ streptomycin (Invitrogen). MDA-MB-231 and MDA-MB-468 were maintained in DMEM supplemented with 10% fetal bovine serum (Invitrogen), 100 units/mL penicillin and 100 $\mu\text{g}/\text{mL}$ streptomycin (Invitrogen). All cells were maintained at 37 °C in a humidified atmosphere containing 5% CO₂. For experiments, cells were plated (0.15×10^6 cells/mL) in 12-well plates overnight and then serum starved for 18 h prior to experiments.

Inhibitor Treatments. Unless otherwise specified, all inhibitors were purchased from Sigma-Aldrich. The inhibitors were first dissolved in the specified solvents and then freshly diluted in serum free media prior to experiments. NAC (250 mM in $1 \times$ PBS) was used at a final concentration of 5 mM. PEG-catalase (40,000 U/mL in diH₂O) was used at a final concentration of 500 U/mL. Tyrphostin AG-1478 (1 μM in DMSO) was used at a final concentration of 250 nM. DPI (0.02 M in DMSO) was used at a final concentration of 20 μM . Apocynin (0.05 M in DMSO) was used at a final concentration of 20 μM . Rotenone (0.1 M in DMSO) was used a final concentration of 10 μM . For inhibitors dissolved in DMSO, the final % v/v of DMSO in serum free

media did not exceed 0.1% . Where specified, cells were pretreated with inhibitors for 30 mins first and then during the last 10 mins, free EGF or NP-EGF was added.

NP-EGF preparation. EGF recombinant human protein (1 mg/mL in $1\times$ PBS, pH 7.4) (Thermo Fisher Scientific) was functionalized by adding 2 μ L of propargyl-N-hydroxysuccinimidyl (NHS)) ester (Peptides International) solution (100 mg/mL in anhydrous DMSO) and incubated on ice for 6 h at 4 $^{\circ}$ C. The alkyne-functionalized EGF was then dialyzed in $1\times$ PBS using D-tube Dialyzer Midi (EMD Millipore) with a molecular weight cut-off of 3.5 kDa for at least 24 h to remove excess NHS ester. The alkyne-functionalized EGF was then stored at -20 $^{\circ}$ C until further use. To functionalize Au NPs, two thiol polyethylene glycol (PEG) molecules were used. PEG 1 (HS-CH₂CH₂-(C₂H₄O)₇₇-N₃) (Nanocs Inc.) and PEG 2 (HS-(CH₂)₁₁-(C₂H₄O)₆) (ProChimia Surfaces) were added to 24 mL of 80 nm Au NP colloidal solution (synthesized via Turkevich method¹⁸¹) to give a final concentration of 50 μ M for PEG 1 and 5 μ M for PEG 2. This mixture was incubated for 17 h at room temperature on a shaker. Following the incubation period, the pegylated Au NPs were centrifuged three times (2.4 krpm, 10 min) and washed with diH₂O. After the last centrifugation cycle, 10 μ L of the NP pellet was resuspended to 770 μ L $0.1\times$ PBS. Then, 5 μ L of alkyne-functionalized EGF was added to this mixture. To catalyze the click reaction, 8 μ L of catalyst solution was added. The catalyst solution was prepared by mixing (1:1, v/v) ascorbic acid (17.6 mg/mL in diH₂O) and CuSO₄ \cdot 5H₂O (5 mg/mL in diH₂O). The solution containing NPs, alkyne-functionalized EGF and catalyst was incubated overnight at 4 $^{\circ}$ C to make NP-EGF₈₇. To prepare NP-EGF₁₂, the procedural steps were identical to NP-EGF₈₇, except, 0.1 μ L of alkyne-functionalized EGF and 1 μ L of catalyst solution was used and incubated at 4 $^{\circ}$ C for 1.5 h only. After the indicated incubation period, NP-EGF were cleaned three times by centrifugation (2.4krpm, 10 min) and after the last centrifugation cycle, the NP-EGF pellet was

resuspended with $0.1\times$ PBS.

NP characterization. To determine the number of EGF per NP, a Human EGF ELISA kit (Thermo Fisher Scientific) was used following the protocol provided by the manufacturer using 1 pM of NP (NP-PEG, NP-EGF). For SEM sample preparation, a 30 μ L sample of NPs diluted in diH₂O was added to a 0.5×0.5 cm² silicon wafer and evaporated overnight. SEM imaging was performed on a Zeiss Supra 55VP at 5.00 kV and a working distance of 7.0 mm. UV-Vis spectra were obtained on an Agilent Cary 5000 and diH₂O was used for baseline correction. The hydrodynamic diameters and zeta potentials of NPs were measured using a Malvern Zetasizer Nano ZS90. Deionized water was used to dilute the NPs for hydrodynamic diameter measurements. To measure the zeta potential, the NPs were diluted in 10 mM NaCl solution.

Cytoplasmic ROS detection. Cells were plated as described above. To detect cytoplasmic ROS, cells were incubated with 1 μ M CellROX Deep Red Reagent (Invitrogen) in phenol red free medium for 30 mins at 37 °C. For cell experiments, NPs (NP-PEG, NP-EGF₁₂, NP-EGF₈₇) were added during the last 10 mins of CellROX Deep Red incubation. Then, cells were rinsed 3 times with PBS and harvested. The cell suspension was then centrifuged for 5 mins to obtain a cell pellet. Subsequently, the cells were fixed with 4% paraformaldehyde for 10 mins at room temperature. After fixation, cells were centrifuged and the cell pellet was resuspended in 500 μ L PBS for flow cytometry. Flow cytometry acquisition was performed on a BD FACSCalibur (BD Biosciences) and analysis was done using Flowing software 2.

Relative EGFR expression level using flow cytometry. Cells were plated as described above. The cell culture media was removed and cells were detached with 500 μ L enzyme free cell dissociation solution (EMDMillipore) for 5 mins at 37 °C for MDA-MB-231 and MDA-MB-468. For MCF10A, a cellstripper solution (Corning) was used to detach the cells for 20 - 30 mins at 37 °C. Cells were subsequently

quenched with 500 μ L resuspension media and collected by centrifugation. The cells were fixed with 4% paraformaldehyde solution at room temperature for 10 mins and then centrifuged once. The supernatant was removed and 500 μ l of Anti-EGFR Affibody FITC (abcam, ab81872) in 2% BSA solution was incubated with the cell pellet for 1 h at room temperature. After that, the cells were centrifuged three times and washed with 2% BSA solution. At the end of the last centrifugation cycle, the supernatant was removed, and the cells were resuspended in 500 μ L of PBS for flow cytometry. Flow cytometry acquisition was performed on a BD FACSCalibur (BD Biosciences) and analysis was done using Flowing software 2.

Quantification of EGFR phosphorylation using flow cytometry. Cells were plated as described above. The cells were washed once with $1\times$ PBS and then incubated with NP-EGF at the indicated concentrations for 10 mins in serum free media. The NP solution was removed, and cells were rinsed several times with $1\times$ PBS. Cells were then harvested and collected by centrifugation. The cells were fixed with 4% paraformaldehyde solution at room temperature for 10 mins and then centrifuged. Cells were then permeabilized with 0.1% Triton X-100 for 10 mins at room temperature and centrifuged. Next, the supernatant was removed and 50 μ L of phosphor-EGF Receptor (Tyr1068) rabbit monoclonal antibody (PE conjugate) (Cell Signaling Technology, 1:75) was incubated with the cell pellet for 1 h at room temperature. After an incubation period of 1 h, the cells were centrifuged three times and washed with 2% BSA solution. At the end of the last centrifugation cycle, the supernatant was removed, and the cells were resuspended in 500 μ L of PBS for flow cytometry. Flow cytometry acquisition was performed on a BD FACSCalibur (BD Biosciences) and analysis was done using Flowing software 2.

Quantification of GSH/GSSG. The cellular GSH/GSSG was measured using the GSH/GSSG ratio detection assay kit II (Fluorometric green) following the manufac-

turer's protocol (Abcam, ab205811). Cells were plated as described above. After incubating NP-EGF with cells for 10 mins at the indicated concentration, cells were rinsed briefly with PBS. Then, cells were detached and centrifuged twice and washed with ice cold $1\times$ PBS. Ice cold $1\times$ Mammalian Lysis Buffer (Abcam, ab179835) was then added to the cell pellet to prepare the cell lysates. Lysates were deproteinized using the TCA deproteinizing sample preparation kit (Abcam, ab204708) following the manufacturer's protocol. After deproteinization, the samples were ready to use. After a 30 min incubation of lysates with the appropriate assay mixture in the dark, fluorescence (Excitation/Emission = 490/520) was measured using a fluorescence microplate reader (Spectramax M5).

Quantification of Au NP cellular uptake. Cells were plated as described above. The cells were rinsed once with $1\times$ PBS and then incubated with NPs (NP-PEG, NP-EGF) for 10 mins in serum free media. After an incubation period of 10 mins, the NP solution was removed, and the cells were rinsed 3 times with PBS before harvesting. Cells were then pelleted by centrifugation and $30\ \mu\text{L}$ of $1\times$ PBS was added to the cell pellet. Aqua regia ($600\ \mu\text{L}$) was added to the $30\ \mu\text{L}$ cell solution to dissolve the Au NPs. The mixture was then dried at $65\ ^\circ\text{C}$ for several hours and then re-dissolved in HCl solution (2%, v/v). The Au content in the cell samples was quantified using MP-AES (4200 MP-AES, Agilent).

Western Blot. Cells were plated as described above. Cells were treated as indicated and then harvested and washed once with ice cold $1\times$ PBS. The samples were then boiled in $1\times$ Laemmli sample buffer (BioRad) at $95\ ^\circ\text{C}$ for 5 mins. The protein samples were then separated by SDS-PAGE using a 10% polyacrylamide gel which ran for 2 h at 120 V. The gel was then transferred to a nitrocellulose membrane (BioRad) for 1.5 h at 400 mA. After protein transfer, the membrane was incubated with Ponceau S (Sigma-Aldrich) staining solution to confirm proteins were transferred. The

membrane was then rinsed a few times with 1× Tris-Buffered Saline, 0.1% Tween 20 Detergent (TBST). Then, the membrane was cut (upper part for Y1068 and EGFR, lower part for β -actin) and subsequently blocked in 5% (w/v) non-fat dry milk powder in 1× TBST with gentle rocking for 1 h at room temperature. The membrane was washed several times with 1× TBST (5 min each) and then immunoblotting was performed with the following primary antibodies overnight with gentle rocking at 4 °C at the indicated dilutions in 1× TBST: Y1068 (Cell Signaling Technology, #2234, 1:1000) and β -actin (Cell Signaling Technology, #4967, 1:1000). After the overnight incubation, the membranes were washed several times with 1×TBST (5 min each) and incubated with Amersham ECL peroxidase-conjugated secondary antibody (Sigma-Aldrich, 1:8000 in 1× TBST) for 1 h at room temperature. The nitrocellulose membrane was then developed by a chemiluminescent substrate (SuperSignal™ West Pico PLUS Chemiluminescent Substrate, Thermo Fisher Scientific) and then imaged using the ChemiDoc Imaging System (BioRad). Then, the upper part of the full membrane that was immunoblotted for Y1068 was stripped (Restore Western Blot Stripping Buffer, Thermo Fisher Scientific) for 25 mins at 37 °C before reprobing for total EGFR (Cell Signaling Technology, #2232, 1:1000). The intensity of the bands was quantified using ImageJ.

Cell viability. The MTT (Sigma-Aldrich) assay was used to determine cell viability. Cells were incubated with NPs (NP-PEG, NP-EGF₁₂, NP-EGF₈₇) at 37 °C for 10 mins in serum free media and then rinsed a few times with 1× PBS. Afterwards, cells were incubated with 0.5 mg/mL MTT reagent in serum free media for 1 h at 37 °C. Purple colored formazan crystals were formed by the living cells following the reduction of MTT by mitochondrial dehydrogenases. The MTT reagent was then removed from the wells and the crystals were dissolved in a 1:1 solution of DMSO:ethanol. The optical density (OD) at 570 nm was determined using a spectrophotometric

microplate reader (Spectramax M5). The OD of the non-treated cells (control) was considered equivalent to 100% viable cells and the cell viability (%) of NP-treated cells was calculated from the respective OD values.

Statistical analysis. Unless otherwise noted, all experiments were performed independently in triplicates and data were expressed as means \pm s.e.m. Statistical analysis was performed using student's *t*-test. Values of $*P < 0.05$, $**P < 0.01$ and $***P < 0.001$ were considered statistically significant.

Chapter 4

Future Directions

In summary, Chapter 2 and 3 demonstrates the versatility of Au NPs as nanoprobe in investigating large-scale receptor clustering and second messenger mediated activation. Chapter 2 details the characterization of spatial receptor heterogeneity using Au NP labels through hyperspectral PCM imaging. The design of Au NPs can also be tuned to probe multivalent ligand-receptor interactions, more specifically, the role of NP-EGF multivalency in ROS-mediated EGFR activation. Following the work presented herein in this dissertation, subsequent studies will focus on testing the role of spatial EGFR clustering in specifying the mode of action of ROS. Furthermore, future studies will also elucidate the role of proximity effects in ROS-mediated EGFR signaling enhancement. Previous studies^{42,84,102} indicated lateral propagation of EGFR activation in receptor clusters. However, it remains unclear whether ROS generation after EGF ligand binding also contributes to lateral propagation mechanisms. The enhancement in EGFR activation observed in locations of NP-EGF clustering can be due to an increase in EGF-EGFR binding contacts or can have a contribution from lateral signal propagation mediated by the formation of local H₂O₂.

Given the short lifetime of ROS second messenger molecules, it is likely that H₂O₂ is the predominant ROS generated and probes that can detect H₂O₂ specifically are needed. The fluorescent dye, CellROX Deep Red, used in Chapter 3 is not specific to any ROS. Future work will incorporate a H₂O₂ selective probe such as the commer-

cially available H_2O_2 biosensor, HyPer^{182,183}. HyPer probes are genetically encoded fluorescent indicators used for ratiometric detection of intracellular H_2O_2 on the sub-nanomolar to low nanomolar range. HyPer probes allow for detecting H_2O_2 gradients (Figure 4.1).

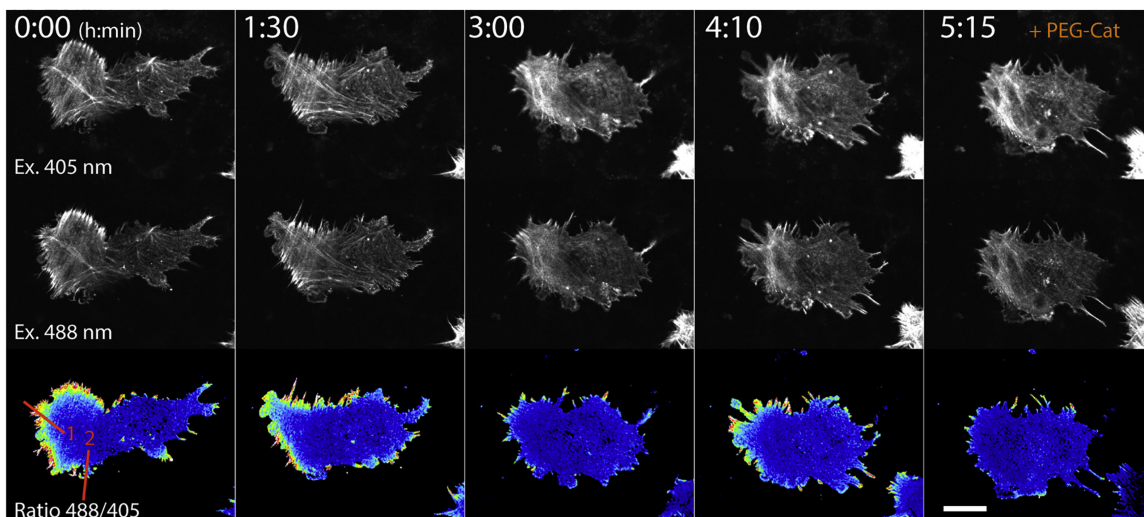


Figure 4.1: Detection of H_2O_2 gradients using HyPer probe. Images of a migrating cell at different time points. Upper and middle rows: fluorescent images excited by 405 and 488 nm. Lower row: ratiometric images of the fluorescence intensity at 488 and 405 nm. Addition of PEG-catalase reduces the gradient. Scale bar: 10 μm . Reprinted with permission from reference¹⁸³, © 2020 Elsevier.

The signal of HyPer probes can be mapped using fluorescence microscopy. At the same time, incorporation of a fluorescent dye to Au NPs allows the NPs to be mapped using fluorescence microscopy as well. The comparison of the local H_2O_2 signal for a given EGF ligand density on the NP provides information about the NP-EGF clustering levels and insights into whether NP-EGF clustering in receptor clusters is involved in enhancing H_2O_2 generation. The optical colocalization of NP-EGF clustering with H_2O_2 formation and EGFR phosphorylation will address the question of whether EGFR clusters enhance H_2O_2 generation and if this amplification in turn also increases EGFR phosphorylation. Chapter 3 provided some insights in

to ROS-mediated EGFR activation using multivalent Au NPs, but the proposed future work involves understanding the role of spatial EGFR clustering (Chapter 2) in ROS-mediated EGFR activation which is currently not well understood. A better quantitative understanding about H₂O₂-mediated EGFR activation is important because, unlike in the case of EGFR phosphorylation through EGF ligand, H₂O₂ does not induce dimerization of EGFR. Redox signaling may represent a feasible drug target in overcoming drug resistance in cancer therapies.

Appendix A

Data Organization and Storage

The data presented in this dissertation can be found on the Boston University Research Drive in the folder for Sandy Zhang in the Reinhard lab:

(U:\eng_research_reinhard.Sandy Zhang)

Below is a short introduction to the files in that folder. If you have any questions, I can be contacted through email at szhang16@bu.edu.

Folder: Dissertation

This folder contains the final thesis version in PDF, figure files, and the final presentation.

Folder: G2 Oral Exam

This folder contains my G2 oral exam presentation as well as written prospectus.

Folder: Order Forms

This folder contains the order forms for materials ordered for both projects.

Folder: Other

This folder contains conference material (poster + presentation) and SEM training videos).

Folder: Paper 1

In this folder I have all the raw data and files associated with Chapter 2 in this disser-

tation. The subfolder labeled as "Data" is separated by different categories (confocal microscopy, darkfield images, SEM, hyperspectral data, and dSTORM data). The manuscript folder has all the drafts and final figures used in the paper corresponding to Chapter 2. The folder labeled as MATLAB codes contains the codes used for analyzing data and for generating figures.

Folder: Paper 2

In this folder I have all the raw data files associated with Chapter 3 in this dissertation. They are separated into different categories based on the technique or different instruments used (flow cytometry, MP-AES, ELISA, DLS, SEM, western blot). The manuscript folder contains all the draft versions and the figures. This folder also contains the presentations (group meetings, DAC meetings, etc.).

Folder: Review article

In this folder there are drafts and figures for the review article titled "Properties, Fabrication, Characterization, and Applications of Lipid-coated Plasmonic Nanoparticles: A Review". This folder contains the drafts, figures, and articles related to the different sections of the review article.

References

- [1] Pinkas Kramarski R; Soussan L; Waterman H; Levkowitz G; Alroy I; Klapper L; Lavi S; Seger R; Ratzkin B J; Sela M; and Yarden Y. Diversification of Neu differentiation factor and epidermal growth factor signaling by combinatorial receptor interactions. *EMBO Journal*, **1996**, 15(10), 2452–2467.
- [2] Riese D J; van Raaij T M; Plowman G D; Andrews G C; and Stern D F. The cellular response to neuregulins is governed by complex interactions of the erbB receptor family. *Molecular and Cellular Biology*, **1995**, 15(10), 5770–5776.
- [3] Carpenter G; Lembach K J; Morrison M M; and Cohen S. Characterization of the binding of ¹²⁵I labeled epidermal growth factor to human fibroblasts. *Journal of Biological Chemistry*, **1975**, 250(11), 4297–4304.
- [4] Todaro G J; De Larco J E; and Cohen S. Transformation by murine and feline sarcoma viruses specifically blocks binding of epidermal growth factor to cells. *Nature*, **1976**, 264(5581), 26–31.
- [5] Ullrich A; Coussens L; Hayflick J S; Dull T J; Gray A; Tam A W; Lee J; Yarden Y; Libermann T A; Schlessinger J; Downward J; Mayes E L; Whittle N; Waterfield M D; and Seeburg P H. Human epidermal growth factor receptor cDNA sequence and aberrant expression of the amplified gene in A431 epidermoid carcinoma cells. *Nature*, **1984**, 309(5967), 418–425.
- [6] Roskoski J, R. The ErbB/HER family of protein-tyrosine kinases and cancer. *Pharmacol Res*, **2014**, 79, 34–74.
- [7] Mok T S. Personalized medicine in lung cancer: What we need to know. *Nature Reviews Clinical Oncology*, **2011**, 8(11), 661–668.
- [8] Wee P and Wang Z. Epidermal growth factor receptor cell proliferation signaling pathways, **2017**. ISSN 20726694.
- [9] Arteaga C L; Sliwkowski M X; Osborne C K; Perez E A; Puglisi F; and Gianni L. Treatment of HER2-positive breast cancer: Current status and future perspectives. *Nature Reviews Clinical Oncology*, **2012**, 9(1), 16–32.
- [10] Harari D and Yarden Y. Molecular mechanisms underlying ErbB2/HER2 action in breast cancer. *Oncogene*, **2000**, 19(53), 6102–6114.

- [11] Seshacharyulu P; Ponnusamy M P; Haridas D; Jain M; Ganti A K; and Batra S K. Targeting the EGFR signaling pathway in cancer therapy. *Expert Opinion on Therapeutic Targets*, **2012**, 16(1), 15–31.
- [12] Arteaga C L and Engelman J A. ERBB receptors: From oncogene discovery to basic science to mechanism-based cancer therapeutics. *Cancer Cell*, **2014**, 25(3), 282–303.
- [13] Wheeler D L; Dunn E F; and Harari P M. Understanding resistance to EGFR inhibitors-impact on future treatment strategies. *Nature Reviews Clinical Oncology*, **2010**, 7(9), 493–507.
- [14] Wang Y; Gao J; Guo X; Tong T; Shi X; Li L; Qi M; Wang Y; Cai M; Jiang J; Xu C; Ji H; and Wang H. Regulation of EGFR nanocluster formation by ionic protein-lipid interaction. *Cell Research*, **2014**, 24(8), 959–976.
- [15] Needham S R; Roberts S K; Arkhipov A; Mysore V P; Tynan C J; Zanetti Domingues L C; Kim E T; Losasso V; Korovesis D; Hirsch M; Rolfe D J; Clarke D T; Winn M D; Lajevardipour A; Clayton A H; Pike L J; Perani M; Parker P J; Shan Y; Shaw D E; and Martin Fernandez M L. EGFR oligomerization organizes kinase-active dimers into competent signalling platforms. *Nature Communications*, **2016**, 7.
- [16] Yosef Yarden and Mark X. Sliwkowski. UNTANGLING THE ErbB SIGNALING NETWORK. *Nature Reviews — Molecular Cell Biology*, **2001**, 2(2), 127.
- [17] Ogiso H; Ishitani R; Nureki O; Fukai S; Yamanaka M; Kim J H; Saito K; Sakamoto A; Inoue M; Shirouzu M; and Yokoyama S. Crystal structure of the complex of human epidermal growth factor and receptor extracellular domains. *Cell*, **2002**, 110(6), 775–787.
- [18] Cochet C; Kashles O; Chambaz E M; Borrello I; King C R; and Schlessinger J. Demonstration of epidermal growth factor-induced receptor dimerization in living cells using a chemical covalent cross-linking agent. *Journal of Biological Chemistry*, **1988**, 263(7), 3290–3295.
- [19] Garrett T P; McKern N M; Lou M; Elleman T C; Adams T E; Lovrecz G O; Zhu H J; Walker F; Frenkel M J; Hoyne P A; Jorissen R N; Nice E C; Burgess A W; and Ward C W. Crystal structure of a truncated epidermal growth factor receptor extracellular domain bound to transforming growth factor α . *Cell*, **2002**, 110(6), 763–773.
- [20] Lemmon M A; Bu Z; Ladbury J E; Zhou M; Pinchasi D; Lax I; Engelman D M; and Schlessinger J. Two EGF molecules contribute additively to stabilization of the EGFR dimer. *EMBO Journal*, **1997**, 16(2), 281–294.

- [21] Yarden Y and Schlessinger J. Self-Phosphorylation of Epidermal Growth Factor Receptor: Evidence for a Model of Intermolecular Allosteric Activation. *Biochemistry*, **1987**, 26(5), 1434–1442.
- [22] Schlessinger J. Ligand-induced, receptor-mediated dimerization and activation of EGF receptor. *Cell*, **2002**, 110(6), 669–672.
- [23] Huang Y; Bharill S; Karandur D; Peterson S M; Marita M; Shi X; Kaliszewski M J; Smith A W; Isacoff E Y; and Kuriyan J. Molecular basis for multimerization in the activation of the epidermal growth factor receptor. *eLife*, **2016**, 5.
- [24] Zhang X; Gureasko J; Shen K; Cole P A; and Kuriyan J. An Allosteric Mechanism for Activation of the Kinase Domain of Epidermal Growth Factor Receptor. *Cell*, **2006**, 125(6), 1137–1149.
- [25] Dawson J P; Berger M B; Lin C C; Schlessinger J; Lemmon M A; and Ferguson K M. Epidermal Growth Factor Receptor Dimerization and Activation Require Ligand-Induced Conformational Changes in the Dimer Interface. *Molecular and Cellular Biology*, **2005**, 25(17), 7734–7742.
- [26] Maruyama I. Mechanisms of Activation of Receptor Tyrosine Kinases: Monomers or Dimers. *Cells*, **2014**, 3(2), 304–330.
- [27] Maruyama I N. Activation of transmembrane cell-surface receptors via a common mechanism? The "rotation model". *BioEssays*, **2015**, 37(9), 959–967.
- [28] Hofman E G; Bader A N; Voortman J; Van Den Heuvel D J; Sigismund S; Verkleij A J; Gerritsen H C; and Van Bergen en Henegouwen P M. Ligand-induced EGF receptor oligomerization is kinase-dependent and enhances internalization. *Journal of Biological Chemistry*, **2010**, 285(50), 39481–39489.
- [29] van Belzen N; Rijken P J; Hage W J; de Laat S W; Verkleij A J; and Boonstra J. Direct visualization and quantitative analysis of epidermal growth factor-induced receptor clustering. *Journal of Cellular Physiology*, **1988**, 134(3), 413–420.
- [30] Moriki T; Maruyama H; and Maruyama I N. Activation of preformed EGF receptor dimers by ligand-induced rotation of the transmembrane domain. *Journal of Molecular Biology*, **2001**, 311(5), 1011–1026.
- [31] Sako Y; Minoghchi S; and Yanagida T. Single-molecule imaging of EGFR signalling on the surface of living cells. *Nature Cell Biology*, **2000**, 2(3), 168–172.
- [32] Kozer N; Barua D; Orchard S; Nice E C; Burgess A W; Hlavacek W S; and Clayton A H. Exploring higher-order EGFR oligomerisation and phosphorylation - A combined experimental and theoretical approach. *Molecular BioSystems*, **2013**, 9(7), 1849–1863.

- [33] Abulrob A; Lu Z; Baumann E; Vobornik D; Taylor R; Stanimirovic D; and Johnston L J. Nanoscale Imaging of Epidermal Growth Factor Receptor Clustering. *Journal of Biological Chemistry*, **2009**, 285(5), 3145–3156.
- [34] Ichinose J; Murata M; Yanagida T; and Sako Y. EGF signalling amplification induced by dynamic clustering of EGFR. *Biochemical and Biophysical Research Communications*, **2004**, 324(3), 1143–1149.
- [35] Bray D; Levin M D; and Morton Firth C J. Receptor clustering as a cellular mechanism to control sensitivity. *Nature*, **1998**, 393(6680), 85–88.
- [36] Bethani I; Skånland S S; Dikic I; and Acker Palmer A. Spatial organization of transmembrane receptor signalling, **2010**. ISSN 14602075.
- [37] Caré B R and Soula H A. Impact of receptor clustering on ligand binding. *BMC Systems Biology*, **2011**, 5.
- [38] Caré B R and Soula H A. Receptor clustering affects signal transduction at the membrane level in the reaction-limited regime. *Physical Review E - Statistical, Nonlinear, and Soft Matter Physics*, **2013**, 87(1).
- [39] Stabley D; Retterer S; Marshall S; and Salaita K. Manipulating the lateral diffusion of surface-anchored EGF demonstrates that receptor clustering modulates phosphorylation levels. *Integrative Biology (United Kingdom)*, **2013**, 5(4), 659–668.
- [40] Yarden Y and Schlessinger J. Epidermal Growth Factor Induces Rapid, Reversible Aggregation of the Purified Epidermal Growth Factor Receptor. *Biochemistry*, **1987**, 26(5), 1443–1451.
- [41] Clayton A H; Orchard S G; Nice E C; Posner R G; and Burgess A W. Predominance of activated EGFR higher-order oligomers on the cell surface. *Growth Factors*, **2008**, 26(6), 316–324.
- [42] Verveer P J; Wouters F S; Reynolds A R; and Bastiaens P I. Quantitative imaging of lateral ErbB1 receptor signal propagation in the plasma membrane. *Science*, **2000**, 290(5496), 1567–1570.
- [43] Ariotti N; Liang H; Xu Y; Zhang Y; Yonekubo Y; Inder K; Du G; Parton R G; Hancock J F; and Plowman S J. Epidermal Growth Factor Receptor Activation Remodels the Plasma Membrane Lipid Environment To Induce Nanocluster Formation. *Molecular and Cellular Biology*, **2010**, 30(15), 3795–3804.
- [44] Nagy P; Claus J; Jovin T M; and Arndt Jovin D J. Distribution of resting and ligand-bound ErbB1 and ErbB2 receptor tyrosine kinases in living cells using number and brightness analysis. *Proceedings of the National Academy of Sciences*, **2010**, 107(38), 16524–16529.

- [45] Szabó Á; Szöllosl J; and Nagy P. Cocustering of ErbB1 and ErbB2 revealed by FRET-sensitized acceptor bleaching. *Biophysical Journal*, **2010**, 99(1), 105–114.
- [46] Zhang S and Reinhard B M. Characterizing Large-Scale Receptor Clustering on the Single Cell Level: A Comparative Plasmon Coupling and Fluorescence Superresolution Microscopy Study. *Journal of Physical Chemistry B*, **2019**, 123(26), 5494–5505.
- [47] Abulrob A; Lu Z; Baumann E; Vobornik D; Taylor R; Stanimirovic D; and Johnston L J. Nanoscale imaging of epidermal growth factor receptor clustering: Effects of inhibitors. *Journal of Biological Chemistry*, **2010**, 285(5), 3145–3156.
- [48] Wang Y; Gao J; Guo X; Tong T; Shi X; Li L; Qi M; Wang Y; Cai M; Jiang J; Xu C; Ji H; and Wang H. Regulation of EGFR nanocluster formation by ionic protein-lipid interaction. *Cell Research*, **2014**, 24(8), 959–976.
- [49] Saffarian S; Li Y; Elson E L; and Pikey L J. Oligomerization of the EGF receptor investigated by live cell fluorescence intensity distribution analysis. *Biophysical Journal*, **2007**, 93(3), 1021–1031.
- [50] Bag N; Huang S; and Wohland T. Plasma Membrane Organization of Epidermal Growth Factor Receptor in Resting and Ligand-Bound States. *Biophysical Journal*, **2015**, 109(9), 1925–1936.
- [51] Orr G; Hu D; Özçelik S; Opresko L K; Wiley H S; and Colson S D. Cholesterol dictates the freedom of EGF receptors and HER2 in the plane of the membrane. *Biophysical Journal*, **2005**, 89(2), 1362–1373.
- [52] Gao J; Wang Y; Cai M; Pan Y; Xu H; Jiang J; Ji H; and Wang H. Mechanistic insights into EGFR membrane clustering revealed by super-resolution imaging. *Nanoscale*, **2015**, 7(6), 2511–2519.
- [53] Singhai A; Wakefield D L; Bryant K L; Hammes S R; Holowka D; and Baird B. Spatially defined EGF receptor activation reveals an F-actin-dependent phospho-erk signaling complex. *Biophysical Journal*, **2014**, 107(11), 2639–2651.
- [54] Boggara M; Athmakuri K; Srivastava S; Cole R; and Kane R S. Characterization of the diffusion of epidermal growth factor receptor clusters by single particle tracking. *Biochimica et Biophysica Acta - Biomembranes*, **2013**, 1828(2), 419–426.
- [55] Pike L J and Casey L. Cholesterol levels modulate EGF receptor-mediated signaling by altering receptor function and trafficking. *Biochemistry*, **2002**, 41(32), 10315–10322.

- [56] Yang S; Raymond Stintz M A; Ying W; Zhang J; Lidke D S; Steinberg S L; Williams L; Oliver J M; and Wilson B S. Mapping ErbB receptors on breast cancer cell membranes during signal transduction. *Journal of Cell Science*, **2007**, 120(16), 2763–2773.
- [57] Clayton A H; Walker F; Orchard S G; Henderson C; Fuchs D; Rothacker J; Nice E C; and Burgess A W. Ligand-induced dimer-tetramer transition during the activation of the cell surface epidermal growth factor receptor-A multidimensional microscopy analysis. *Journal of Biological Chemistry*, **2005**, 280(34), 30392–30399.
- [58] Gamou S and Shimizu N. Hydrogen peroxide preferentially enhances the tyrosine phosphorylation of epidermal growth factor receptor. *FEBS Letters*, **1995**, 357(2), 161–164.
- [59] Bae Y S; Kang S W; Seo M S; Baines I C; Tckle E; Chock P B; and Rhee S G. Epidermal growth factor (EGF)-induced generation of hydrogen peroxide. Role in EGF receptor-mediated tyrosine phosphorylation. *Journal of Biological Chemistry*, **1997**, 272(1), 217–221.
- [60] Rhee S G B Y S K S W S M S B I C T E C P B. Epidermal growth factor (EGF)-induced generation of hydrogen peroxide. Role in EGF receptor-mediated tyrosine phosphorylation. *Journal of Biological Chemistry*, **1997**, 272(1), 217–221.
- [61] Miller E W; Tulyanthan O; Isacoff E Y; and Chang C J. Molecular imaging of hydrogen peroxide produced for cell signaling. *Nature Chemical Biology*, **2007**, 3(5), 263–267.
- [62] DeYulia G J; Cárcamo J M; Bórquez Ojeda O; Shelton C C; and Golde D W. Hydrogen peroxide generated extracellularly by receptor-ligand interaction facilitates cell signaling. *Proceedings of the National Academy of Sciences of the United States of America*, **2005**, 102(14), 5044–5049.
- [63] Fischer O M; Giordano S; Comoglio P M; and Ullrich A. Reactive oxygen species mediate met receptor transactivation by G protein-coupled receptors and the epidermal growth factor receptor in human carcinoma cells. *Journal of Biological Chemistry*, **2004**, 279(28), 28970–28978.
- [64] Park H S; Lee S H; Park D; Lee J S; Ryu S H; Lee W J; Rhee S G; and Bae Y S. Sequential Activation of Phosphatidylinositol 3-Kinase, Pix, Rac1, and Nox1 in Growth Factor-Induced Production of H₂O₂. *Molecular and Cellular Biology*, **2004**, 24(10), 4384–4394.
- [65] Paulsen C E; Truong T H; Garcia F J; Homann A; Gupta V; Leonard S E; and Carroll K S. Peroxide-dependent sulfenylation of the EGFR catalytic site enhances kinase activity. *Nature Chemical Biology*, **2012**, 8(1), 57–64.

- [66] Liou G Y and Storz P. Reactive oxygen species in cancer, **2010**. ISSN 10715762.
- [67] Schieber M and Chandel N S. ROS function in redox signaling and oxidative stress, **2014**. ISSN 09609822.
- [68] Kim J; Kim J; and Bae J S. ROS homeostasis and metabolism: A critical liaison for cancer therapy. *Experimental and Molecular Medicine*, **2016**, 48(11).
- [69] Dickinson B C and Chang C J. Chemistry and biology of reactive oxygen species in signaling or stress responses, **2011**. ISSN 15524469.
- [70] Finkel T. Signal transduction by reactive oxygen species, **2011**. ISSN 00219525.
- [71] D'Autréaux B and Toledano M B. ROS as signalling molecules: Mechanisms that generate specificity in ROS homeostasis, **2007**. ISSN 14710072.
- [72] Lambeth J D. NOX enzymes and the biology of reactive oxygen, **2004**. ISSN 14741733.
- [73] Forman H J; Fukuto J M; and Torres M. Redox signaling: Thiol chemistry defines which reactive oxygen and nitrogen species can act as second messengers, **2004**. ISSN 03636143.
- [74] Winterbourn C C. Reconciling the chemistry and biology of reactive oxygen species, **2008**. ISSN 15524469.
- [75] Dröge W. Free radicals in the physiological control of cell function, **2002**. ISSN 00319333.
- [76] Truong T H; Ung P M U; Palde P B; Paulsen C E; Schlessinger A; and Carroll K S. Molecular Basis for Redox Activation of Epidermal Growth Factor Receptor Kinase. *Cell Chemical Biology*, **2016**, 23(7), 837–848.
- [77] Meng T C; Fukada T; and Tonks N K. Reversible oxidation and inactivation of protein tyrosine phosphatases in vivo. *Molecular Cell*, **2002**, 9(2), 387–399.
- [78] Lee S R; Kwont K S; Kim S R; and Rhee S G. Reversible inactivation of protein-tyrosine phosphatase 1B in A431 cells stimulated with epidermal growth factor. *Journal of Biological Chemistry*, **1998**, 273(25), 15366–15372.
- [79] Goldkorn T; Balaban N; Matsukuma K; Chea V; Gould R; Last J; Chan C; and Chavez C. EGF-receptor phosphorylation and signaling are targeted by H₂O₂ redox stress. *American Journal of Respiratory Cell and Molecular Biology*, **1998**, 19(5), 786–798.
- [80] Chen K; Kirber M T; Xiao H; Yang Y; and Keaney J F. Regulation of ROS signal transduction by NADPH oxidase 4 localization. *Journal of Cell Biology*, **2008**, 181(7), 1129–1139.

- [81] Boyd P S; Struve N; Bach M; Eberle J P; Gote M; Schock F; Cremer C; Kriegs M; and Hausmann M. Clustered localization of EGFRvIII in glioblastoma cells as detected by high precision localization microscopy. *Nanoscale*, **2016**, 8(48), 20037–20047.
- [82] Truong T H and Carroll K S. Redox regulation of epidermal growth factor receptor signaling through cysteine oxidation. *Biochemistry*, **2012**, 51(50), 9954–9965.
- [83] Lim J B; Huang B K; Deen W M; and Sikes H D. Analysis of the lifetime and spatial localization of hydrogen peroxide generated in the cytosol using a reduced kinetic model. *Free Radical Biology and Medicine*, **2015**, 89, 47–53.
- [84] Zhang Q and Reinhard B M. Ligand Density and Nanoparticle Clustering Cooperate in the Multivalent Amplification of Epidermal Growth Factor Receptor Activation, **2018**. ISSN 1936086X.
- [85] Reynolds A R; Tischer C; Verveer P J; Rocks O; and Bastiaens P I. EGFR activation coupled to inhibition of tyrosine phosphatases causes lateral signal propagation. *Nature Cell Biology*, **2003**, 5(5), 447–453.
- [86] Wu L; Yu X; Feizpour A; and Reinhard B M. Nanoconjugation: A materials approach to enhance epidermal growth factor induced apoptosis. *Biomaterials Science*, **2014**, 2(2), 156–166.
- [87] Khanehzar A; Fraire J C; Xi M; Feizpour A; Xu F; Wu L; Coronado E A; and Reinhard B M. Nanoparticle-cell interactions induced apoptosis: A case study with nanoconjugated epidermal growth factor. *Nanoscale*, **2018**, 10(14), 6712–6723.
- [88] Huang B; Bates M; and Zhuang X. Super-Resolution Fluorescence Microscopy. *Annual Review of Biochemistry*, **2009**, 78(1), 993–1016.
- [89] Valley C C; Lidke K A; and Lidke D S. The spatiotemporal organization of ErbB receptors: Insights from microscopy. *Cold Spring Harbor Perspectives in Biology*, **2014**, 6(2).
- [90] Carpenter G; Stoscheck C M; and Soderquist A M. Epidermal Growth Factor. *Annals of the New York Academy of Sciences*, **1982**, 397(1), 11–17.
- [91] Digman M A; Wiseman P W; Choi C; Horwitz A R; and Gratton E. Stoichiometry of molecular complexes at adhesions in living cells. *Proceedings of the National Academy of Sciences of the United States of America*, **2009**, 106(7), 2170–2175.
- [92] Ibach J; Radon Y; Gelléri M; Sonntag M H; Brunsveld L; Bastiaens P I; and Verveer P J. Single particle tracking reveals that EGFR signaling activity is amplified in clathrin-coated pits. *PLoS ONE*, **2015**, 10(11).

- [93] Sergé A; Bertaux N; Rigneault H; and Marguet D. Dynamic multiple-target tracing to probe spatiotemporal cartography of cell membranes. *Nature Methods*, **2008**, 5(8), 687–694.
- [94] Lidke D S; Nagy P; Heintzmann R; Arndt Jovin D J; Post J N; Grecco H E; Jares Erijman E A; and Jovin T M. Quantum dot ligands provide new insights into erbB/HER receptor-mediated signal transduction. *Nature Biotechnology*, **2004**, 22(2), 198–203.
- [95] Zhang R; Fruhwirth G O; Coban O; Barrett J E; Burgoyne T; Lee S H; Simonson P D; Baday M; Kholodenko B N; Futter C E; Ng T; and Selvin P R. Probing the Heterogeneity of Protein Kinase Activation in Cells by Super-resolution Microscopy. *ACS Nano*, **2017**, 11(1), 249–257.
- [96] Betzig E; Patterson G H; Sougrat R; Lindwasser O W; Olenych S; Bonifacino J S; Davidson M W; Lippincott Schwartz J; and Hess H F. Imaging intracellular fluorescent proteins at nanometer resolution. *Science*, **2006**, 313(5793), 1642–1645.
- [97] Mason M D; Hess S T; and Girirajan T P K. Ultra-High Resolution Imaging by Fluorescence Photoactivation Localization Microscopy. *Biophysical Journal*, **2006**, 91(11), 4258–4272.
- [98] Rust M J; Bates M; and Zhuang X. Sub-diffraction-limit imaging by stochastic optical reconstruction microscopy (STORM). *Nature Methods*, **2006**, 3(10), 793–795.
- [99] Heilemann M; Van De Linde S; Schüttelpelz M; Kasper R; Seefeldt B; Mukherjee A; Tinnefeld P; and Sauer M. Subdiffraction-resolution fluorescence imaging with conventional fluorescent probes. *Angewandte Chemie - International Edition*, **2008**, 47(33), 6172–6176.
- [100] Turkowyd B; Virant D; and Endesfelder U. From single molecules to life: microscopy at the nanoscale. *Analytical and Bioanalytical Chemistry*, **2016**, 408(25), 6885–6911.
- [101] Khater I M; Nabi I R; and Hamarneh G. A Review of Super-Resolution Single-Molecule Localization Microscopy Cluster Analysis and Quantification Methods. *Patterns*, **2020**, 1(3).
- [102] van Lengerich B; C A; EM P; B H; and N J. EGF and NRG induce phosphorylation of HER3/ERBB3 by EGFR using distinct oligomeric mechanisms. *Proceedings of the National Academy of Sciences*, **2017**, 114(14), E2836–E2845.
- [103] Needham S R; Hirsch M; Rolfe D J; Clarke D T; Zanetti Domingues L C; Wareham R; and Martin Fernandez M L. Measuring EGFR Separations on Cells

- with 10 nm Resolution via Fluorophore Localization Imaging with Photo-bleaching. *PLoS ONE*, **2013**, 8(5).
- [104] Sezgin E. Super-resolution optical microscopy for studying membrane structure and dynamics. *Journal of Physics Condensed Matter*, **2017**, 29(27).
- [105] Soeller C and Jayasinghe I D. Quantitative Super-Resolution Microscopy of Cardiomyocytes. *Microscopy of the Heart*, **2018**, pages 37–73.
- [106] Godin A G; Lounis B; and Cognet L. Super-resolution microscopy approaches for live cell imaging, **2014**. ISSN 15420086.
- [107] Nahidiazar L; Agronskaia A V; Broertjes J; Van Broek B D; and Jalink K. Optimizing imaging conditions for demanding multi-color super resolution localization microscopy. *PLoS ONE*, **2016**.
- [108] Glushonkov O; Réal E; Boutant E; Mély Y; and Didier P. Optimized protocol for combined PALM-dSTORM imaging. *Scientific Reports*, **2018**, 8(1).
- [109] Sengupta P; van Engelenburg S B; and Lippincott Schwartz J. Superresolution Imaging of Biological Systems Using Photoactivated Localization Microscopy. *Chemical Reviews*, **2014**, 114(6), 3189–3202.
- [110] Crow M J; Seekell K; Ostrander J H; and Wax A. Monitoring of receptor dimerization using plasmonic coupling of gold nanoparticles. *ACS Nano*, **2011**, 5(11), 8532–8540.
- [111] Rong G; Wang H; Skewis L R; and Reinhard B M. Resolving Sub-Diffraction limit encounters in nanoparticle tracking using live cell plasmon coupling microscopy. *Nano Letters*, **2008**, 8(10), 3386–3393.
- [112] Wang H; Wu L; and Reinhard B M. Scavenger receptor mediated endocytosis of silver nanoparticles into J774A.1 macrophages is heterogeneous. *ACS Nano*, **2012**, 6(8), 7122–7132.
- [113] Wang H; Rong G; Yan B; Yang L; and Reinhard B M. Optical sizing of immunolabel clusters through multispectral plasmon coupling microscopy. *Nano Letters*, **2011**, 11(2), 498–504.
- [114] Yu X; Wang J; Feizpour A; and Reinhard B M. Illuminating the lateral organization of cell-surface CD24 and CD44 through plasmon coupling between Au nanoparticle immunolabels. *Analytical Chemistry*, **2013**, 85(3), 1290–1294.
- [115] Messersmith R E; Nusz G J; and Reed S M. Using the localized surface plasmon resonance of gold nanoparticles to monitor lipid membrane assembly and protein binding. *Journal of Physical Chemistry C*, **2013**, 117(50), 26725–26733.
- [116] Hamilton D J; Coffman M D; Knight J D; and Reed S M. Lipid-Coated Gold Nanoparticles and FRET Allow Sensitive Monitoring of Liposome Clustering

Mediated by the Synaptotagmin-7 C2A Domain. *Langmuir*, **2017**, 33(36), 9222–9230.

- [117] Kumar S; Diwan A; Singh P; Gulati S; Choudhary D; Mongia A; Shukla S; and Gupta A. Functionalized gold nanostructures: Promising gene delivery vehicles in cancer treatment. *RSC Advances*, **2019**, 9(41), 23894–23907.
- [118] Yu X; Xu F; Ramirez N G P; Kijewski S D; Akiyama H; Gummuluru S; and Reinhard B M. Dressing up nanoparticles: A membrane wrap to induce formation of the virological synapse. *ACS Nano*, **2015**, 9(4), 4182–4192.
- [119] Sepúlveda B; Angelomé P C; Lechuga L M; and Liz Marzán L M. LSPR-based nanobiosensors, **2009**. ISSN 17480132.
- [120] Jain P K; Lee K S; El Sayed I H; and El Sayed M A. Calculated absorption and scattering properties of gold nanoparticles of different size, shape, and composition: Applications in biological imaging and biomedicine. *Journal of Physical Chemistry B*, **2006**, 110(14), 7238–7248.
- [121] Reinhard B M; Siu M; Agarwal H; Alivisatos A P; and Liphardt J. Calibration of dynamic molecular rulers based on plasmon coupling between gold nanoparticles. *Nano Letters*, **2005**, 5(11), 2246–2252.
- [122] Maier S A; Brongersma M L; Kik P G; and Atwater H A. Observation of near-field coupling in metal nanoparticle chains using far-field polarization spectroscopy. *Physical Review B - Condensed Matter and Materials Physics*, **2002**, 65(19), 1–4.
- [123] Jain P K and El Sayed M A. Universal scaling of plasmon coupling in metal nanostructures: Extension from particle pairs to nanoshells. *Nano Letters*, **2007**, 7(9), 2854–2858.
- [124] Jain P K; Huang W; and El Sayed M A. On the universal scaling behavior of the distance decay of plasmon coupling in metal nanoparticle pairs: A plasmon ruler equation. *Nano Letters*, **2007**, 7(7), 2080–2088.
- [125] Lerch S and Reinhard B M. Spectral signatures of charge transfer in assemblies of molecularly-linked plasmonic nanoparticles. *International Journal of Modern Physics B*, **2017**, 31(24).
- [126] Wang J; Boriskina S V; Wang H; and Reinhard B M. Illuminating epidermal growth factor receptor densities on filopodia through plasmon coupling. *ACS Nano*, **2011**, 5(8), 6619–6628.
- [127] Hu Q; Tay L L; Noestheden M; and Pezacki J P. Mammalian cell surface imaging with nitrile-functionalized nanoprobe: Biophysical characterization of aggregation and polarization anisotropy in SERS imaging. *Journal of the American Chemical Society*, **2007**, 129(1), 14–15.

- [128] Kennedy D C; Tay L L; Lyn R K; Rouleau Y; Hulse J; and Pezacki J P. Nanoscale aggregation of cellular β 2-adrenergic receptors measured by plasmonic interactions of functionalized nanoparticles. *ACS Nano*, **2009**, 3(8), 2329–2339.
- [129] Chung T; Koker T; and Pinaud F. Split-GFP: SERS Enhancers in Plasmonic Nanocluster Probes. *Small*, **2016**, 12(42), 5891–5901.
- [130] Wu L and Reinhard B M. Probing subdiffraction limit separations with plasmon coupling microscopy: Concepts and applications, **2014**. ISSN 14604744.
- [131] Crow M J; Grant G; Provenzale J M; and Wax A. Molecular imaging and quantitative measurement of epidermal growth factor receptor expression in live cancer cells using immunolabeled gold nanoparticles. *American Journal of Roentgenology*, **2009**, 192(4), 1021–1028.
- [132] Aaron J; Nitin N; Travis K; Kumar S; Collier T; Park S Y; José Yacamán M; Coghlan L; Follen M; Richards Kortum R; and Sokolov K. Plasmon resonance coupling of metal nanoparticles for molecular imaging of carcinogenesis in vivo. *Journal of Biomedical Optics*, **2007**, 12(3), 034007.
- [133] Wang J; Yu X; Boriskina S V; and Reinhard B M. Quantification of differential ErbB1 and ErbB2 cell surface expression and spatial nanoclustering through plasmon coupling. *Nano Letters*, **2012**, 12(6), 3231–3237.
- [134] Goodman C M; McCusker C D; Yilmaz T; and Rotello V M. Toxicity of gold nanoparticles functionalized with cationic and anionic side chains. *Bioconjugate Chemistry*, **2004**, 15(4), 897–900.
- [135] Pan Y; Leifert A; Ruau D; Neuss S; Bornemann J; Schmid G; Brandau W; Simon U; and Jahnen Dechent W. Gold nanoparticles of diameter 1.4 nm trigger necrosis by oxidative stress and mitochondrial damage. *Small*, **2009**, 5(18), 2067–2076.
- [136] Suk J S; Xu Q; Kim N; Hanes J; and Ensign L M. PEGylation as a strategy for improving nanoparticle-based drug and gene delivery. *Advanced Drug Delivery Reviews*, **2016**, 99, 28–51.
- [137] Colombo M; Fiandra L; Alessio G; Mazzucchelli S; Nebuloni M; De Palma C; Kantner K; Pelaz B; Rotem R; Corsi F; Parak W J; and Prospero D. Tumour homing and therapeutic effect of colloidal nanoparticles depend on the number of attached antibodies. *Nature Communications*, **2016**, 7.
- [138] Nakase I; Ueno N; Katayama M; Noguchi K; Takatani Nakase T; Kobayashi N B; Yoshida T; Fujii I; and Futaki S. Receptor clustering and activation by multivalent interaction through recognition peptides presented on exosomes. *Chemical Communications*, **2017**, 53(2), 317–320.

- [139] Hong S; Leroueil P R; Majoros I J; Orr B G; Baker J R; and Banaszak Holl M M. The Binding Avidity of a Nanoparticle-Based Multivalent Targeted Drug Delivery Platform. *Chemistry and Biology*, **2007**, 14(1), 107–115.
- [140] Wang X; Ramström O; and Yan M. Quantitative analysis of multivalent ligand presentation on gold glyconanoparticles and the impact on lectin binding. *Analytical Chemistry*, **2010**, 82(21), 9082–9089.
- [141] Wang X; Matei E; Deng L; Ramström O; Gronenborn A M; and Yan M. Multivalent glyconanoparticles with enhanced affinity to the anti-viral lectin Cyanovirin-N. *Chemical Communications*, **2011**, 47(30), 8620–8622.
- [142] Mammen M; Choi S K; and Whitesides G M. Polyvalent interactions in biological systems: Implications for design and use of multivalent ligands and inhibitors. *Angewandte Chemie - International Edition*, **1998**, 37(20), 2754–2794.
- [143] Kane R S. Thermodynamics of multivalent interactions: Influence of the linker. *Langmuir*, **2010**, 26(11), 8636–8640.
- [144] Conway A; Vazin T; Spelke D P; Rode N A; Healy K E; Kane R S; and Schaffer D V. Multivalent ligands control stem cell behaviour in vitro and in vivo. *Nature Nanotechnology*, **2013**, 8(11), 831–838.
- [145] Silpe J E; Sumit M; Thomas T P; Huang B; Kotlyar A; Van Dongen M A; Banaszak Holl M M; Orr B G; and Choi S K. Avidity modulation of folate-targeted multivalent dendrimers for evaluating biophysical models of cancer targeting nanoparticles. *ACS Chemical Biology*, **2013**, 8(9), 2063–2071.
- [146] Wang J; Min J; Eghtesadi S A; Kane R S; and Chilkoti A. Quantitative Study of the Interaction of Multivalent Ligand-Modified Nanoparticles with Breast Cancer Cells with Tunable Receptor Density. *ACS Nano*, **2020**, 14(1), 372–383.
- [147] Gestwicki J E; Cairo C W; Strong L E; Oetjen K A; and Kiessling L L. Influencing receptor-ligand binding mechanisms with multivalent ligand architecture. *Journal of the American Chemical Society*, **2002**, 124(50), 14922–14933.
- [148] Zhang Y; Cheng M; Cao J; Zhang Y; Yuan Z; Wu Q; and Wang W. Multivalent nanoparticles for personalized theranostics based on tumor receptor distribution behavior. *Nanoscale*, **2019**, 11(11), 5005–5013.
- [149] Berkers J A M; Van Bergen En Henegouwen P M P; and Boonstra J. Three Classes of Epidermal Growth Factor Receptors on HeLa Cells*. *Journal of Biological Chemistry*, **1991**, 266(2), 922–927. URL <http://www.jbc.org/content/266/2/922.full.pdf>.

- [150] Filmus J; Pollak M N; Cailleau R; and Buick R N. MDA-468, a human breast cancer cell line with a high number of epidermal growth factor (EGF) receptors, has an amplified EGF receptor gene and is growth inhibited by EGF. *Biochemical and Biophysical Research Communications*, **1985**, 128(2), 898–905.
- [151] Su K H; Wei Q H; Zhang X; Mock J J; Smith D R; and Schultz S. Interparticle coupling effects on plasmon resonances of nanogold particles. *Nano Letters*, **2003**, 3(8), 1087–1090.
- [152] Rechberger W; Hohenau A; Leitner A; Krenn J R; Lamprecht B; and Aussenegg F R. Optical properties of two interacting gold nanoparticles. *Optics Communications*, **2003**, 220(1-3), 137–141.
- [153] Reinhard B M; Siu M; Agarwal H; Alivisatos A P; and Liphardt J. Calibration of dynamic molecular rulers based on plasmon coupling between gold nanoparticles. *Nano Letters*, **2005**, 5(11), 2246–2252.
- [154] Yang L; Wang H; Yan B; and Reinhard B M. Calibration of silver plasmon rulers in the 1-25 nm separation range: Experimental indications of distinct plasmon coupling regimes. *Journal of Physical Chemistry C*, **2010**, 114(11), 4901–4908.
- [155] Prodan E; Radloff C; Halas N J; and Nordlander P. A Hybridization Model for the Plasmon Response of Complex Nanostructures. *Science*, **2003**, 302 (5644), 419–422.
- [156] Nordlander P; Oubre C; Prodan E; Li K; and Stockman M I. Plasmon hybridization in nanoparticle dimers. *Nano Letters*, **2004**, 4(5), 899–903.
- [157] Yguerabide J and Yguerabide E E. Light-scattering submicroscopic particles as highly fluorescent analogs and their use as tracer labels in clinical and biological applications II. Experimental characterization. *Analytical Biochemistry*, **1998**, 262(2), 157–176.
- [158] Yu X; Feizpour A; Ramirez N G P; Wu L; Akiyama H; Xu F; Gummuluru S; and Reinhard B M. Glycosphingolipid-functionalized nanoparticles recapitulate CD169-dependent HIV-1 uptake and trafficking in dendritic cells. *Nature Communications*, **2014**, 5.
- [159] Yang J A and Murphy C J. Evidence for patchy lipid layers on gold nanoparticle surfaces. *Langmuir*, **2012**, 28(12), 5404–5416.
- [160] Uyemura T; Takagi H; Yanagida T; and Sako Y. Single-molecule analysis of epidermal growth factor signaling that leads to ultrasensitive calcium response. *Biophysical Journal*, **2005**, 88(5), 3720–3730.

- [161] Banerjee R N, A. & Dave. Validating clusters using the Hopkins statistic. In *IEEE International Conference on Fuzzy Systems*, Budapest, Hungary, **2004**. IEEE.
- [162] Moh K J; Yuan X C; Bu J; Zhu S W; and Gao B Z. Surface plasmon resonance imaging of cell-substrate contacts with radially polarized beams. *Optics Express*, **2008**, 16(25), 20734.
- [163] Beuthan J; Minet O; Helfmann J; Herrig M; and Müller G. The spatial variation of the refractive index in biological cells. *Physics in Medicine and Biology*, **1996**, 41(3), 369–382.
- [164] Johnsen S and Widder E A. The physical basis of transparency in biological tissue: Ultrastructure and the minimization of light scattering. *Journal of Theoretical Biology*, **1999**, 199(2), 181–198.
- [165] Den Hartigh J C; Van Bergen En Henegouwen P M; Verkleij A J; and Boonstra J. The EGF receptor is an actin-binding protein. *Journal of Cell Biology*, **1992**, 119(2), 349–355.
- [166] Coué M; Brenner S L; Spector I; and Korn E D. Inhibition of actin polymerization by latrunculin A. *FEBS Letters*, **1987**, 213(2), 316–318.
- [167] Chung I; Akita R; Vandlen R; Toomre D; Schlessinger J; and Mellman I. Spatial control of EGF receptor activation by reversible dimerization on living cells. *Nature*, **2010**, 464(7289), 783–7. URL <http://www.ncbi.nlm.nih.gov/pubmed/20208517>.
- [168] Clayton A H; Tavarnesi M L; and Johns T G. Unligated epidermal growth factor receptor forms higher order oligomers within microclusters on A431 cells that are sensitive to tyrosine kinase inhibitor binding. *Biochemistry*, **2007**, 46(15), 4589–4597.
- [169] Teramura Y; Ichinose J; Takagi H; Nishida K; Yanagida T; and Sako Y. Single-molecule analysis of epidermal growth factor binding on the surface of living cells. *EMBO Journal*, **2006**, 25(18), 4215–4222.
- [170] Nieuwenhuizen R P; Lidke K A; Bates M; Puig D L; Grünwald D; Stallinga S; and Rieger B. Measuring image resolution in optical nanoscopy. *Nature Methods*, **2013**.
- [171] Andronov L; Orlov I; Lutz Y; Vonesch J L; and Klaholz B P. ClusterViSu, a method for clustering of protein complexes by Voronoi tessellation in super-resolution microscopy. *Scientific Reports*, **2016**, 6.
- [172] Henriques R; Lelek M; Fornasiero E F; Valtorta F; Zimmer C; and Mhlanga M M. QuickPALM: 3D real-time photoactivation nanoscopy image processing in ImageJ. *Nature Methods*, **2010**, 7(5), 339–340.

- [173] Owen D M; Rentero C; Rossy J; Magenau A; Williamson D; Rodriguez M; and Gaus K. PALM imaging and cluster analysis of protein heterogeneity at the cell surface. *Journal of Biophotonics*, **2010**, 3(7), 446–454.
- [174] Owen D M; Williamson D; Magenau A; and Gaus K. Optical techniques for imaging membrane domains in live cells (live-cell palm of protein clustering). *Methods in Enzymology*, **2012**, 504, 221–235.
- [175] Ober R J; Ram S; and Ward E S. Localization Accuracy in Single-Molecule Microscopy. *Biophysical Journal*, **2004**, 86(2), 1185–1200.
- [176] Kolb H C; Finn M G; and Sharpless K B. Click Chemistry: Diverse Chemical Function from a Few Good Reactions. *Angewandte Chemie - International Edition*, **2001**, 40(11), 2004–2021.
- [177] Santra M; Reed C C; and Iozzo R V. Decorin binds to a narrow region of the epidermal growth factor (EGF) receptor, partially overlapping but distinct from the EGF-binding epitope. *Journal of Biological Chemistry*, **2002**, 277(38), 35671–35681.
- [178] Young H S and Carroll K S. Profiling protein thiol oxidation in tumor cells using sulfenic acid-specific antibodies. *Proceedings of the National Academy of Sciences of the United States of America*, **2009**, 106(38), 16163–16168.
- [179] Nemoto S; Takeda K; Yu Z X; Ferrans V J; and Finkel T. Role for Mitochondrial Oxidants as Regulators of Cellular Metabolism. *Molecular and Cellular Biology*, **2000**, 20(19), 7311–7318.
- [180] Murphy M P. How mitochondria produce reactive oxygen species. *Biochemical Journal*, **2009**, 417(1), 1–13.
- [181] Turkevich J; Stevenson P C; and Hillier J. A study of the nucleation and growth processes in the synthesis of colloidal gold. *Discussions of the Faraday Society*, **1951**, 11, 55–75.
- [182] Bilan D S; Pase L; Joosen L; Gorokhovatsky A Y; Ermakova Y G; Gadella T W; Grabher C; Schultz C; Lukyanov S; and Belousov V V. HyPer-3: A genetically encoded H₂O₂ probe with improved performance for ratiometric and fluorescence lifetime imaging. *ACS Chemical Biology*, **2013**, 8(3), 535–542.
- [183] Pak V V; Ezeriņa D; Lyublinskaya O G; Pedre B; Tyurin Kuzmin P A; Mishina N M; Thauvin M; Young D; Wahni K; Martínez Gache S A; Demidovich A D; Ermakova Y G; Maslova Y D; Shokhina A G; Eroglu E; Bilan D S; Bogeski I; Michel T; Vriz S; Messens J; and Belousov V V. Ultrasensitive Genetically Encoded Indicator for Hydrogen Peroxide Identifies Roles for the Oxidant in

Cell Migration and Mitochondrial Function. *Cell Metabolism*, **2020**, 31(3), 642–653.

